Applications for CMOS pixel sensors in ion-beam therapy

Claire-Anne Reidel

▶ **To cite this version:**

Claire-Anne Reidel. Applications for CMOS pixel sensors in ion-beam therapy. Physics [physics]. Université de Strasbourg, 2020. English. NNT : 2020STRAE040 . tel-03177291

HAL Id: tel-03177291
https://theses.hal.science/tel-03177291

Submitted on 23 Mar 2021

HAL is a multi-disciplinary open access archive for the deposit and dissemination of scientific research documents, whether they are published or not. The documents may come from teaching and research institutions in France or abroad, or from public or private research centers.

L'archive ouverte pluridisciplinaire **HAL**, est destinée au dépôt et à la diffusion de documents scientifiques de niveau recherche, publiés ou non, émanant des établissements d'enseignement et de recherche français ou étrangers, des laboratoires publics ou privés.

UNIVERSITÉ DE STRASBOURG

École Doctorale de Physique et Chimie-Physique

Laboratoire : Institut Pluridisciplinaire Hubert Curien

Thèse présentée par :

Claire-Anne REIDEL

pour obtenir le grade de : Docteur de l'université de Strasbourg

Discipline/ Spécialité : Physique

Applications for CMOS pixel sensors in ion-beam therapy

THÈSE dirigée par :

Finck Christian	Docteur, Université de Strasbourg

RAPPORTEURS :

Patera Vincenzo	Professor, University of Rome
Jäkel Oliver	Professor Doctor, German Cancer Research Center

AUTRES MEMBRES DU JURY :

Weber Ulrich	Docteur, GSI Helmholtzzentrum für Schwerionenforschung
Baudot Jérôme	Professeur, Université de Strasbourg
Husson Daniel	Docteur, Université de Strasbourg
Vanstalle Marie	Docteur, Université de Strasbourg
Durante Marco	Professeur, GSI Helmholtzzentrum für Schwerionenforschung

Dream big, work hard...

To all of those who believed in me.

Acknowledgments

It has been a long and incredible journey that started more than three years ago, after exchanging some e-mails with Dr. Uli Weber. I explained to him my wish to do a Ph.D. in physics within his group at GSI. The probability of getting such a position was very low because of my engineering career, but my motivation for this work overcomes the lack of experience. After several months, Dr. Uli Weber offered to me the possibility to integrate his group as a fellow, which I accepted without hesitation. I thus started to work in the Space Radiation Physics group of the Biophysics department at GSI in September 2016, under the supervision of Uli. After six months of hard work, and countless efforts, I was granted a Ph.D. position in Physics at GSI together with the university of Strasbourg.

My first thanks goes to Dr. Uli Weber, who gave me the chance to work within his group and expand my knowledge about particle therapy. He was the first person to believe in my capabilities of making this career, and for this, I could never thank him enough. I also own him my deepest gratitude for his supervision and incredible support across these years. I will always be grateful for all the knowledge he shared, all the time we spent preparing and doing experiments, and the invaluable discussions. Thank you for helping me all the way.

I would also like to thank Dr. Christian Finck as my supervisor of the University of Strasbourg. He agreed to supervise my work and has always been involved in every step of it. He also believed in my capabilities to succeed in this thesis, helped me, and supported me during these three years.

One of my biggest thanks goes to Dr. Christoph Schuy from the Biophysics department at GSI, who also supervised this work. I will always be thankful for all the time he dedicated to me, all the hours he spent teaching me programming, and helping me with the experiments. He has always been a great support during all moments, and I could always rely on his advice. I also thank him for the time we shared climbing and discussing.

Many thanks to the Biophysics department at GSI, especially to Corinna Kausch and Marco Durante, who gave me the opportunity to work in such a nice group. I also would like to thank Thomas Friedrich for his support and involvement during the beam times at the UNILAC. I want to thank the support from Felix Horst and Daria Boscolo for all simulations they have performed for me. I am very grateful to the mechanical workshop at GSI and, in particular, Elko and Harry for their amazing contribution to this work. Thank you also to Jög Jöhnke for his valuable help with the electronics. I also would like to thank Yannick and Matthias from the Ion-beam Therapy Center in Marburg for their support.

A particular thanks goes to my colleagues from GSI, who I respect scientifically and personally. Thank you to Uli, Christoph, Felix, Francesca, Daria, Alex, Tabea, and all those who shared with me this journey. Many thanks also to Stéphanie, Frédéric, and the CBM team for the lunch and coffee times together.

ACKNOWLEDGMENTS

I would like to thank my working group at the IPHC in Strasbourg, in particular Christian, Marie Vanstalle and Alexandre Sécher. Very special ones to Marie and Christian, who always welcomed me with open arms. Thank you for every great hour we shared, the excellent restaurants, the work conversations, especially the funny ones with all the jokes. But above all this, you believed in this work, supported me, and for that, I will be forever thankful.

I want to thank the PICSEL group from IPHC in Strasbourg for their support in using Mimosa-28. In particular, I would like to acknowledge Jérôme Baudot and Mathieu Goffe for their time and their help.

Many thanks to Prof. Vincenzo Patera and Prof. Oliver Jäkel who accepted to review my manuscript and to be part of my PhD committee. I also want to thank Prof. Jérôme Baudot for accepting to be the president of my jury for the PhD defense. Many thanks to Dr. Uli Weber, Dr. Christian Finck, Dr. Daniel Husson, Dr. Marie Vanstalle and Prof. Marco Durante for being part of my PhD defense committee.

I would like to thank my family and my friends. To my parents for their invaluable support. They have taught me to never give up, and to always follow my dreams. To all my friends, especially to Manon, Franci and Osnan, who always believed in me, helped in the hard moments and shared the happy ones.

To Adrian Rodriguez Rodriguez, who shared all these years with me, believed in me and stayed by my side in all moments. Thank you for your unconditional support.

Abstract

In ion-beam therapy, high precision measurements are necessary to improve the quality of patient treatment. In this thesis, several measurement methods for clinical applications, with the use of MIMOSA-28 pixel sensors, are presented. In a first part, mechanical and software optimizations were implemented in order to reach the micrometer precision of the sensor. The experimental setup has been mechanically optimized for stability, and to provide a mobile setup to be used in different ion-beam therapy facilities. Sensor holders were designed and manufactured as precise as possible to fit the sensor board, and to be light-tight. During experiments, the sensors are placed along an optical bench, and the cables are clamped to avoid any movement. An alignment procedure, which corrects mechanical misalignment by software, was developed and implemented in the reconstruction code QAPIVI, for a tracker system placed along the beam axis. This procedure, based on a global χ^2 minimization, simultaneously optimizes the alignment parameters for all events. The performance of the procedure was evaluated against simulated and experimental data. The spatial track resolution, reached after performing the alignment procedure, was better than 10 µm. Additionally, the response of the MIMOSA-28 pixel sensor, defined as the cluster size of the fired pixels, was evaluated for different ion species and energies. The data obtained from this characterization can be used to improve the data analysis of this sensor.

In a second part, a series of experiments for ion-beam therapy applications were performed. The beam profiles were evaluated at therapeutic energies for low beam intensities, with a set of sensors placed along the beam axis. The lateral beam spread was determined using the transport code SCATTMAN, after fitting the different measurement points acquired with the sensors. Afterwards, the beam width could be extracted from the fit at any position along the beam axis. An online monitoring software was developed to obtain real time information of the beam profile during an experiment. Another beam time campaign was devoted to the measurement of fluence perturbations due to high density gradients and sharp edges, especially, for fiducial markers. The latter are nowadays commonly used for image guidance in ion-beam therapy. The markers are composed of materials dense enough to be visible on the daily X-ray image projection, but also create dose inhomogeneities during the radiotherapy treatment. In this work, the fluence perturbations of four commercial fiducial markers (made of gold and carbon-coated ZrO_2) were evaluated with a new measurement concept, using a tracker system consisting of six MIMOSA-28 sensors. With this method, 3D fluence distributions were computed from all reconstructed tracks, and the maximum cold spots created, and their position along the beam axis were quantified. In this work, the measured cold spot varied between less than 3% up to 9.2% for a specific marker and a given energy for carbon ions.

Résumé

En hadronthérapie, des mesures de haute précision sont nécessaires afin d'améliorer la qualité de traitement du patient. Durant cette thèse, plusieurs méthodes de mesures pour des applications cliniques ont été effectuées avec l'utilisation de capteurs à pixels Mimosa-28. Dans un premier temps, des améliorations au niveau mécanique ont été apportées ainsi que des optimisations du code de reconstruction dans le but de pouvoir atteindre la précision micrométrique qu'offre le capteur. Le dispositif expérimental a été mécaniquement amélioré pour une meilleure stabilité afin de pouvoir le transporter dans différents centres de thérapie. Des supports de capteurs ont été dessinés et produits aussi précis que possible, ajutés à la carte du Mimosa-28. Une procédure d'alignement a été développée et implémentée dans le code de reconstruction Qapivi, afin de corriger le désalignement mécanique, pour un système de trajectométrie placé le long du faisceau. Cette procédure est basée sur la minimisation d'un χ^2 global qui optimise les paramètres d'alignements pour tous les évènements en même temps. Après l'exécution de cette procédure, la résolution des traces reconstruites est inférieure à 10 µm. De plus, la réponse du capteur Mimosa-28, définie comme la taille du groupe de pixels touchés, a été évaluée pour différentes particules et énergies. Les données obtenues, grâce à cette caractérisation, peuvent être utilisées pour améliorer l'analyse de données de ce capteur.
Dans un second temps, une série d'expériences appliquées à la hadronthérapie ont été performées. Les profils de faisceaux ont été évalués pour des énergies thérapeutiques et à basse intensité, à l'aide de plusieurs capteurs le long du faisceau. La propagation latérale du faisceau a été déterminée avec le code de transport Scattman après avoir ajusté les différents points de mesures acquis avec les capteurs. La largeur du faisceau a été déterminée, à l'aide de la courbe d'ajustement, à quelconque position le long du faisceau. Un logiciel a été développé pour obtenir le profil du faisceau en temps réel durant une expérience. Une autre campagne de faisceau a été consacrée à la mesure des perturbations créées par des changements conséquents de densités et des bords tranchants, en particulier pour les marqueurs de repères. Ces derniers sont de nos jours utilisés pour le guidage d'image en hadrontérapie. Ces marqueurs sont composés de matériaux denses qui peuvent être visibles sur l'image journalière performée aux rayons X. Cependant, ils créent aussi des inhomogénéités sur la dose délivrée durant le traitement avec des ions. Les perturbations du flux pour quatre marqueurs commerciaux ont été évaluées en utilisant un système de trajectométrie composé de six Mimosa-28. Les distributions 3D de flux ont été calculées à partir de toutes les traces reconstruites et les sous-doses ainsi que leurs positions le long de l'axe du faisceau ont été quantifiées. Les points froids mesurés varient entre moins de 3% à 9.2% pour un marqueur et une énergie de faisceau définis.

Contents

List of Tables

List of Figures

Introduction

Cancer is one of the main causes of death in the world and is expected to further increase because of the growth and aging of the population. Based on Global Cancer Observatory estimates, 18.1 million new cancer cases and 9.6 million cancer death occurred in 2018 worldwide [1]. The risk of getting cancer before the age of 70 is about 20% and the probability to die from this disease is about 10%. Prostate cancer is the most frequent form of cancer for males while breast cancer is the most common for females. For both males and females, lung cancer is highly diagnosed and appears to be one of the cancer inducing the most mortality. Nowadays, three main treatments are used against cancer: surgery, chemotherapy and radiotherapy. Other less common treatments such as immunotherapy and targeted alpha therapy can also be employed for tumor treatment. The combination of several methods can be required for successful cancer treatments such as surgery followed by radiotherapy or typically radioimmunotherapy [2], which combines immunotherapy and radiotherapy. From all patients with a localized tumor, 50% are treated by means of radiation [3] with a dose delivered generally in several fractions over 6–7 weeks.

The aim of radiotherapy is to deliver a defined homogeneous dose inside the tumor and spare the surrounding healthy tissues. The role of this treatment method is to inactivate cancer cells by exposing them to ionizing radiation that damages the DNA of the cell and lead to its death. Conventional therapy uses high energy photons produced by linear accelerators but the use of heavy charged particles for tumor treatment is also very attractive [4]. The use of particles is more complex and more expensive compared to the use of photons but their physical and biological properties offer several advantages, especially for deep-seated or radio-resistant tumors [5].

In radiotherapy, and in particular in heavy charged particle therapy, high precision in every step of the treatment is mandatory in order to deliver a conformal dose. Uncertainties, which can lead to severe consequences, can rise on the one hand from the beam side and the treatment planning and on the other hand from patient mispositioning and organ motions. To reduce these uncertainties, high precision measurements are required to establish a reliable database for particle therapy treatment and several methods are employed to precisely position the patient and to verify the tumor movements.

This work aims to improve proton and ion-beam therapy by providing high precision measurement setups and applying them to investigate radiation physics effects that are of clinical interest. The measurements were intended to be performed with the help of a tracker system composed of high resolution CMOS pixel sensors. These detectors belong

to the MAPS generation [6] and are commonly used for tracking and vertexing in the field of high energy physics. The sensors used in this work are called MIMOSA-28 [7] and were developed by the Physics with Integrated Cmos Sensors and ELectron machines (PICSEL) group at the Institut Pluridisciplinaire Hubert Curien (IPHC) located in Strasbourg. In this work, a set of these sensors was used during different experiments in order to determine charged particle trajectories.

The MIMOSA-28 sensors have been used for different tests in the past years at GSI. However, the optimum track resolution could not be reached due to mechanical instabilities of the setup during the experiments. In this work, the experimental setup is intended to be used in different facilities for several clinical applications. In order to do this, a portable and mechanically stable setup is required. The first aim of this work is to optimize the experimental setup in order to transport and build it easily in different facilities and to improve its stability for mechanical precision and robustness. The mechanical optimization of the setup was developed to exploit the micrometer precision possible to reach with the sensors.

A tracker system composed of MIMOSA-28 delivers high resolution positions from ionizing particles that pass through the sensors. The particle trajectories can then be reconstructed with a spatial resolution better than 10 µm by means of several sensors that are precisely aligned with respect to each other. A few micrometers alignment precision can be reached after performing an alignment procedure that corrects the mechanical misalignment of the sensors by software. The originally implemented alignment algorithm in the reconstruction software QAPIVI [8] is based on an iterative procedure. The latter is time consuming and the algorithm does not always converge properly. In this work, it was intended to develop a reliable alignment procedure that corrects the mechanical misalignment of the sensors through a global χ^2 minimization. This procedure aims to be low time consuming and to converge properly for any setup configurations consisting of several pixel sensors placed along the beam axis.

The response of the MIMOSA-28 sensor to different ion species and energies, with different energy losses, has not been fully characterized yet. This sensor, based on CMOS technology, is composed of almost 1 million pixels. The number of pixels fired by a charged particle varies as a function of the particle characteristics. The response of previous pixel sensor generations (MIMOSA-18 and MIMOSA-26) was investigated by Spiriti et al. (2017) [9]. During this PhD thesis, the characterization of the MIMOSA-28 against different ion species and energies aims to extend the experimental data sets of the previous study in order to improve the understanding of the sensor response and exploit these informations for an improvement in data analysis.

During several experiments for ion-beam therapy, low particle beam intensities are required due to detector constraints. However, under such conditions the beam monitoring detectors, used in clinics, are not able to provide the beam characteristics due to the low signal produced in the detectors. The MIMOSA-28 sensors are intended to be used for beam monitoring in the frame of this work to evaluate the beam profiles when performing experiments at low intensities. A stand alone online tool for beam monitoring, with the use

of MIMOSA-28, was then important to be developed. From this online beam monitoring, a real time information of the beam characteristics can be provided.

The characterization of pencil beams for clinical applications was performed at low intensity with the use of several MIMOSA-28 sensors placed along the beam axis. This measurement method aims to provide the beam divergence and angular distribution in both lateral directions. In a treatment room, the beam profile is well defined at the isocenter position. However, since the particle beam is non-parallel, the beam profile varies along the longitudinal axis. This work also aims to determine the lateral beam spread along the beam axis, by using the transport code SCATTMAN [5, 10], based on the ion optical parameters of a non-parallel beam.

The MIMOSA-28 could also be exploited for another clinical application related to the patient positioning using fiducial markers. For particle therapy treatment, one crucial step is the precise positioning of the patient inside the treatment room. A small mispositioning of the patient can lead to range shifts of the particle beam, creating under- and overdosage inside the tumor and organs at risk, respectively. The patient is precisely positioned in the treatment room, in most cases, by means of the bony structure position of the patient visible on the daily imaging method. However, for the case of interfractional moving tumors, fiducial markers are used for image guidance. These markers are implanted inside or close to the tumor volume and are composed of materials dense enough to be visible on the different imaging methods used during the patient treatment. Even though, the fiducial markers are small (< 0.5 mm diameter), they induce dose inhomogeneities due to edge-scattering effects. Several studies have been performed with Monte Carlo simulations and experimental measurements using radiochromic films. The latter experiments mainly investigated proton beams and were only performed at some positions along the beam axis. The aim of this work is to provide a measurement method that delivers a three dimensional fluence (respectively dose) distribution to quantify precisely fluence perturbations due to fiducial markers. With such purpose, the measurements were intended to be performed with a tracker system composed of several MIMOSA-28 sensors. This new measurement concept was first tested with the use of thick targets to verify the usability of the method and was later applied to fiducial markers commercially available. Through this concept, the maximum perturbation can be quantified as well as its position along the beam axis.

This manuscript is divided in four chapters. The first one describes the scientific background behind charged particle therapy with the physical and biological aspects necessary for the elaboration of a precise treatment plan. It also comprises the description of tumor movements and the methods used to compensate the uncertainties coming from these motions. In the second chapter, the CMOS pixel sensor MIMOSA-28 used during the different experiments as well as the optimization of the experimental setup are described. In the third part, the beam time campaigns performed at different facilities are detailed with a description of the experimental setups and the methods employed for the data analysis. In the last chapter, the results obtained from this work are described and discussed.

Chapter 1

Ion-beam therapy

This chapter describes the scientific background of particle therapy, the properties of heavy charged particles and their advantages for radiotherapy applications. A short history, relating the different discoveries that made possible cancer treatment with heavy ions, introduces the chapter. The physical and biological aspects necessary for planning cancer therapy are explained, followed by several descriptions of the treatment complexities and the use of fiducial markers for image guidance in particle therapy.

1.1 History

1.1.1 From X-rays to heavy-ion therapy

Radiotherapy for cancer treatment started in the 19$^{\text{th}}$ century, shortly after the discovery of X-rays in 1895 when Röntgen was operating a Crookes tube and observed that a nearby screen was glowing [11]. In the same year, Becquerel discovered the phenomena of radioactivity [12], followed by that of the Curies of the Radium in 1898 [13]. From these findings, the use of X-rays and radium for treating diseases were considered [14]. During the first decades, the notion of dose was not clear and the measurement methods were not reliable. Biological effects were not well understood at that time, which led to high morbidity and poor results [15].
From the 1920s, several discoveries significantly improved the results of radiotherapy. First, with the invention of Coolidge in 1913 [16], the X-ray energies could reach 180–200 kV. In the same era, the dose was quantified and its physical units defined as the *röntgen* followed by the *rad*. After series of experiments, fractionated radiotherapy showed its benefits with a better repair of the healthy tissues. Based on the Coolidge X-ray tube, linear accelerators were developed in 1928 by Wideröe where energies higher than 500 kV could be reached [17]. The invention of the electrostatic generator, with megavoltage potential by Van de Graaf in 1929 [18], led to the development of the first cyclotron by Lawrence in 1932 [19]. In parallel, neutron radiation for medical treatment was used after its discovery in 1932 by Chadwick [20]. Electrons also became an option for radiotherapy after the development of the first betatron in 1940 by Kerst [21]. During the following years, medical research was sidelined due to World War II. However, important achievements during this period were made with the development of a new particle accelerator type: the synchrotron [22].

From the 1950s until mid of 1980s, the need of techniques for treating tumors located in deep tissues pushed the development of cobalt therapy [23] and linear electron accelerators [24]. A greater penetration depth was thus possible to reach, improving the skin sparing. However, X-rays and gamma rays were difficult to control since they pass through the patient, leading to overdoses in healthy tissues. Multifield irradiation was introduced by the medical physicists but the lack of tumor control was still present. Over the years, treatment plans based on intensity modulated radiotherapy (IMRT) [25] were computed, yielding a better control and conformity of the dose inside the tumor volume.
Within a century of research from laboratories and clinics, several developments continuously improved patient treatments by delivering a more conformal dose to the tumor and minimizing the secondary effects.

1.1.2 History of Ion-beam therapy

The construction of the first cyclotron in 1932 enabled the acceleration of charged particles to over a million electron volts for the first time, with the acceleration of protons to 1.22 MeV. In 1939, larger machines were built, able to accelerate deuterons to 20 MeV and alpha particles to 40 MeV [26]. Heavy ions for radiotherapy applications were first considered in 1946 when Wilson investigated the depth-dose profile of proton beams [27].
A couple of years later, the first synchrotron for medical purpose was built at Lawrence Berkeley Laboratory in USA, where experiments were performed to study the physical and biological properties of proton beams [28]. In 1954, patient treatments started with protons followed by helium ions. Several years later, heavier particles and in particular 670 MeV/u ^{20}Ne ions, produced at the Bevalac in Berkeley, were used due to their strong biological effects and low oxygen enhancement ratio [29].
A variety of beam delivery techniques were also developed, such as passive beam shaping, collimators and modulators [30] and several medical facilities using mainly proton beams were constructed in the world [31]. When sufficient computer resources were available, three dimensional computed tomography (CT) imaging could be performed, improving the treatment planning capabilities [32]. Patient positioning techniques were developed [33] for proton therapy since higher precision was required due to the sharp dose fall-off of protons compared to photons.
In 1994, the Heavy Ion Medical Accelerator (HIMAC) [34] was built at the National Institute of Radiological Science (NIRS) in Japan, delivering carbon ion beams using innovative beam delivery techniques by means of passive systems. Advanced techniques were developed with the implementation of active beam scanning using spot scanning [35] at the Paul-Scherrer-Institute (PSI) in Switzerland and raster scanning [36] at the Helmholtzzentrum für Schwerionenforschung (GSI) in Germany. The latter became a pioneer in heavy ion-beam therapy from 1997 on, when a pilot project was conducted until 2008 with the use of carbon ions for the first time in Europe, under the leadership of Pr. Gerhard Kraft from the Biophysics department at GSI. For this project, the treatment planning system TRiP98 [37] (Treatment planning for particles, 1998 edition) was developed including the Local Effect Model (LEM) [38]. A raster scanning system was used for delivering precisely the dose to the tumor volume. An online Photon Emission Tomography (PET) system [39] was placed in-room and could measure the range of the ion beams shortly after the treatment. After ten years of clinical trials, more than 400 patients were successfully treated,

showing the benefit of carbon ion beams. Therefore, the Ion-beam Therapy Center in Heidelberg (HIT) was constructed as part of the university clinic Heidelberg with the help of GSI. The HIT facility and the treatment planning system used are based on the ones developed for the pilot project at GSI. But still, a lot of research is needed for better accuracy and precision of ion-beam therapy treatments.

1.2 General aspects

The main rationale of using heavy ions in tumor therapy compared to electromagnetic radiation (e.g., X-rays) relies on their favorable depth-dose profile [5]. In contrast to photons, used in conventional therapy, the dose of ions at the entrance channel is small and increases along their path until they release a maximum dose at the end of their range, forming a distinct and narrow peak called *Bragg peak*. In Figure 1.1, the depth-dose profiles of 6 MV photons, 170 MeV protons and 325 MeV/u carbon ions in water are illustrated. The primary energies of protons and carbon ions were chosen to adjust the Bragg peak position to 20 cm depth.

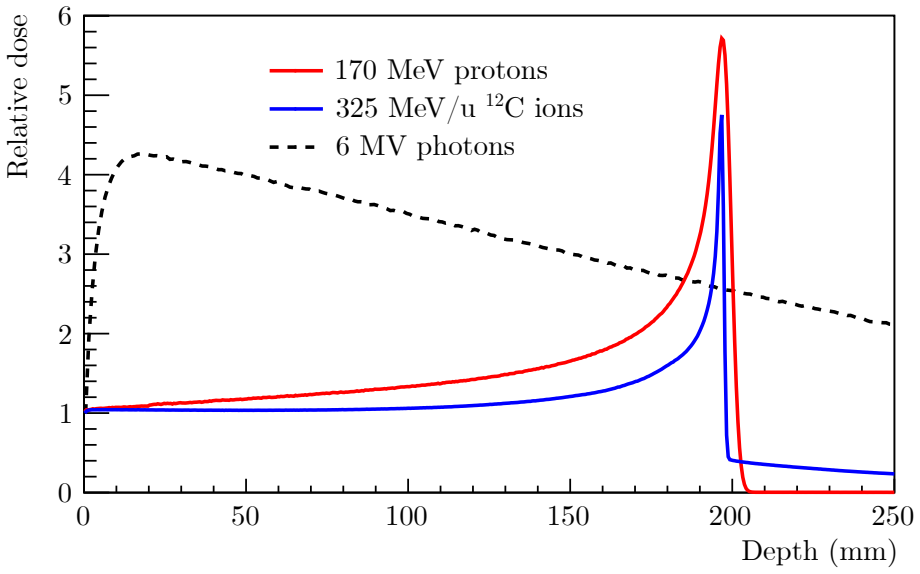

Figure 1.1: Depth-dose profiles of 6 MV photons (black dashed line), 170 MeV protons (red line) and 325 MeV/u carbon ions (blue line) in water simulated with the GEANT4 version 10.05 Monte Carlo code. For the photon curve, an energy-fluence spectrum was simulated using the data set from a 6 MV Varian Linac [40].

The position of the Bragg peak can be precisely adjusted to the proper depth by varying the energy of the incident ions. By superimposing single energy irradiations, a spread out Bragg peak (SOBP) can be created and a uniform dose can be delivered over a target volume by means of a single field irradiation, but typically more than one field are used in particle therapy. Figure 1.2 shows a SOBP created with carbon ions is shown, covering 5 cm in depth.

In the past years, innovative techniques such as raster scanning were developed, permitting the modulation of beam energies and intensities within a short time. Intensity modulated particle therapy (IMPT) uses several irradiation fields, where the dose can be modulated and optimized for all fields enabling the treatment complex tumor volumes with high precision. To fully exploit the physical advantages of ion-beam therapy, high precision is an absolute necessity during all steps. Therefore, several aspects such as precise patient positioning, beam monitoring and treatment planning system database need to be accurate.

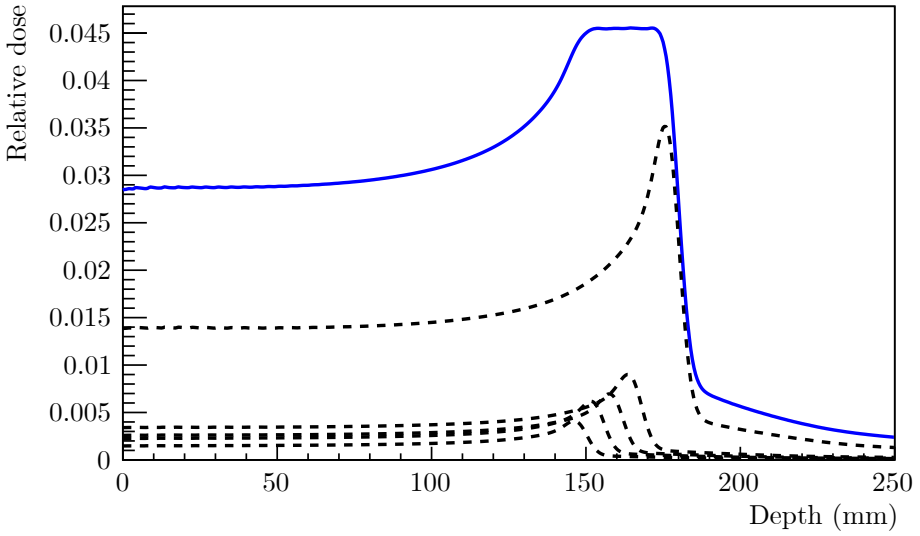

Figure 1.2: Spread out Bragg peak (SOBP) created with carbon ions in water, covering 5 cm in depth. The pristine Bragg curves (black dashed lines) are superimposed to obtain the SOBP (blue line). The data were generated with the Monte Carlo code FLUKA [41]. A ripple filter was included in the simulation in order to reduce the number of energy steps. Data courtesy of Dr. Felix Horst.

1.3 Physical aspects

1.3.1 Interaction mechanisms

A charged particle passing through matter interacts via different mechanisms. To deliver a conformal dose to the patient, it is necessary to consider the different mechanisms that are responsible for this dose. In particle therapy, three main processes are relevant: the elastic Coulomb interactions with the nucleus, the inelastic Coulomb interactions with the atomic electrons and the inelastic nuclear interactions (Figure 1.3).

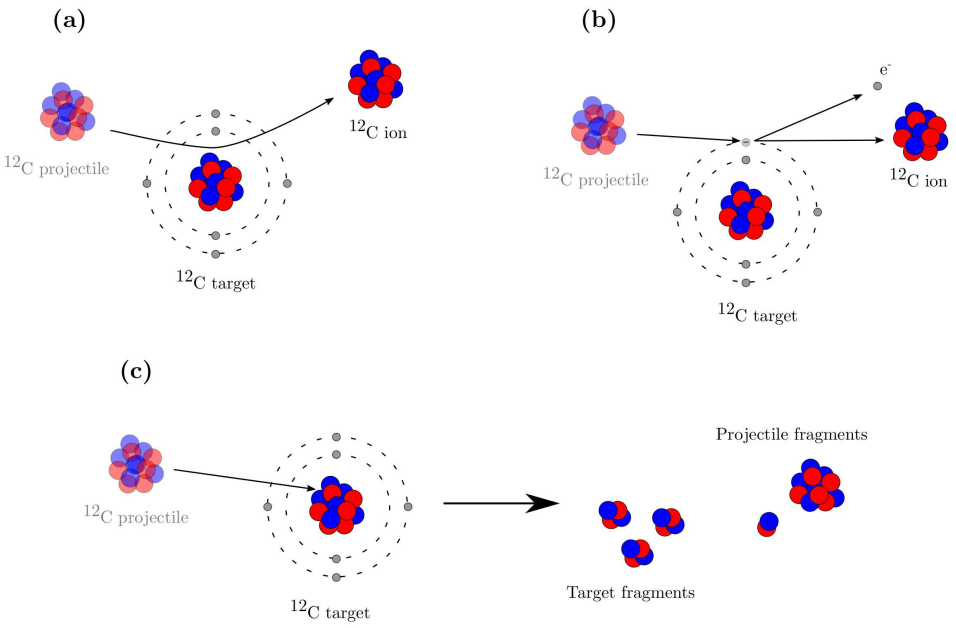

Figure 1.3: Interaction mechanisms relevant for particle therapy with the example of a ^{12}C projectile interacting with a ^{12}C target. The elastic and inelastic Coulomb interactions are represented in panels (a) and (b), while the inelastic nuclear interaction is illustrated in panel (c). Figure inspired by [42].

1.3.1.1 Elastic Coulomb interactions

When a heavy charged particle passes through a medium, it undergoes elastic Coulomb interactions and is slightly deflected by a few mrad due to a repulsive force with the target nuclei. This interaction is sketched in Figure 1.3 (a), and is responsible for the lateral spread of the beam, explained in section 1.3.4.

1.3.1.2 Inelastic Coulomb interactions

Inelastic Coulomb interactions are due to the attractive Coulomb force between the positively charged projectile and the target atoms. In such collisions, the energy transfer of the primary ion to the atom causes an *ionization* or *excitation* process. Figure 1.3 (b) illustrates an inelastic interaction leading to the ionization of the target atoms. The ejected electrons can undergo a large impulse and have enough energy to create further ionizations. In such case, these high energetic liberated electrons are called δ-*electrons*. Inelastic Coulomb interactions are mainly responsible for the energy deposition of the particle inside a medium, detailed in section 1.3.2.

1.3.1.3 Inelastic nuclear interactions

Inelastic nuclear interactions are less likely than the interactions described above, but their contribution to the dose in a target volume is not negligible. Peripheral collisions are the most frequent nuclear reactions and lead to the loss of one or several nucleons of the primary ion. Nuclear fragmentation can yield *projectile* and *target fragments*, as illustrated in Figure 1.3 (c), which also contribute to the dose inside the target. The probability for a certain reaction to occur, due to inelastic nuclear interaction, is defined by its cross section, described in section 1.3.6. For heavy ions, with atomic number $Z > 2$, these collisions are well described by the *abrasion-ablation* model [43, 44] that is a two-step process. In the first one, an overlap zone is defined where the projectile and target nucleons are abraded, forming a *fireball* while the remaining projectile and target pieces of the non-overlapping zone are the *spectators*. In the next step, the fireball and spectators deexcite by evaporation of nucleons, protons and light nuclei as well as the emission of photons. In the case of protons and helium ions, this model is not valid anymore. For protons at therapeutic energies, only target fragments are produced during nuclear interactions while the secondary protons are deflected [42]. For helium ions, the nuclear fragmentation follows a one-step process due to its unique internal structure. The different interactions of helium ions are well described by Cucinotta et al. (1993) [45].

1.3.2 Energy deposition

A heavy charged particle passing through matter mainly loses its energy by electronic interactions with the atoms of the medium. The energy loss per unit path length, also called *stopping power*, depends on the energy and type of the projectile and on the characteristics of the target material. When traversing a medium, the particle beam slows down until it loses a maximum energy at the end of its path before dropping down to zero (Figure 1.1), induced by inelastic interactions with the target electrons (section 1.3.1.2). The curve describing the trend of the energy loss per unit path length is called *Bragg curve* and can be calculated using the Bethe-Bloch formula [46, 47]:

$$-\frac{dE}{dx} = 4\pi N_A r_e^2 m_e c^2 \rho \frac{Z}{A}\frac{z^2}{\beta^2}\left[\ln\frac{2m_e c^2\gamma^2\beta^2}{I} - \beta^2 - \frac{\delta}{2} - \frac{C}{Z}\right] , \tag{1.1}$$

where the parameters are listed in Table 1.1.

The energy loss per unit path length of a heavy charged particle is proportional to the square of the projectile charge z and increases with the slowing down of the particle due to the velocity parameter of the projectile β. This means that for heavier ions than protons such as carbon ions, the energy loss is higher for the same traveled distance and increases along its path. Equation 1.1 is valid for high energy particles that are fully stripped [48]. For lower energies than 1 MeV/u, the energy loss of the projectile becomes smaller due to the decrease of the effective charge when the primary particle captures the absorber electrons. The atomic number of the projectile z in Equation 1.1 is thus replaced by the effective charge z_{eff} and can be approximated with the Barkas formula [49] as:

$$z_{eff} = z\left[1 - \exp\left(-125\beta z^{-\frac{2}{3}}\right)\right] . \tag{1.2}$$

Table 1.1: Variables used in the Bethe-Bloch formula.

Symbol	Definition	Units or Value
N_A	Avogadro's number	6.022×10^{23} mol^{-1}
r_e	Classical electron radius	2.818 fm
$m_e c^2$	Electron mass $\times$ c^2	0.511 MeV
ρ	Density of absorber	g/cm^3
Z	Atomic number of absorber	
A	Atomic mass of absorber	
z	Charge of incident particle	
β	Velocity parameter of incident particle v/c	
γ	Lorentz factor $1/\sqrt{1-\beta^2}$	
I	Mean excitation potential of absorbing material	eV
δ	Density correction	
C	Shell correction	

The stopping power of different ion beams in water as a function of their kinetic energy is illustrated in Figure 1.4.

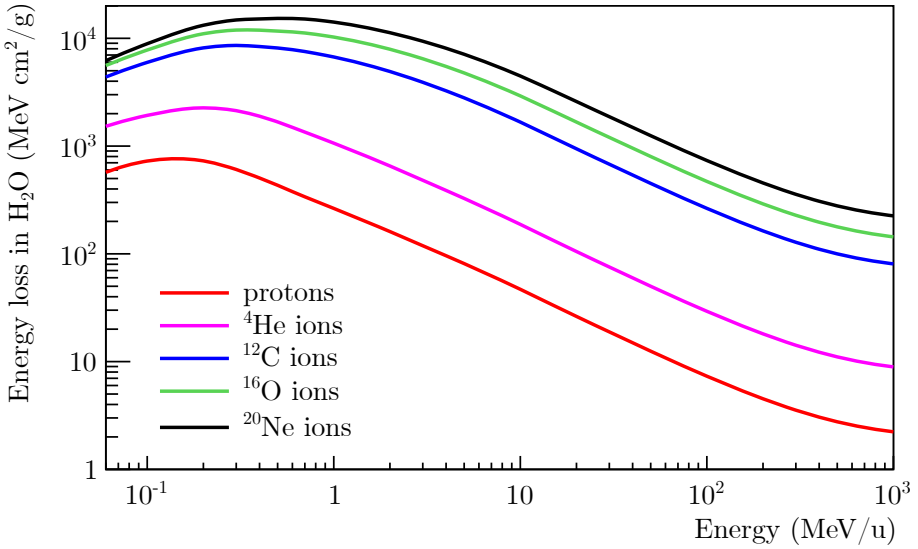

Figure 1.4: Stopping power as a function of the energy for protons (red line), ^{4}He (magenta line), ^{12}C (blue line), ^{16}O (green line) and ^{20}Ne (black line) ions in water. The energy loss values were calculated using LISE++ [50].

1.3.3 Mean range & energy straggling

As explained in the previous section, the energy loss function, described by the Bethe-Bloch formula (equation 1.1), shows a narrow peak just before that the primary ion stops in the medium. Since the interaction processes with the target material occur in a statistical way, the energy loss varies for each independent particle. This effect is called *energy-loss straggling* and induces a broadening of the Bragg peak.
The range of a particle is defined as the path length traveled in a given absorber until it comes to rest. In reality, the particle follows a complex path due to multiple Coulomb scattering. However, the latter effect is relatively small for heavy charged particles and the total path length can be approximated by a straight line. Even though the multiple scattering is not relevant for this range, a *range straggling* effect arises due to the stochastic variations of the energy loss. For simple applications, these fluctuations can be neglected and the range R of a particle at a given energy can be approximated by the continuous slowing down approximation (CSDA) [51], and is calculated by integrating the reciprocal energy loss per unit path length $\mathrm{d}E/\mathrm{d}x$ over the full energy range:

$$R = \int_0^{E_0} \left(\frac{\mathrm{d}E}{\mathrm{d}x}\right)^{-1} \mathrm{d}E \,. \tag{1.3}$$

For a given velocity and for a same medium, the CSDA range is proportional to A/z^2, which means that in general, the heavier the particle is, the smaller is the range, except for protons and helium ions that have the same range. The CSDA range in water as a function of the energy for different ion species is illustrated in Figure 1.5.

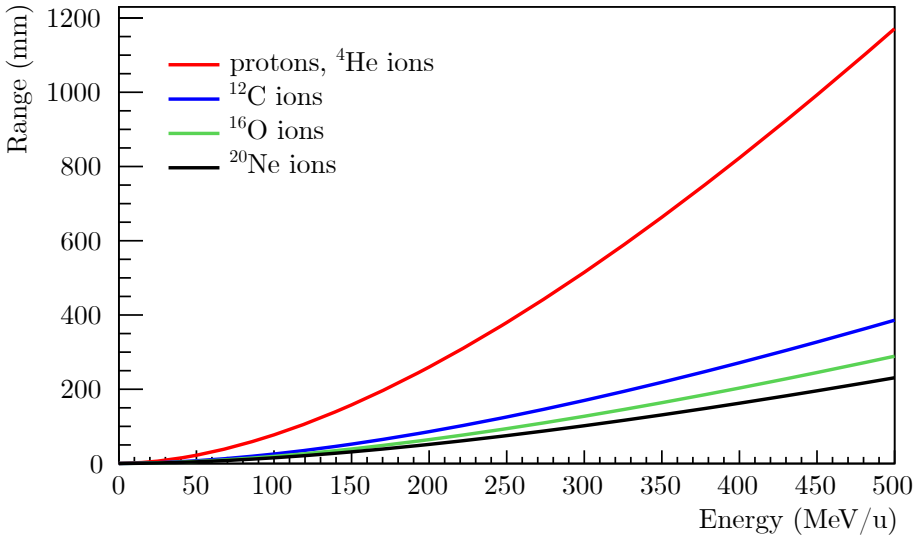

Figure 1.5: CSDA range in water as a function of the energy for protons (red line), ^{4}He (red line), ^{12}C (blue line), ^{16}O (green line) and ^{20}Ne (black line) ions. The range values were calculated with LISE++ [50].

1.3.4 Lateral beam spread

The deflections of ions, due to multiple Coulomb scattering, are accurately described by the *Molière's theory* [52]. The latter is algebraically complicated and can be approximated by a Gaussian distribution much easier to evaluate. The angular width of the Gaussian distribution σ_α, given in mrad, can be defined by the Highland approximation [53, 54]:

$$\sigma_\alpha = \frac{14.1}{\beta pc}\, z \sqrt{\frac{\rho d}{L_{rad}}} \left[1 + \frac{1}{9}\log_{10}\left(\frac{\rho d}{L_{rad}}\right)\right], \tag{1.4}$$

where p is the projectile momentum and ρ, d and L_{rad} are the density in g/cm^3, the thickness in cm and the radiation length in g/cm^2 of the absorber, respectively.
The Highland formula scales with z/A of the projectile, which means that the multiple scattering is stronger for protons than carbon ions at a given energy. Heavy absorber materials induce stronger deflections than lighter ones for a given thickness. Figure 1.6 illustrates the FWHM of several pencil beams as a function of the depth, for protons and carbon ions at therapeutic energies.

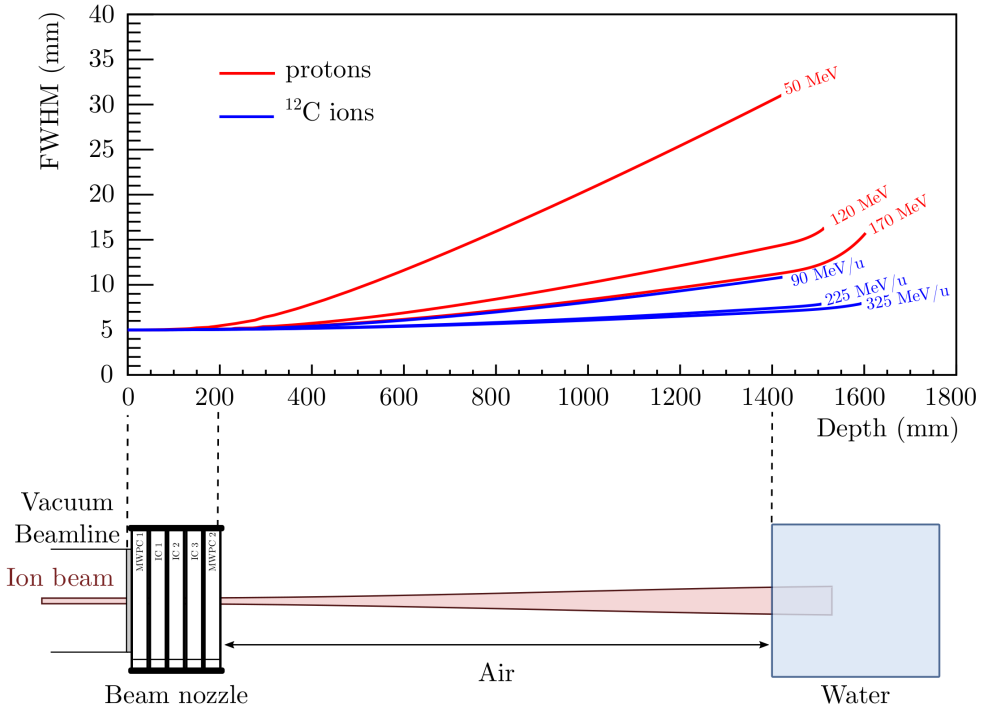

Figure 1.6: Lateral beam width as a function of the depth for protons (red lines) and carbon ions (blue lines) at different energies (top panel) for a setup representing a clinical case (bottom panel). The initial FWHM was set to 5 mm and the position 0 mm represents the exit window position. The calculations were performed with the transport code SCATTMAN [5, 10].

The FWHM was evaluated by the analytical code SCATTMAN [5, 10], described in section 3.4.2.1, which transports the particle based on the multiple Coulomb scattering calculated by the Highland approximation (equation 1.4). For the calculations presented in Figure 1.6, a 5 mm FWHM parallel pencil beam passes through a set of detectors, called *beam nozzle*, and impinges a water phantom of 40 cm thickness, which fully stops the particle beam. The beam nozzle represents the beam monitoring system used in the therapy centers in Heidelberg (HIT) and Marburg (MIT) and has a water equivalent length of 2 mm. As shown in Figure 1.6 (top panel), protons scatter more than carbon ions for a given range. For a certain ion species, the scattering becomes stronger when the particle energy decreases. To correctly estimate the multiple scattering, it is necessary to take into account the energy loss of the primary beam along its path. The strong rise of the beam width at the end of its range is due to the decrease of the particle energy, especially when impinging on the water phantom.

1.3.5 Edge-scattering effects

A particle beam passing perpendicularly through strong density gradients and edges suffers inhomogeneous scattering, creating then an over- and undershoot. In Figure 1.7, the basic principle of edge-scattering effects induced by a target with a sharp edge is depicted. This figure was obtained by analytical calculations of several overlapping Gaussian beams that are differently scattered.

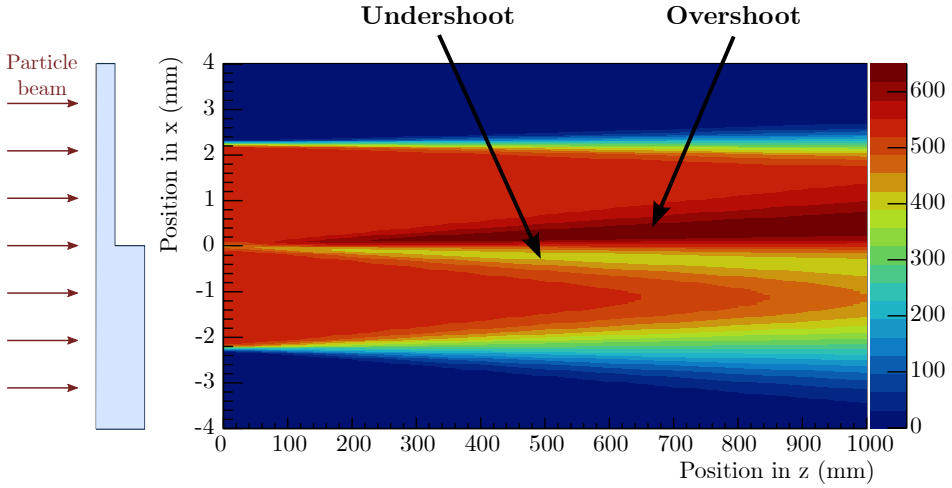

Figure 1.7: Inhomogeneous scattering of a beam particle passing through strong density gradients and sharp edges. The fluence perturbation from edge-scattering effects creates an under- and overshoot behind the target.

The strength of the perturbation due to edge-scattering effects depends on several parameters relative to the beam and to the density gradient. On the one hand, high density and thick target materials induce strong particle deflections due to multiple Coulomb scattering. On the other hand, the lower and the lighter the beam energy and particle species are,

the larger is the scattering effect. Consequently, a particle beam of a given energy, passing through high density gradients from a target placed inside a certain medium, suffers stronger perturbations than for low density gradients. The position of the perturbation behind the target also depends on these parameters: for small deflections, the over- and undershoot are created at further positions than for strong deflections.

1.3.6 Cross section

The inelastic collisions between two nuclei, presented in section 1.3.1.3, can be described in terms of *cross section*. The latter quantifies the probability of a reaction to occur per unit area, given in barn. When a primary beam impinges a thin target, particles are scattered out within a certain solid angle. The *differential cross section* is given as followed [55]:

$$\frac{\mathrm{d}\sigma}{\mathrm{d}\Omega}(E,\Omega) = \frac{1}{\Phi}\,\frac{\mathrm{d}N}{\mathrm{d}\Omega}\,, \tag{1.5}$$

where $\mathrm{d}\sigma/\mathrm{d}\Omega$ represents the fraction of particles $\mathrm{d}N$ scattered into the solid angle $\mathrm{d}\Omega$ per unit fluence Φ. This value varies as a function of the primary beam energy and the scattered angle. The *total cross section* of a reaction at a given energy is calculated by integrating equation 1.5 over all solid angles:

$$\mathrm{d}\sigma(E) = \int \frac{\mathrm{d}\sigma}{\mathrm{d}\Omega}\,\mathrm{d}\Omega\,, \tag{1.6}$$

Cross section measurements are essential for transport codes applied to ion-beam therapy. Semi-empirical models are used to describe total cross sections as a function of the charge and mass of the projectile and target, and also depend on the energy of the colliding system. The parametrization in these models is well characterized by means of experimental data. The geometrical model based on the Bradt-Peters formula [56], and enhanced with the consideration of the energy dependence [57], describes the total reaction cross section σ_R as follows:

$$\sigma_R = \pi\, r_0^2\, c_1(E)\, (A_P^{1/3} + A_T^{1/3} - c_2(E))^2\,, \tag{1.7}$$

where $r_0 \approx 1.2$ fm is the nucleon radius used for the calculation of the nuclear radius as $r = r_0 \cdot A^{1/3}$. The A_P and A_T terms represent the mass number of the projectile and target, respectively, and $c_1(E)$ and $c_2(E)$ are energy-dependent parameters. As explained in section 1.3.1.3, nuclear collisions produce fragments that contribute to the dose. Moreover, they have different biological effects than the primary beam, which need to be considered in order to deliver a conformal dose to the patient. Several studies have been performed to measure cross sections of different reactions (e.g., Dudouet et al. (2013) [58] and Horst et al. (2017) [59]) as well as secondary fragment yields and angular distributions (e.g., Haettner et al. (2006) [60] and Haettner et al. (2013) [61]) in order to tune the models used for particle transport calculations.

1.3.7 Absorbed dose

The *absorbed dose* or *physical dose* is defined as the mean energy deposited $\mathrm{d}E$ per mass element $\mathrm{d}m$ [62]:

$$D = \frac{\mathrm{d}E}{\mathrm{d}m} \,, \tag{1.8}$$

where D is given in Gray (1 Gy = 1 J/kg). Considering the energy loss per path length from equation 1.1, the absorbed dose can be calculated as:

$$D = 1.6 \cdot 10^{-9} \; \Phi \; \frac{\mathrm{d}E}{\mathrm{d}x} \; \frac{1}{\rho} \,, \tag{1.9}$$

where Φ is the fluence of the primary beam per unit area in cm^{-2}, and ρ is the density of the target material in $\mathrm{g/cm}^3$. The linear energy transfer (LET), given in keV/µm, is defined as the energy locally deposited per path length [63] and is similar to the electronic stopping power described in equation 1.1. The latter determines the ability of an absorber to slow down a certain particle, while the LET corresponds to the energy transferred from the particle to the medium. The LET may refer to a *restricted stopping power* in the case that an energy cut-off Δ is applied to the produced δ-electrons and is defined as follows:

$$LET_\Delta = \frac{\mathrm{d}E_\Delta}{\mathrm{d}x} \,. \tag{1.10}$$

In the case of heavy charged particles, the LET_∞ ($\Delta \to \infty$) is practically identical to the electronic stopping power since radiative energy losses such as *bremsstrahlung* [55] are negligible. The LET influences the biological effects [64], detailed in the next section.

1.4 Biological aspects

The aim of radiotherapy is to inactivate and avoid the multiplication of tumor cells by damaging their deoxyribonucleic acid (DNA). The latter is comprised inside the cell nucleus of about 2 µm diameter for a total cell size of 20 µm diameter [65]. DNA damages can occur via *direct* or *indirect actions* [66]. In the case of direct damages, the produced δ-electrons interact immediately with the DNA structure by destroying its helix. For the case of indirect damages, a *free radical* is created, in most cases by creation of a group hydroxyl through hydrolysis of water, and can diffuse far enough to damage the DNA structure.
Lesions of the DNA can be induced either through base or strand damages. In the first case, the DNA structure is damaged with the loss or the modification of a base. In the second case, two main break types can occur: the single strand break (SSB) and the double strand break (DSB), which are simple and more complex lesions, respectively.
Cells have different ways to repair ionizing radiation-induced damages depending on the type of lesion. In the case of base damages and SSBs, the DNA can be repaired without errors due to the simplicity of the lesions. For DSB cases, and especially spatially clustered DSBs, the damage can be complex enough that no available mechanisms can repair the DNA successfully. In such case, cell mutations can happen or the cell dies and cannot multiply anymore.

1.4.1 Track structure

The track structure of a particle determines its spatial energy distribution at a microscopic level. Another characteristic of heavy charged particles compared to photons, in addition to their depth-dose profile (Figure 1.1), is their advantageous track structure for tumor therapy. For high energy photons, produced by a linear accelerator, photoelectric effect and Compton scattering processes dominate [5]. The photons interact with the target electrons of the medium that damage the DNA. Electromagnetic radiation produces then *indirect ionizations* while heavy charged particles can also create *direct ionizations*. In the case of photons, the interaction processes happen with low probability and the number of indirect ionizations per cell is small. In the case of heavy charged particles, ionizations have a high probability, and the track is denser.

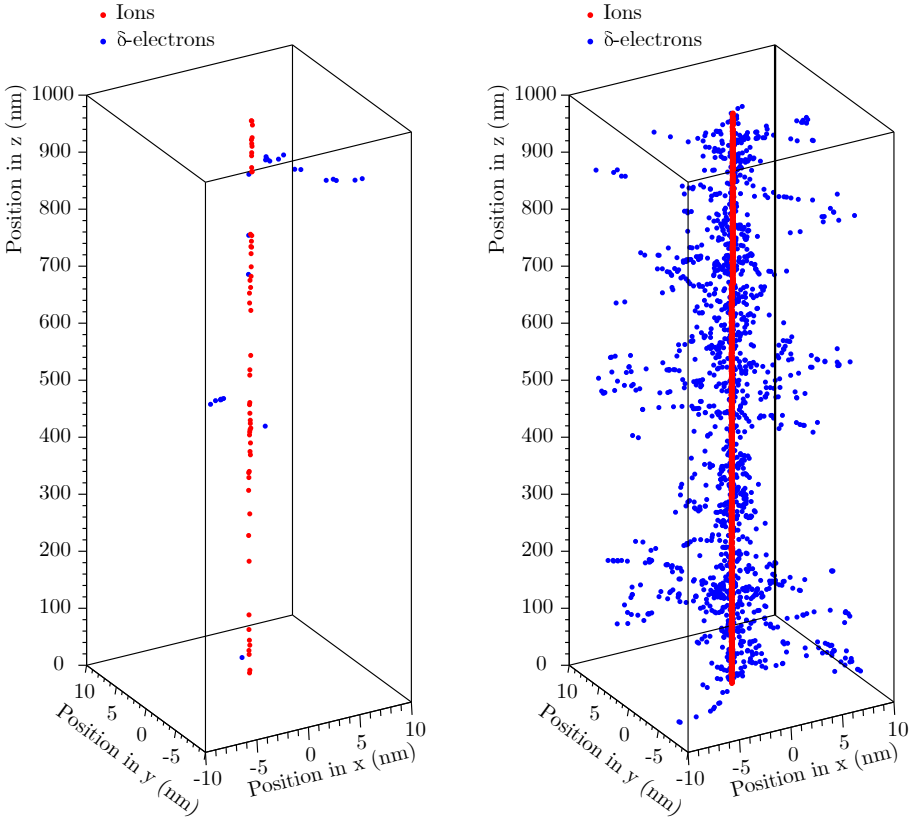

Figure 1.8: Track structure of a proton (left panel) and a carbon ion (right panel) at 10 MeV/u in water. The red points describe the ionizations due to the primary particle while the blue points are the ionizations created by the secondary δ-electrons. The simulations were performed with the Monte Carlo transport code TRAX [67]. Data courtesy of Dr. Daria Boscolo.

Electromagnetic radiations are thus defined as low-LET radiations due to their sparsely ionizing property, while heavy charged particles are considered as high-LET radiations since they produce dense tracks. The track density, which defines the spatial energy distribution,

also varies as a function of the particle type and energy. In Figure 1.8, the track structures, of a proton (left panel) and a carbon ion (right panel) at 10 MeV/u in a water medium, are illustrated. The spatial energy distribution influences the biological effects on the cells. It is thus an essential criterion to take into account for the optimization of the delivered dose to the patient.

1.4.2 Biological effects

Since the track structure from ionizing particles varies as a function of the ion species and energy, the biological effects depend strongly on the ionization density around the particle trajectory [68]. As the number of ionizations increases for ions compared to photons, the probability of creating complex DNA damages is enhanced. For densely ionizing particles, such as carbon ions, the number of DSBs increases, which leads to higher biological effects. To study these effects, cell survival curves as a function of the absorbed dose are established [69]. The *linear-quadratic model* is the most common parametrization for cell survival S and is given as the following:

$$S = \exp(-\alpha D - \beta D^2) \,, \tag{1.11}$$

where D is the absorbed dose and α and β are the linear and quadratic parameters, which are experimentally determined. In this model, the linear and quadratic components α and β scale with the dose and the square of the dose, respectively. One of the most common interpretation explains that for low doses, cell death by single hits are responsible for the linear component while for high doses, the multiple hits for cell killing may result from the interaction of different particles describing the quadratic component [70]. The two contributions of cell killing are identical for a dose equal to the α/β ratio. The latter is an important criterion for cell killing and influences the repair process of the cells. A small α/β ratio is connected to a pronounced shoulder of the survival curve and a high radioresistance. For sensitive cell lines, the shoulder of the survival curve is less pronounced and is defined by a large α/β ratio.
The relative biological effectiveness (RBE) is the quantity that defines the biological effects and is defined as follows:

$$RBE = \frac{D_{ref}}{D_{ion}} \,, \tag{1.12}$$

where D_{ion} is the ion dose needed to create the same biological effect as the reference dose D_{ref} applied with photons. The RBE can be determined from survival curves (Figure 1.9 (left panel)), and is commonly shown as a function of the deposited energy per path length illustrated in Figure 1.9 (right panel).

The biological effectiveness increases for high-LET radiation until reaching a saturation point, where it decreases again due to overkill effect. For protons, the RBE value is considered as 1.1 [71]. For carbon ions, this quantity varies significantly along its path and can be calculated based on different models such as the Local Effect Model (LEM) developed at GSI [38]. Additionally, the LET of carbon ions where the RBE is maximum corresponds to the LET at the Bragg peak position [72]. The RBE is a complex biological quantity, which depends on the particle species, energy and absorbed dose but also on the

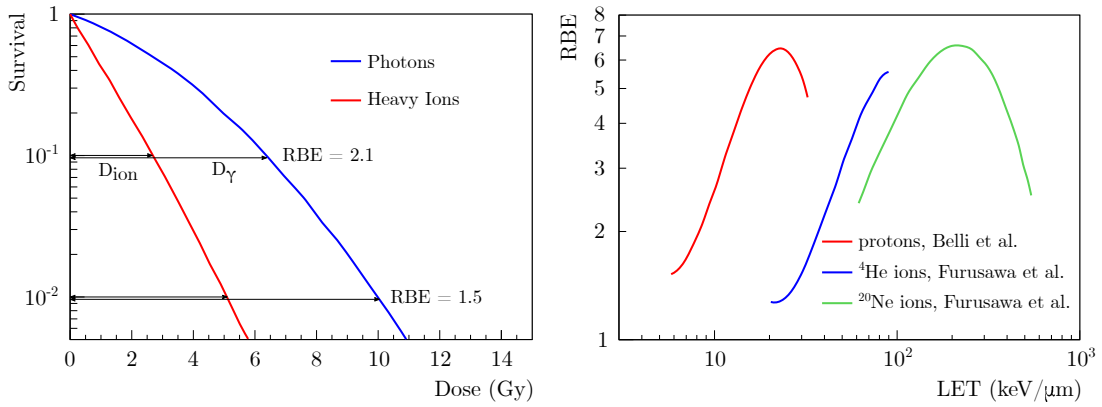

Figure 1.9: Survival curves as a function of the absorbed dose are displayed in the left panel for photons (blue line) and heavy ions (red line). The right panel illustrates the RBE as a function of the LET for protons (red line), ^{4}He ions (blue line) and ^{20}Ne ions (green line). Data redrawn from [5].

cell line and oxygenation level. Tumors in hypoxic conditions are more radio-resistant; therefore, heavy particles such as carbon ions seem to be more efficient in the treatment.

1.5 Treatment procedure

The aim of tumor treatment is to establish the best possible procedure to ensure the killing of the tumor and to spare the surrounding healthy tissues. With this purpose, diagnostic tools are used to evaluate the specific patient case and to decide whether to employ radiotherapy for tumor treatment. In such a case, several steps are followed to precisely and efficiently remove the tumor.

1.5.1 Planning CT & volume definitions

In a first step, a three dimensional (3D) computed tomography (CT) is performed for the patient in the same conditions than the later treatment. From the treatment planning CT information, the physician can delineate the gross tumor volume (GTV). The clinical target volume (CTV) includes the GTV and the microscopic spread of the disease. The physician prescribes the dose that needs to be delivered to the tumor and additional constraints to organs at risk (OAR). The treatment planning CT serves as a representation for the treatment delivery and is included into the treatment planning system (TPS). The latter takes into account the beam specific information such as particle ranges, deposited energies and beam angles as well as patient geometry to design the best possible treatment.

Patient positioning, inter- and intrafractional motions lead to uncertainties on the delivered dose. The TPS also considers these uncertainties related to the shift of the tumor during the treatment compared to the tumor position on the planning CT. Therefore, safety margins are applied around the target volume to ensure that the whole CTV is covered. The target volume with the applied margins is called planning target volume (PTV).

1.5.2 Treatment planning systems

The TPS calculations are normally performed using a pencil beam algorithm for dose optimization. Nowadays, TPSs based on Monte Carlo (MC) transport codes are also used. They lead to more accurate dose optimization but are also more time consuming. During the pilot project at GSI, mentioned in section 1.1.2, the TPS TRiP98 [37, 73] was developed for the use of carbon ions, delivered with a raster scanning system. This TPS considers both absorbed dose and *biological dose*. TRiP98 resulted to successful patient treatments and was later used as base for the commercial TPS from Siemens.
Pencil beam algorithms are based on basic data, provided by MC simulations or by transport codes, and include depth-dose profiles, lateral dose distributions, fragmentation processes and RBE tables. The biological dose D_{biol} at position $\overrightarrow{r}$ can be calculated as the following [74]:

$$D_{biol}(\overrightarrow{r}) = \sum_{z=1}^{z_p} \int_0^{E_{max}} \Phi(z, E, \overrightarrow{r})\ LET(z, E)\ RBE(z, E)\ \frac{1}{\rho(\overrightarrow{r})}\ \mathrm{d}E\ , \tag{1.13}$$

where Φ is the particle fluence of the primary ions and all fragments of energy E and ρ is the target material density. The biological dose is optimized according to the prescribed dose given by the radio-oncologist for covering the target volume and spare the healthy tissues. The RBE is determined for each particle, energy and tissue, based on a table containing values calculated beforehand with a modeling code.
In Figure 1.10, a treatment plan for a head and neck tumor was calculated by using photons (left panel) and carbon ions (right panel). Both plans were computed with the software matRad [75] for a single fraction dose of 2.3 GyE in the main PTV and 2.1 GyE in the second PTV, with a total dose of 70 GyE and 63 GyE, respectively, delivered in 30 fractions. This comparison demonstrate that a better dose conformality can be achieved with ^{12}C ions than with photons. In the latter case, the left parotid (white contours) needed to be irradiated for a homogeneous dose in the PTV while in the case of carbon ions, both parotids could be spared.

In ion-beam therapy, a verification of the plan is typically performed before the patient treatment. For this, the planned treatment is delivered to a water phantom, and the dose conformality is verified with several detectors such as ionization chambers.

1.5.3 Treatment delivery & Tumor control

The patient receives the treatment delivered in a number of fractions that was specified from the clinician and optimized by the TPS. Typically, the radiotherapy treatment is performed over several weeks. During this time, the patient plan can be re-evaluated to

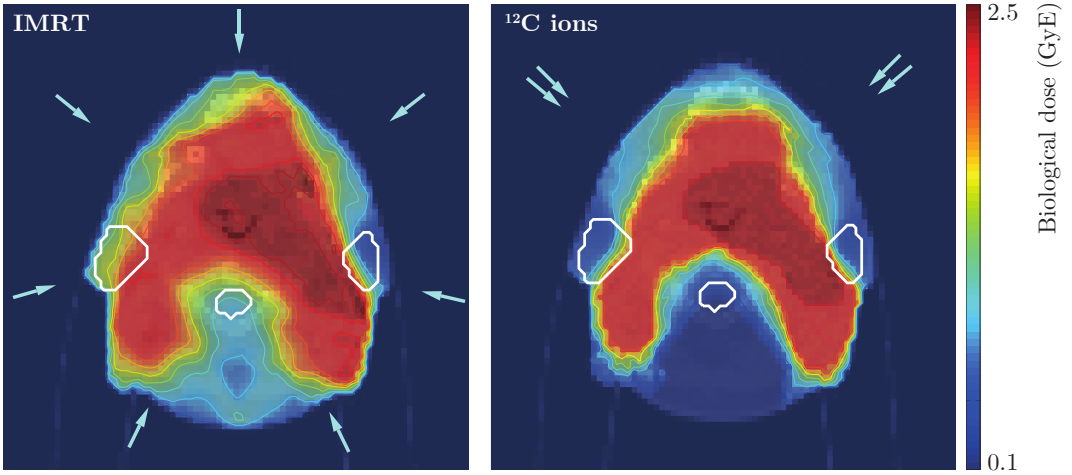

Figure 1.10: Treatment plan delivering a homogeneous dose to a head and neck tumor with the use of photons (left panel) and carbon ions (right panel). The blue arrows indicate the field orientations, with the use of seven fields in the case of photons and four fields in the case of carbon ions. The white contour lines mark the OARs with two parotids and the spinal cord. Both plans were computed with the software matRad [75]. Image courtesy of Dr. Athena Paz.

ensure that the treatment is still appropriate to the tumor characteristics such as its size and to verify the unexpected toxicities. In case large differences are found, compared to the original planning, a new planning CT is performed and a new treatment plan is calculated. At the beginning of every fraction, the patient is precisely positioned in the treatment room to guaranty a reproducible treatment.
Magnetic resonance imaging (MRI) is used to follow up the patient treatment, by verifying that the tumor has shrunk and is not regrowing. The control of the patient is usually done during a period of 5 years after the end of the treatment, in general every 6 months, to verify that there is no recurrence from the tumor.

1.6 Interfractional tumor motions

Ion-beam therapy can deliver conformal doses with sharp dose fall-off to complex target volumes. For static targets, range uncertainties can be estimated and the irradiated volume is delimited in order to cover the full tumor. Patient positioning is one of the most important steps during the patient treatment and is optimized by using several methods to precisely align the patient with respect to the beam axis. Several studies have investigated inter- and intrafractional motions as well as the patient positioning [76]. In this section, the use of fiducial markers for image guidance of interfractional organ motions and their dosimetric consequences are introduced.

1.6.1 Patient positioning

To cover the target volume with the prescribed dose and to spare healthy tissues, the patient must be aligned compared to the beam axis with high precision to minimize range and lateral uncertainties. These uncertainties have a stronger impact for ion beams than for photons, and a mispositioning of the patient can lead to severe underdosage in the tumor and overdosage in the healthy tissues. In this case, tumor recurrence could occur and organs at risk could receive unwanted doses. The patient is generally treated for several weeks and needs to be precisely positioned each day of the treatment. Systematic and statistical patient setup errors need to be taken into account for the treatment. Systematic uncertainties describe all causes for changes in the patient position, shape and size, for instance, weight change and target average displacement during the treatment. Statistical patient setup errors define unpredictable interfractional changes of the patient positioning due to mechanical fluctuations related to the treatment equipment or the setup methodology used for the daily treatment. At the beginning of every fraction, the patient is fixed to the couch through several methods, such as using a stereotactic mask for the treatment of brain or head and neck tumors. A 3D image such as cone beam computed tomography (CBCT) or a two dimensional (2D) X-ray projection image is recorded to verify the position of the patient. The daily image is used to compare the position of the patient with the CT recorded for the treatment plan by checking, for example, the bony structure position. With this information, the patient can be re-aligned with a precision better than 1 mm [77] compared to the absolute coordinates system of the treatment room, and therefore to the beam axis.

1.6.2 Fiducial markers for image guidance

In some cases, the tumor can move between two consecutive fractions due to anatomical changes. For instance, several studies showed that the prostate may move in the range of 0–2 cm in-between the fractions [78, 79, 80], due to the filling of the bladder and the rectum with an average displacement of around 5 mm. For such motions, the bony structures of the patient can not be used anymore for precise positioning. Therefore, fiducial markers are used to verify the interfractional tumor displacements. The markers are surgically implanted inside or at the border of the tumor before the treatment, and their positions are recorded during the treatment planning CT. They are used to verify the tumor movement by comparing their positions on the planning CT, and the daily image performed most of the time by X-ray projections. In case the fiducial markers indicate a significant movement of the tumor, the treatment can be stopped and a new treatment planning CT will be recorded in order to re-calculate a proper treatment plan with the new tumor position. The spatial stability of the fiducial markers was investigated with two or three implanted markers [81]. In 99% of all cases, their movement was smaller than 4 mm.
Fiducial markers must respect three essential criteria. First, they should produce low streak artifacts on the treatment planning CT [82] to not induce wrong density information, which could lead to a wrongly calculated dose distribution. Secondly, they must be visible on the different daily imaging methods used for the patient positioning [83]. The last criterion is that fiducial markers should produce a low dose perturbation during the radiotherapy treatment [84]. As described in section 1.3.5, a particle beam suffers inhomogeneous scattering when passing through strong density gradients and edges, creating

fluence perturbations. Since the dose scales with the fluence, the edge-scattering effects induce cold and hot spots in terms of dose. Therefore, fiducial markers can cause unwanted dose inhomogeneities. To fulfill the above criteria, size and shape of the fiducial markers as well as the Z and ρ of the material need to be optimized.

1.6.3 Dose perturbations due to fiducial markers

During the last years, mainly high density (e.g., gold) and relatively large (> 1 mm diameter) fiducial markers were used for position verification since they can easily be seen on the X-ray projection. However, these types of markers induce significant artifacts on CTs [83] and also cause cold and hot spots (dose perturbations) during the treatment due to inhomogeneous scattering of the particle beam. Other markers with lower density and atomic number (e.g., carbon-coated ZrO_2) can reduce these inhomogeneities. However, they are not always visible on the X-ray projection performed during the daily treatment. It is also important to note that the fractionation of the treatment will lead to a wash-out of the dose inhomogeneities produced behind the fiducial markers.
Several studies investigated the severeness of the dose perturbations induced by fiducial markers with MC simulations [84, 85, 86] and/or measurements performed with radiochromic films [87, 88]. These studies have demonstrated that the dose perturbations depend on the marker material, thickness, position and orientation inside the phantom. The bigger and heavier the material is, the stronger is the inhomogeneous scattering effect, which creates thus larger and stronger cold and hot spots. Another MC simulation study showed that the dose perturbations due to the markers could be partly reduced using several fields [89]. The measurements performed with radiochromic films were mainly done for proton beams and with several films placed along the beam axis. However, it is difficult to predict where to place them exactly along the longitudinal axis to precisely measure the maximum dose perturbation induced by the markers.

Chapter 2

CMOS pixel sensors: MIMOSA-28

This chapter relates in a first part the general characteristics of CMOS pixel sensors and the evolution of the MAPS generation for particle tracking purpose. In a second part, the MIMOSA-28 pixel sensor used in this work is described, followed by a section explaining the detector characterization and the mechanical setup optimization, performed during this PhD thesis.

2.1 CMOS pixel sensors

In the field of particle physics, single-sided microstrip detectors were initially used as vertex detectors in collider and fixed target experiments [90]. This type of semiconductor detector is fabricated through a planar process by oxide passivation, photo engraving and ion implantation [91]. The growing requirements for high precision tracking in particle physics, such as the study of short-lived particles and the high particle collision rates, pushed the development of high granularity pixel detectors, able to detect multiple tracks with high spatial and time resolution. One of the proposed candidate to fulfill these requirements was a monolithic active pixel sensor (MAPS) [6], based on complementary metal-oxide-semiconductor (CMOS) technology.

2.1.1 General aspects

Semiconductor materials are such that their electrical conductivity is between the one of a conductor material and the one of an insulator material. The detection principle of semiconductors is the same as e.g., gas-filled ionization chambers. The energy needed to create an electron–hole pair in such a chamber is about 20 eV while only 3.6 eV is required for silicon material. This has the advantage that semiconductors have a better energy resolution.
The conductivity can be modified by introducing impurities (doping) into the semiconductor, either by adding electrons (n-type) or holes (p-type). A pn-junction is an interface between p-type and n-type semiconductors creating an electric field at the boundary region. Metal-oxide-semiconductor field-effect transistors (MOSFET or MOS) are a common semiconductor device used in the electronics industry. They consist of a metal gate, an oxide insulation and a semiconductor, and are composed of four different terminals: the

source (S), the drain (D), the grid (D) and the substrate (B). The MOSFETs can be used in different operation modes depending on the applied voltage between the source and the drain: the weak-inversion mode, the linear mode and the saturation mode. MOS transistors can be either p-type (p-MOS) or n-type (n-MOS), and the combination of both types is called CMOS. This technology is used for different electronic components, but also for active-pixel sensors (CMOS sensors).
Originally used as an alternative to charge-couple devices (CCDs) in image sensors [92], CMOS detectors were proposed for particle tracking in the field of particle physics, and also were of interest for medical physics applications, with the development of MAPSs. The latter are composed of a low-resistivity monolithic epitaxial layer with an embedded amplifier per pixel to buffer the output signal. MAPSs became attractive with their good compromise between granularity, readout speed, material budget, radiation tolerance and power dissipation.

2.1.2 Charged particle detection

Monolithic CMOS sensors are composed of a thin epitaxial layer moderately p-doped (P−) located between a highly p-doped substrate (P++) and P-well (P++). A pn-junction is created between the epitaxial layer and the implanted N-well (N++) in the top of each pixel, creating a collection diode. When a particle traverses the sensor, electron-hole pairs are produced by ionization and trapped in the epitaxial layer. Since the epitaxial layer is not fully depleted, the electrons diffuse thermally and are collected by the N-well region of the pixel. Because of the different doping concentrations of the layers, build-in voltages are induced at the boundaries of the epitaxial layer with the substrate and the N-well, which allow the electrons to move towards the collection diode. The signal is then stored in a diode-parasitic capacitance before being amplified for each pixel. A schematic cross-section of a monolithic active pixel sensor is sketched in Figure 2.1.

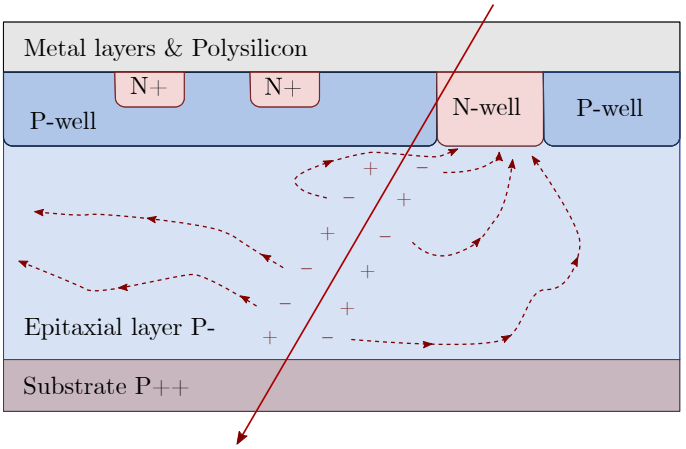

Figure 2.1: Schematic cross-section of a monolithic active pixel sensor for charged particle detection. Ionization processes occur after the passage of a charged particle inside the epitaxial layer. The produced electrons diffuse thermally (red dotted lines), and are collected by the N-well diode. Figure redrawn from [93].

2.1.3 Evolution of Mimosa sensors

In 1999, a first prototype of MAPS, called Mimosa (Minimum Ionizing particle MOS Active Pixel Sensor)-1, was designed for particle tracking applications [94]. This prototype sensor was fabricated in AMS-0.6 µm CMOS process with an epitaxial layer of 15 µm, and was an analog sensor made of four matrix arrays of 64 × 64 pixels each with a pitch of 20 µm. Even though the collection process was dominated by thermal diffusion, a charge collection of about 1000 electrons by 3 × 3 pixels in less than 100 ns was obtained with simulated and experimental data [95]. The tracking performance of this first prototype was evaluated for a high energy beam, yielding a detection efficiency close to 100% and a signal to noise ratio (SNR) of 30 [96]. The potential of this prototype pushed the research and development of several other prototypes based on CMOS processes, leading to the design of Mimosa-5. This sensor was the first device in wafer scale composed of four matrix arrays of 510 × 512 pixels each one, and a pixel pitch of 17 µm [97]. These analog sensors showed good performance for particle tracking with a single point resolution $\sim$ 2 µm [98]. The readout time per frame of such pixel detectors was in the range of 1–10 ms.
During the following years, several prototypes of Mimosa, mainly fabricated in AMS-0.35 µm CMOS process, were initially developed for the vertex detector [99, 100, 101] of the STAR experiment at RHIC and the International Linear Collider (ILC) [102]. This new sensor generation was equipped with a more complex electronics with an in-pixel amplification and correlated double sampling (CDS), to suppress the pixel-to-pixel pedestal variations [103]. The differential output signal was read out in parallel by column-level discrimination with offset compensation [104]. These MAPS also integrated a binary output, improving significantly the readout speed of the detector [105]. The study of the charge collection and SNR as a function of the integrated radiation dose for different pitch sizes showed that reducing the pitch from 40 to 20 µm improved the radiation hardness of the sensor significantly [106].
In 2006, the EUDET-JRA1 project (Detector R&D programme for a future international linear collider) [107] was proposed to provide a test beam area for a telescope of high resolution pixel sensors, located at the facility in DESY near Hamburg (Germany). Mimosa-16 was the first prototype for this project, using the architecture of Mimosa-8 with a new pixel design [108]. The promising results of this prototype were followed by the fabrication of a larger sensor, Mimosa-22, with $\sim$ 25 mm^2 active area. Mimosa-22 was characterized and showed good performance with a high spatial resolution, good detection efficiency and low noise [109]. Nevertheless, a concern about the radiation hardness led to the development of other sensors, investigating different pixel architectures and the epitaxial layer resistivity [110]. The requirements for the EUDET project and the STAR vertex detector also needed a fast readout with integrated zero suppression to reduce the data flow [111]. After successful achievements [112], the full scale sensor Mimosa-26 was fabricated within the EUDET project. This reticular sensor was composed of 576 × 1152 pixels, with a pitch of 18.4 µm and a readout time $\leqslant$ 200 µs [113]. The detection performance of this sensor was assessed with minimum ionizing particles. Several tests were performed at the CERN-SPS with a 120 GeV π^- beam [114], resulting in a low temporal noise, a low fake rate, a detection efficiency $\sim$ 99.5% and a single point resolution better than 3 µm. Another full scale sensor Mimosa-28, based on the Mimosa-26 architecture and optimized for the STAR experiment [115, 116], was the first vertex detector based on CMOS technology. The physics run in 2014 for the STAR experiment [117, 118] at RHIC validated the use of MAPS

as vertex detectors. Since then, CMOS pixel sensors also became of interest in the field of applied physics: MIMOSA-26 was used during the FIRST experiment [119, 120] with heavy charged particle, and MIMOSA-28 is foreseen to be used in the FOOT experiment [121] for ion-beam therapy and space radiation applications. Nowadays, silicon sensors have become a standard for vertex detectors in high energy physics [122]. Further designs of CMOS pixel sensors are exploited [123] in order to provide adequate performance required for different experiments such as the ALICE [124] inner tracking system upgrade at CERN [125, 126] or the micro-vertex detector of the future Compressed Baryon Matter (CBM) experiment at FAIR [127].

2.2 MIMOSA-28

MIMOSA-28 (or ULTIMATE) [7] is fabricated in AMS-0.35 µm CMOS process, using 4 metal- and 2 polylayers. It is composed of 928 rows × 960 columns with a square pixel of 20.7 µm pitch covering an active area of ~ 3.8 cm^2.

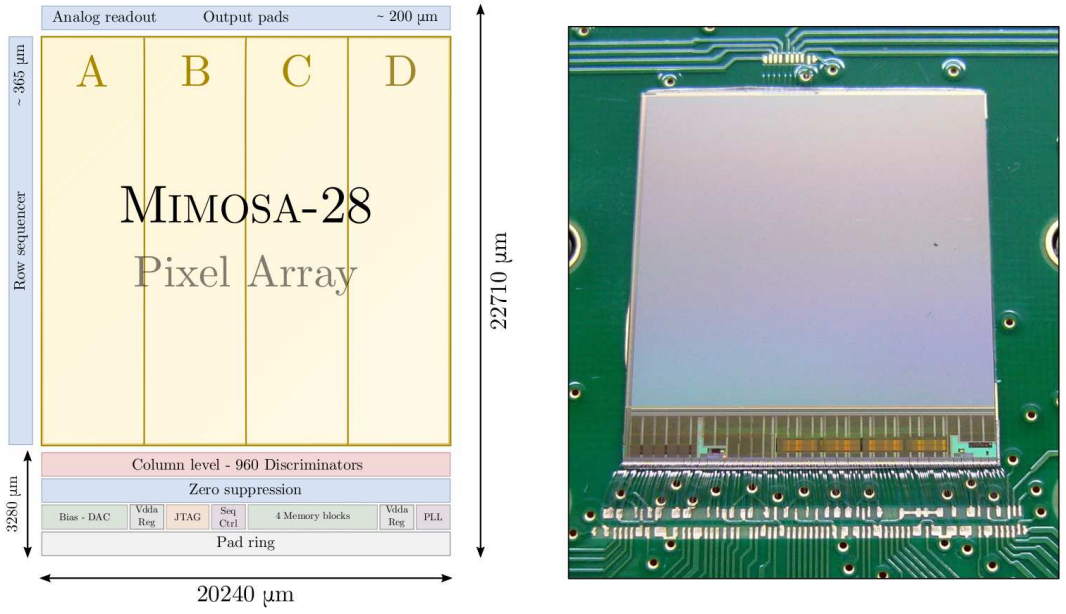

Figure 2.2: Functional block diagram of MIMOSA-28 pixel sensor (left panel). Figure redrawn from [7]. Picture of MIMOSA-28 pixel sensor (right panel).

Figure 2.2 (left panel) represents the functional block diagram of MIMOSA-28 sensor and Figure 2.2 (right panel) shows a picture of the sensor. This sensor has a total thickness of 50 µm with a high resistivity epitaxial layer (> 400 Ω·cm) of 14 µm. Each pixel integrates an amplifier and a CDS, improving the SNR. MIMOSA-28 is read out line by line in rolling shutter mode with column-level discrimination delivering a binary signal, and has an integration time of 186.5 µs. The output signal is then processed by zero suppression, where only signals from the fired pixels are registered. The performance of MIMOSA-28

was evaluated with a 120 GeV π^- beam, where the single point resolution of the detector was found to be better than 4 µm [7]. At room temperature, the power dissipation of the chip is around 150 mW/cm^2 and the fake hit rate per readout frame is $< 10^{-4}$ for a threshold set at five times the noise. The radiation tolerance of this sensor is around 150 krad (or 1500 Gy) for ionizing dose, which means that the sensor could be damaged after some hours of irradiation in clinical conditions. However, for the primary beam energies and intensities used in this work, the sensor could be continuously operated for some years without serious effect. The non-ionizing damaging fluence has been proven to be 3×10^{12} n_{eq}/cm^2 for MIMOSA-28.

2.2.1 Architecture

2.2.1.1 Pixel

The pixel architecture of the ULTIMATE sensor is described in Figure 2.3 (left panel). The sensitive part is composed of a self-biased diode, where the reverse biased collection diode D_1 is reset by the forward biased diode D_2. The sensitive element and the amplification stage are biased with a common source. The load transistor amplifier M_2 is biased with another transistor M_3, increasing the gain about a factor 2 [128].

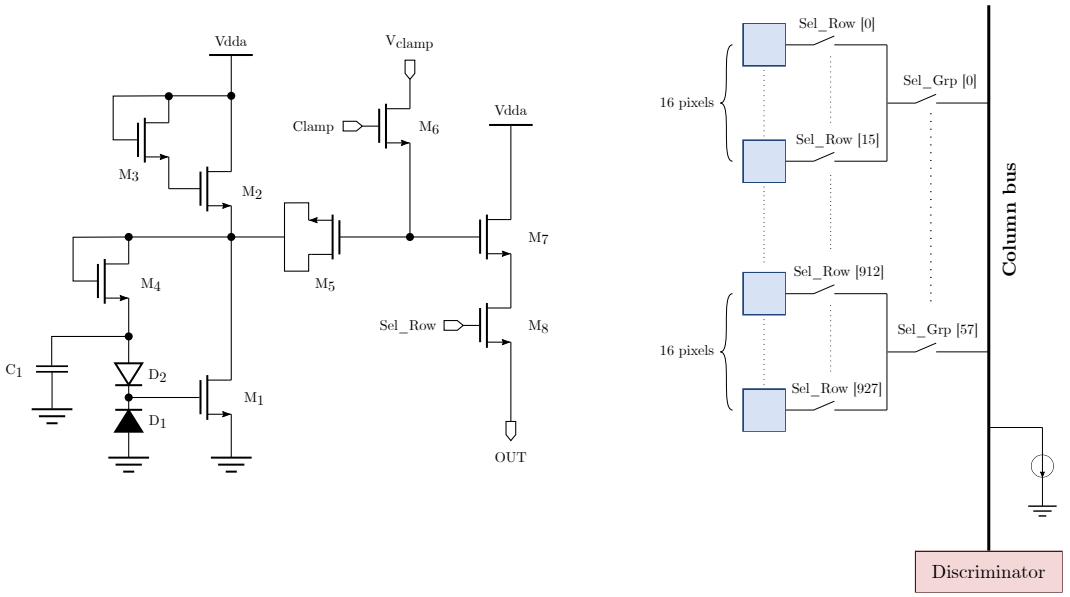

Figure 2.3: Schematics of the pixel architecture (left panel) and the connections of the pixel column to the discriminator (right panel) for MIMOSA-28. Figure redrawn from [7].

A feedback, creating a low-pass filter with a large time constant, is formed by the transistor M_4 and the capacitor C_1, compensating the leakage current of the diode D_1. The MOS capacitor M_5 and the MOS switch M_6 compose the CDS element, which removes the offset and reduces the noise due to the circuitry. This is done via resetting the clamping node at the gate M_7 to a pre-defined voltage at each readout cycle. The transistor M_7 is followed

by an output source follower M_8, whose current is provided by a current source, located at the end of the column and shared by all pixels inside the same column. To reduce the capacitance at the output node, each column is split in 58 groups of 16 pixels, and each group has a common switch (Figure 2.3 (right panel)).

2.2.1.2 Discriminator

To provide a high precision signal, the discriminator is based on a differential architecture (Figure 2.4 (top panel)) with offset compensation, and comprises three differential gain stages and a dynamic latch. The auto-zero functionality is performed via the two phases *Calib* and *Read*, where the amplifier offsets are first stored by the capacitors C_1, C_2, C_3 and C_4 to be then canceled in the second phase. The pixel output is reset by the *Clamp* signal, controlling the in-pixel CDS element. As observed on the time diagram sketched in Figure 2.4 (bottom panel), the pixel offset stored in the *Calib* phase is subtracted from the pixel output signal superimposed to the same offset recorded during the *Read* phase.

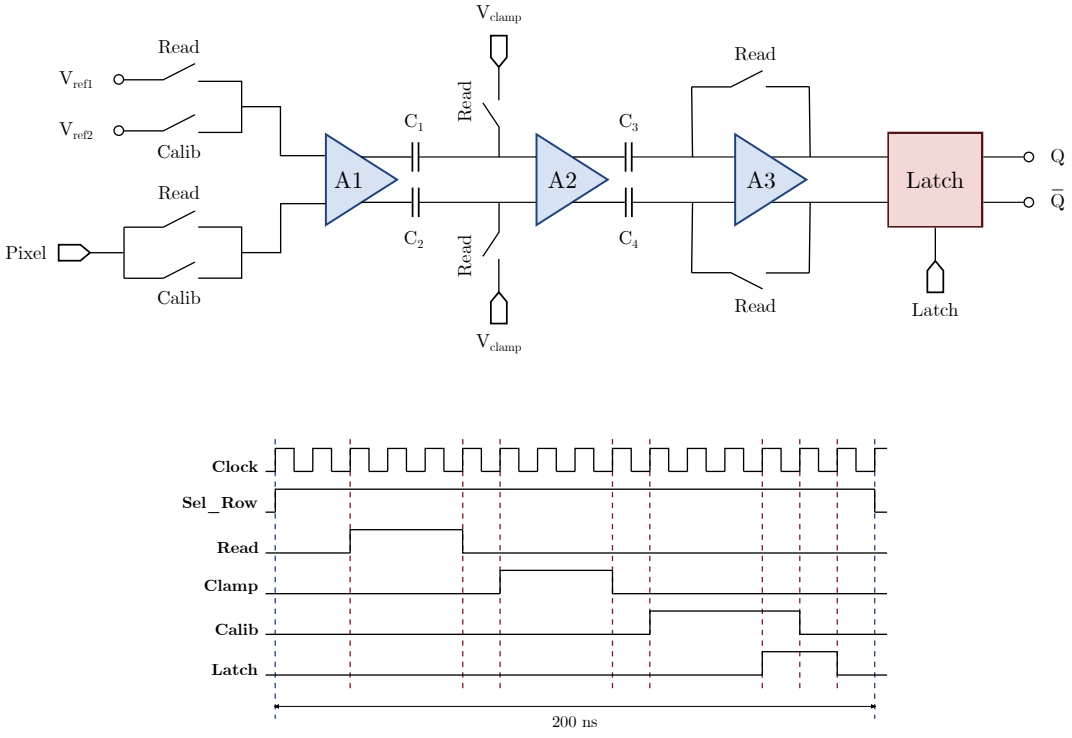

Figure 2.4: Schematics of the discriminator architecture (top panel) and the corresponding time diagram (bottom panel) of MIMOSA-28. Figure redrawn from [7].

The same operation is performed concerning the threshold signal, coming from the difference between V_{ref1} and V_{ref2} stored during the *Read* and *Calib* phases, respectively. During the *Latch* phase, the latch performs the difference between the pixel output signal and its corresponding threshold. The binary output signal is obtained after amplification and digitization of this difference.

A total of 960 discriminators are used in the MIMOSA-28, which can suffer from stray capacitance of the MOS devices used as switches. To ensure the minimization of these effects and reduce the capacitance of the output node, the sensor is divided in four blocks of 240 discriminators (Figure 2.2) with an adjustable threshold per block. By means of a characterization procedure, detailed in section 2.2.2, the noise levels of each block can be evaluated to later set appropriate threshold values to the sensor. The performance of MIMOSA-28, evaluated with minimum ionizing particles as a function of the noise threshold measured at 30°C, are represented in Figure 2.5.
For a threshold set at six times the noise value, a detection efficiency $\sim 100\%$ is found with a single point resolution < 4 µm, and a fake hit rate $< 10^{-6}$ per pixel per readout frame.

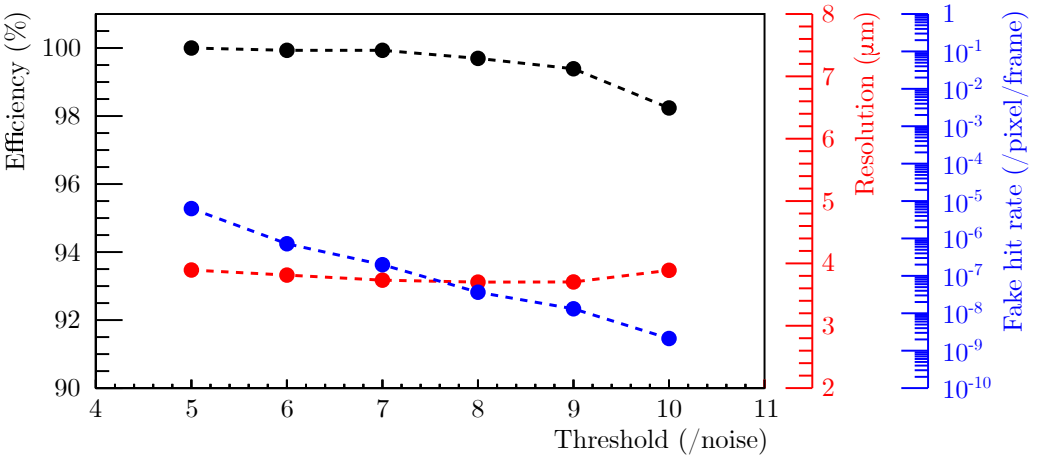

Figure 2.5: Performance of MIMOSA-28 as a function of the noise threshold measured at 30°C with minimum ionizing particles. The detection efficiency is shown in black, the single point resolution of the sensor is represented in red and the number of fake hits per pixel per readout frame is sketched in blue. Figure redrawn from [7].

2.2.1.3 Zero suppression

The data flow from such pixel detector can reach up to several Gbit/s, slowing down the readout speed. The ULTIMATE sensor is equipped with zero suppression, located at the end of the discriminators, and is based on a row by row sparse data scan readout in order to only store the information from the fired pixels. In a first stage, the digital signals are processed in parallel on 15 blocks of 64 columns. Each block describes 1 status group (4-bit), up to 6 states (11-bit per state), and 1 overlap (1-bit). The status group indicates the number of states for one block with its line address. A state contains the information of up to 4 contiguous fired pixels; the number of contiguous pixels are described by the first 2-bit, while the next 11-bit encode the column address of the first pixel. In a second stage, the outcome of the 15 blocks is read by a multiplexer composed of 3 different modules, resulting in 1 status and 9 states encoded on 16-bit each. The status contains the number of states and the line address, while each state contains the number of fired pixels and

the column address. In a last stage, data are stored in memory, containing 2 buffers to perform read and write operations, simultaneously, allowing a continuous readout of the sensor. The data are transmitted to the acquisition system via 2 low voltage differential signal (LVDS) outputs, with a frequency of 160 MHz. In Figure 2.6 (top panel), a sequence example of pixels fired from a line of one block is sketched. The middle and bottom panels describe the coding of the status and the state of the binary data, respectively.

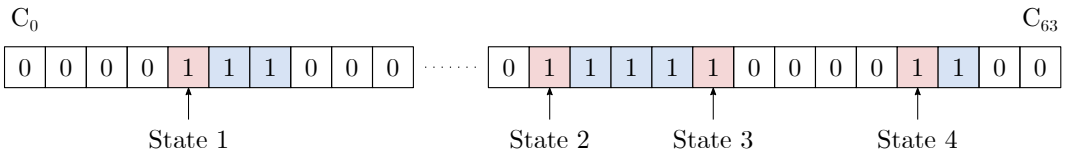

Status															
0	1	2	3	4	5	6	7	8	9	10	11	12	13	14	15
Number of states				Address of the line											Overflow

State															
0	1	2	3	4	5	6	7	8	9	10	11	12	13	14	15
Number of hits				Address of the column									Not used		

Figure 2.6: Coding of the binary data for MIMOSA-28 sensor. The top panel illustrates a sequence example of fired pixels from a line of one block. The middle panel describes the coding of a status, while the bottom panel describes the coding of a state.

2.2.2 Characterization

During the characterization of MIMOSA-28, it is possible to test the circuitry of the chip, to determine the number of broken pixels, and to verify the uniformity of the sensor response. This procedure also aims to determine the noise level of all pixels in order to apply consistent thresholds during operation. As explained in section 2.2.1.2, the sensor is divided in four groups, where the discriminator level of each group can be adjusted independently. With this purpose, the temporal and fixed pattern noise, resulting from the pixels combined with the discriminators, are measured for each group. In this work, the characterization of 12 MIMOSA-28 was performed at IPHC in Strasbourg. In Figure 2.7, the noise distributions are shown for one group of one sensor, resulting in a temporal noise of 1.02 mV, mainly coming from the pixel behavior, and determined by the mean value of the noise distribution (Figure 2.7 (a)). The fixed pattern noise of 0.54 mV is dominated by the discriminator dispersion, defined by the width of the threshold distribution (Figure 2.7 (b)). The threshold levels of all groups can be later set via a join test action group (JTAG).

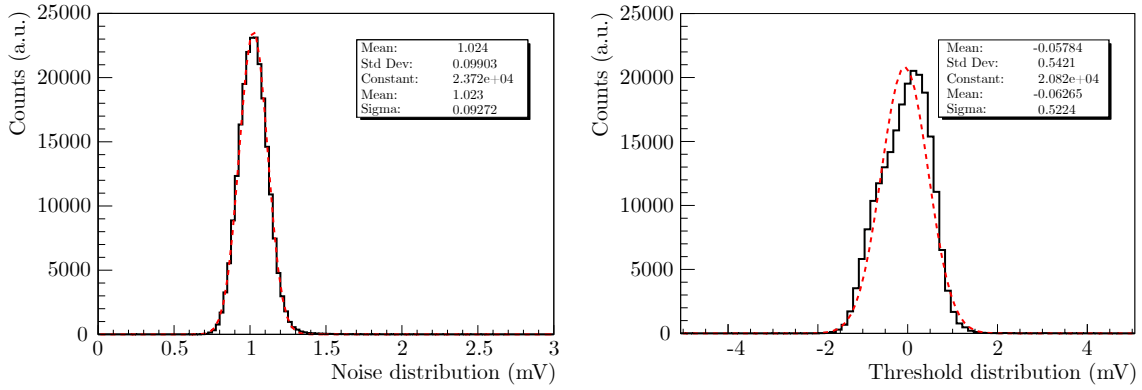

Figure 2.7: Temporal noise (left panel) and fixed pattern noise (right panel) distributions obtained from the characterization of MIMOSA-28. The red dotted line represents the Gaussian fit of the distribution.

In a previous study [9], the cluster size was investigated for the analog sensor MIMOSA-18 [129], and for the digital sensor MIMOSA-26 [113], with 80 MeV proton, and 80 and 400 MeV/u carbon ion beams. An empirical model was developed and used to fit the collected data of MIMOSA-18, expressing the cluster size as a function of the energy deposition. In this work, an extension of this study was performed with the MIMOSA-28 sensor. With this goal, two generations of MIMOSA-28 sensor were used, where the noise repartition of the sensor is distributed more uniformly in the second generation, after improvements implemented by the PICSEL group at IPHC in Strasbourg.

2.2.3 Data acquisition system

The data acquisition (DAQ) system uses the PXI platform, and is based on National Instruments (NI) hardware. The DAQ software used for ULTIMATE was developed in Labview [130], and the management of the DAQ operations is performed via a FlexRIO board driver. The JTAG protocol is generated on the CPU board parallel port in order to configure the sensors. The DAQ system is equipped with a field programmable gate arrays (FPGA) on a NI FlexRIO board and a NI LVDS adaptor module for the acquisition of serial data stream.
In Figure 2.8, a schematic of the DAQ system used to operate several MIMOSA-28 sensors is sketched. The sensor proximity printed circuit board (PCB) comprises four ports: the power connector supplying +5 V, the *JTAG* port to provide the slow control protocol for configuration, the *CTRL* port for the clock and synchronization and the *DATA* port for the clock, synchronization and data streaming. The JTAG protocol and the Control signals are provided by the DAQ system via a parallel port, and translated by the JTAG interface board into LVDS signals transmitted to the sensor via RJ45 connectors. The *DATA* port of the sensor is connected to a digital interface board via RJ45 connectors, while the connection between the interface board and the FlexRIO front-end module is done via VHDCI connectors. To be able to run more than one sensor at the same time, additional JTAG and CTRL distribution boards are needed.

To synchronize the readout of several MIMOSA-28 sensors, a specific starting procedure is followed. In a first step, the DAQ generates start and clock signals distributed to all sensors. The DAQ system receives then the clock and a synchronization signal from one of the sensors, provided via the digital interface board. In a last step, the 160 MHz clock is provided by the DAQ system to the *CTRL* connector through an adaptor card connected to the DAQ adaptor module via VHDCI cable. The recorded data are finally saved on a RAID of disk connected to the PXIe system.

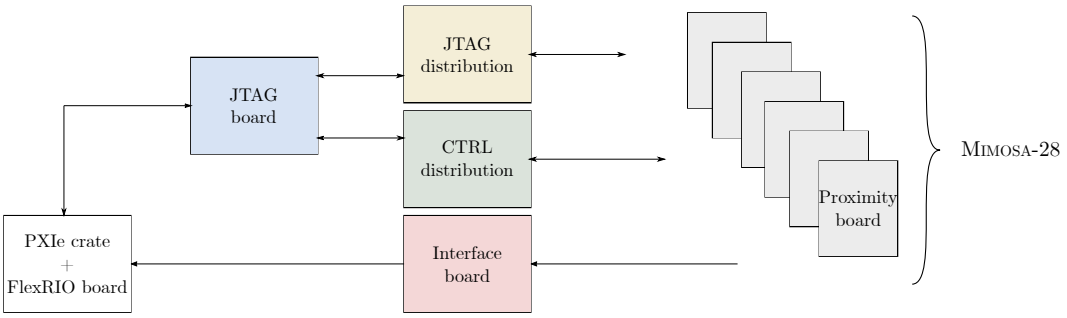

Figure 2.8: Schematic of the data acquisition system used for operating several MIMOSA-28 sensors.

2.3 Mechanical setup for MIMOSA-28

The mechanical stability of the setup is one of the main concerns for high spatial resolution pixel sensors, since small deviations can lead to severe problems during the data analysis. In this work, the mechanical setup for MIMOSA-28 has been optimized in order to perform experiments in different facilities. Main goals were having a setup relatively easy to handle, fast to mount and as stable as possible. The different parts detailed in this section were designed, in the frame of this work, with CATIA V5 [131], and manufactured by the mechanical workshop at GSI.

2.3.1 Sensor holder

The sensor holders were designed to be light-tight, and to tightly accommodate the proximity board. This brings stability to the system by restricting the sensor movements. Even though aluminum is a standard material used for shielding in different electrical applications, the sensor holders developed in this work are made of trubidur plastic (PVC). The reason for this choice was because plastic is a lighter material with small effective atomic number. This reduces unwanted secondary fragment production from the primary beam interactions with the holders. The latter are composed of one support part, where the sensor PCB can be fixed with five screws, and one cover part attached to the support. On both parts, two holes slightly bigger than the dimensions of the sensor were manufactured to remove any additional material in front and behind the sensor.

In Figure 2.9, a drawing of the holder, developed in this work, for MIMOSA-28 sensor is depicted. Antistatic black tape was used to cover the holes for making the holder light-tight.

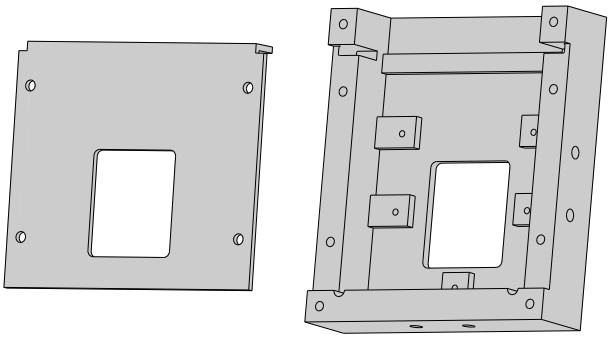

Figure 2.9: Holder for the MIMOSA-28 sensor, designed with CATIA V5 [131].

After being fixed inside their holder, the sensors were scanned with a resolution of 600 dpi to evaluate precisely their position compared to the holder dimensions. After analyzing the scanned images with ImageJ [132], the position (0,0) in x and y, defined as the center of the sensor, could be precisely quantified compared to the holder coordinates. To locate the sensor position in (x, y and z) inside its holder, marks were drawn on each holder, with a precision better than 0.5 mm.

2.3.2 Setup optimization

The complete setup to be mounted during an experiment for running ULTIMATE sensors is relatively complex. The DAQ system uses multiple boards and several tens of cables, as mentioned in the previous section. To optimize such a setup, it was necessary to employ a concept where the setup could be pre-cabled and prepared as compact as possible (Figure 2.10). In this work, the JTAG interface card, the two distribution boards, the adaptor card and the digital interface board were fitted inside a 19-inch rack drawer, with all cables and interconnections pre-connected. Several holes have been made on the front and back sides of the box to create an interface between all cards that will be connected to the PXIe crate and the sensors during the experiment. For this, RJ45 feed-through connectors were fixed in the front of the rack drawer.

For stability and precision purposes, the sensors are placed on an optical bench (Qioptic manufacturer). The RJ45 shielded cables attached to the sensor proximity boards are six meters long, which make them relatively heavy. To avoid any movement of the holder due to cable strain, each of them, as well as each power cable, is clamped to a cage built from aluminum profiles. In Figure 2.11, a picture of an experimental setup, using six MIMOSA-28 sensors, illustrates the different components used to improve the stability of the setup.

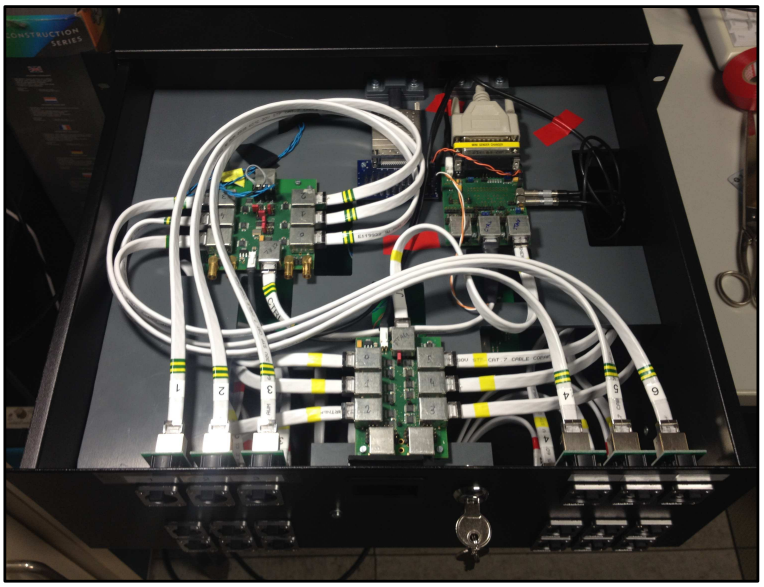

Figure 2.10: Photo of the pre-cabled 19-inch rack drawer for MIMOSA-28 setup. In the front of the box, RJ45 feed-through connectors are fixed.

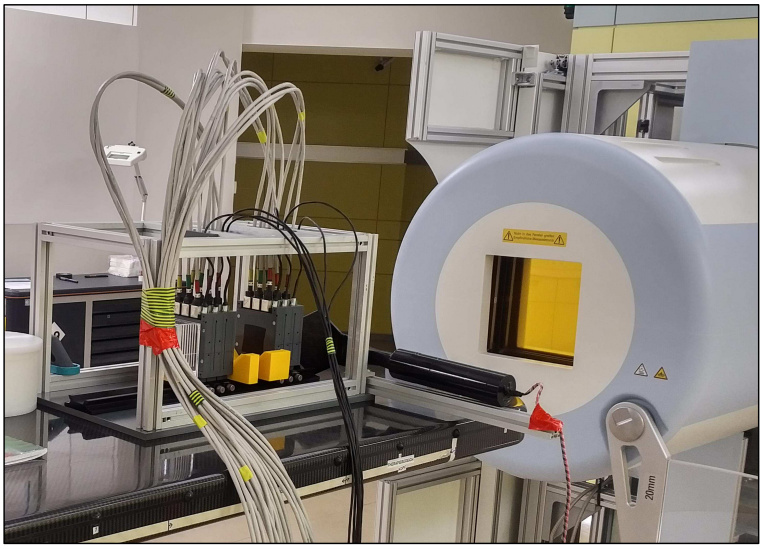

Figure 2.11: Photo of the MIMOSA-28 setup during an experiment performed at the Marburg Ion-beam Therapy Center, where six sensors are placed along an optical bench. All cables, connected to the sensor proximity boards, are clamped to a cage made from aluminum profiles.

Chapter 3

Materials & Methods

In this work, several experiments have been performed with the goal of providing high precision experimental data for ion-beam therapy. Due to the high spatial resolution of Mimosa-28, the sensors have been used in different experimental conditions. The first part of this chapter describes the software package of this pixel sensor, the alignment procedure that was developed during this PhD thesis as well as a description of the response of Mimosa-28 sensor to heavy charged particles. These steps are necessary to obtain high precision measurements. The beam profiles of therapeutic beams and the fluence perturbation due to fiducial markers were measured with high resolution. In this chapter, the experimental setups used for these measurements are described.

3.1 Software package for Mimosa-28 sensors

The analysis of the data, obtained with the Mimosa-28 sensors, was performed using the object-oriented Qapivi software [8], written in C++. This code contains a reconstruction and a simulation part, based on the Root [133] and Geant4 [134] libraries.
In the frame of this work, the reconstruction package was modified to improve the efficiency and precision of the data analysis. This section explains the different steps followed of Qapivi, regarding the reconstruction and simulation parts.

3.1.1 Reconstruction

The reconstruction part of Qapivi aims to reconstruct the trajectories of charged particles passing through several sensors (also referred to as *planes*). The different steps, required for the data analysis of Mimosa-28, are detailed with the conversion of raw data to hit pixels, the clustering, the tracking and the vertexing.

3.1.1.1 From raw data to hit pixels

The binary file, generated from the DAQ system, is decoded following the logic described in section 2.2.1.3 and for each event, the fired pixels are moved to a memory container. The pixels that belong to this container are called *hits*, and the event number is equal to the frame number defined by the sensor readout. A hit is identified by its event number,

sensor ID (numbered from 1 up to the number of sensors placed during the experiment) and its position. The latter is defined as the line and column numbers that were fired, and are converted to (x, y) coordinates. The total number of containers depends on the number of sensors, and all fired pixels from one sensor belong to the same container.

3.1.1.2 From hits to clusters

A *cluster* is defined as a group of neighboring pixels that were fired from the same particle. For this reconstruction step, a clustering algorithm was implemented [135], based on the first neighbor search in an iterative way. With such purpose, all consecutive hits with a common edge are considered to be part of the same cluster. The procedure stops when no more neighboring pixels are found. The performance of this algorithm was tested by means of a random cluster generator, and the efficiency was found to be better than 99%. As for the hits, a cluster is identified by its event number, sensor ID and its position. The latter is defined as the center of mass from all pixels composing the cluster, and is considered as valid when the number of pixels that belong to this cluster is bigger than a certain value set by the user. This condition is used for optimizing the time of the next step by suppressing the clusters generated by noise.

3.1.1.3 From clusters to tracks

A *track* is described by a regression line matching several clusters in different planes. The track resolution is calculated by the residuals [135], defined as the difference between the cluster and the track positions at a given plane. The tracking algorithm is based on the one implemented for the FIRST experiment [135], and was improved in the context of this work. The different steps followed during the tracking are listed below:

- All combinations of the valid clusters from the first and the last planes are considered and a straight line is computed for each combination, which defines a preliminary track.
- For every intermediate plane, the closest cluster to the computed line is added to the track candidate, and the track parameters of the regression line are updated after fitting all found clusters.
- A track is considered valid after being evaluated by a set of constraints:
  - Three or more clusters belong to the track, and only one missing cluster is allowed. The latter point is considered since a sensor can be less sensitive than the others. This can be due to the fact that the deposited energy inside the sensor was not enough to create a signal above the threshold, or that some pixels did not produce any signal (dead pixels).
  - The track residuals, evaluated for each plane, are smaller than certain thresholds. The latter are estimated for every plane with a weight calculation based on multiple Coulomb scattering, approximated by the Highland formula (equation 1.4). The weight is defined as $w_i = 1/\tilde{\sigma}_{x,i}$ for sensor i, where they are estimated from a pencil beam passing through different materials. The calculation details of $\tilde{\sigma}_{x,i}$ can be found in section 3.4.2.1.

    * The deviation of the cluster size from all found clusters is smaller than a certain cut.

- Non-valid tracks are re-evaluated through the previous step, where the residual constraint is set to a less strict condition. This step is repeated via several iterations until reaching a fixed limit defined by the user.
- In the case valid clusters are still available, all steps are re-performed with a decrement of the last plane definition in the first step.
- The algorithm stops when no valid clusters or no valid track candidates are available.

3.1.1.4 From tracks to vertices

The vertexing step is performed in case a target is placed in front or in-between the tracker system. A *vertex* is defined as an interaction point between two or more tracks. Vertices are determined as the mean coordinates, where the distance between the two extrapolated tracks from the front and from the back, is minimum. A valid vertex is defined when this distance is smaller than a certain value set by the user.

3.1.2 Monte Carlo simulation

The goal of the Monte Carlo simulations for this work is to provide comparable data sets to the ones recorded from the Mimosa-28 sensors, and to test the performance of the reconstruction code.
Geant4 [134] is an object-oriented simulation toolkit, developed by CERN. This Monte Carlo transport code can be applied to high energy, nuclear and accelerator physics, but also to medical and space radiation applications. Geant4 is a modular and flexible code, whose implementation is transparent and open to the user. The main tools used for the simulations presented in this work are listed below:

- The *geometry* defines the volumes and materials as well as their positions for the simulated geometrical structure.
- The *physics list* considers the interaction processes used during the simulation run.
- The *particle gun* establishes the particle species and energies that will be transported through the geometry during the simulation run.
- The *run* decides of the actions at the beginning and at the end of the simulation.
- The *event* considers the actions at the beginning and at the end of every primary event generated by the particle generator.
- The *stepping* determines the actions performed at the beginning and at the end of each step that correlates to one interaction along the track of a particle.

The Mimosa-28 sensor geometry was implemented in Geant4 by means of multiple superimposed volumes, representing the different sensor layers. They were designed following the dimensions of the Mimosa-28 sensor, as described in section 2.2, and the sensitive volume was defined as the epitaxial layer of the sensor.

The particle gun was set to different ion species and energies, as the ones used for particle therapy. The primary particles were generated following a Gaussian distribution, and the initial parameters such as beam position, width and divergence could be set to values comparable to the ones used in different experiments.
The physics list used for the simulations was the binary cascade light ion model (BIC) [136] in combination with the electromagnetic processes option 3 (EMY option) [137], which are recommended for particle therapy applications.
The runs consisted of a certain number of particles that were generated at a defined position, and transported along the constructed geometry. The particles interacting with the sensitive volume, defined as the epitaxial layer of the sensor, are considered as candidates for the simulation output. To decide whether an event is kept or not, the deposited energy of the particle inside the sensitive volume is compared to an energy cut, which reproduces the threshold values set during the experiments. In case the energy deposition is higher than this threshold, the particle parameters are recorded, and used as input for the reconstruction code. The simulation output is based on the response of the detector, detailed in section 3.3, and is generated by means of a digitizer included in the QAPIVI framework.

3.2 Alignment procedure for CMOS sensors

A tracker composed of several MIMOSA-28 sensors can reach a spatial track resolution better than 10 µm [135], due to the high intrinsic resolution of the sensor. Nevertheless, this is only possible when an alignment procedure is performed beforehand. This procedure, implemented in the reconstruction code, aims to correct the mechanical misalignment of the sensors by software. The alignment is needed to determine the translational and rotational shifts (referred to as *alignment parameters*) of the sensors relative to each other. During an experiment, a so-called alignment run needs to be performed, where a particle beam passes through the sensors placed along the z-axis. For this run, no target is placed in front or in-between the sensors and no magnetic field is applied. The alignment parameters can then be determined, using the positions of the primary particles passing almost straight through the tracker.
The different methods developed for the alignment of several sensors are generally based on iterative procedures that sequentially process a given amount of tracks [138, 139]. For this, the particle trajectories are fitted by a linear regression, where the translational and rotational shifts of the sensors are optimized. This iterative concept has the disadvantage to be significantly time consuming. For that reason, e.g., Blobel introduced a so-called matrix method for aligning the sensors, in which the alignment parameters are optimized in one step through matrix operations [140, 138]. The latter algorithm is able to optimize a large number of parameters in a simultaneous linear least square fit for a certain number of tracks, and uses the simultaneous optimization approach for the local and global parameters. The track parameters are defined by the local parameters (e.g., slope and intersection for a straight line), while the alignment parameters are defined by the global parameters (correction of detector positioning common for all tracks).
In the case of MIMOSA-28, the alignment procedure originally implemented in QAPIVI, is based on an iterative procedure that calculates the global parameters after fitting a given amount of tracks. The algorithm repeats this operation until the difference of the alignment parameters between two consecutive iterations is smaller than a given requirement.

This procedure needs many iterations and in some cases, the algorithm does not converge. For this procedure, a pre-alignment of the sensors is required in order that the tracks can be reconstructed by the tracking algorithm.
To improve the accuracy and efficiency of the alignment, a new procedure was developed in the frame of this PhD thesis, and implemented in Qapivi. The procedure follows the general concept of Millepede [140], developed by Blobel et al., with a global optimization. However, the presented procedure can be implemented easier than the one from Blobel that requires a linearization around the initial local and global alignment parameters. In addition, the developed procedure is based on the cluster positions rather than on the track positions, and is explicitly adapted to the situation of a tracker system composed of a set of parallel Mimosa-28 sensors. Since the primary particles undergo multiple scattering in the sensors and in the air gaps between them, the alignment procedure described in this work includes an event rejection loop, based on simple scattering calculations, which improves the quality of the results.
The following section reports the new alignment procedure with a full description of the alignment algorithm, the refinement of the procedure and its implementation in the reconstruction code. The experimental setup and the Monte Carlo simulations, performed to test the performance of the procedure, are also detailed. The alignment procedure and its performance are published in [141].

3.2.1 Alignment algorithm

The alignment algorithm presented in this section is based on the optimization of a global χ^2 function. The local parameters are not explicitly computed, but are implicitly dependent on the global parameters that are calculated within the χ^2 function. The local parameters are defined by the linear regression parameters, and the global parameters are represented by the alignment parameters. This method is very efficient and can process a high number of events. An *event* is defined as the measured positions from a single particle traversing all sensors, while the linear fit of these positions is referred to as a *track*. The alignment parameters are calculated after solving a matrix-equation, whose size is independent from the number of events processed. The χ^2 function, depending on the alignment parameters, and the resulting matrix are derived, and stepwise described in this section.

3.2.1.1 Concept

In an optimal scenario, the sensors would be placed without any misalignment along the beam axis during an experiment, and the tracks could be reconstructed without performing any alignment procedure Figure 3.1 (left panel). In a realistic case, the sensors are placed with initial mechanical misalignments that need to be corrected in order to obtain a reliable data analysis. Figure 3.1 (middle panel) and (right panel) illustrate a reconstructed track before and after the alignment procedure, respectively.

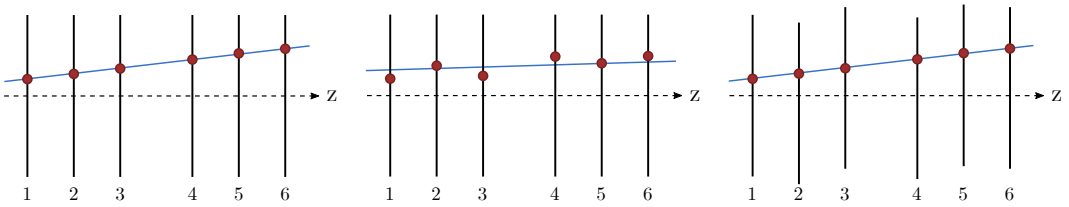

Figure 3.1: The left panel illustrates a reconstructed track with six sensors placed along the beam axis for an optimal scenario. The middle and right panels sketch a reconstructed track before and after the alignment procedure with six sensors placed along the beam axis. The particle positions are defined by the red circles, while the track is represented by the blue line.

The free alignment parameters, defined in this work, are two translations dx and dy, and one rotation $d\phi$ around the z-axis (parallel to the beam axis) per sensor. For a precise mechanical setup, the sensors can be positioned with a typical accuracy < 0.5 mm lateral to the beam axis, and < 30 mrad around the x-axis and y-axis. The impact of the latter rotations can be neglected since the geometrical correction factor is smaller than $1 - \cos(0.03)$, and is not relevant for the MIMOSA-28 dimensions of 20×20 mm^2. It should also be noted that the influence of the longitudinal parameters is very small compared to the transversal ones. For a RMS of 10 mrad for the linear track slopes, the sensitivity of the longitudinal alignment parameters is a factor 100 (1/RMS) smaller compared to the transversal parameters.
Considering the two translations dx_i, dy_i and the rotation $d\phi_i$, the corrected coordinates (X_{ij},Y_{ij}) relative to the original coordinates (x_{ij},y_{ij}) of sensor i for a track j are calculated as follows:

$$\begin{pmatrix} X_{ij} \\ Y_{ij} \end{pmatrix} = \begin{pmatrix} \cos(d\phi_i) & \sin(d\phi_i) \\ -\sin(d\phi_i) & \cos(d\phi_i) \end{pmatrix} \begin{pmatrix} x_{ij} \\ y_{ij} \end{pmatrix} + \begin{pmatrix} dx_i \\ dy_i \end{pmatrix} . \tag{3.1}$$

Since the rotation $d\phi_i$ around the z-axis is small ($d\phi_i \ll 1$), equation 3.1 can be simplified:

$$\begin{pmatrix} X_{ij} \\ Y_{ij} \end{pmatrix} = \begin{pmatrix} 1 & d\phi_i \\ -d\phi_i & 1 \end{pmatrix} \begin{pmatrix} x_{ij} \\ y_{ij} \end{pmatrix} + \begin{pmatrix} dx_i \\ dy_i \end{pmatrix} . \tag{3.2}$$

3.2.1.2 Degrees of freedom

A global coordinate system needs to be established for the tracker, which is achieved by fixing several alignment parameters. For this, two translational parameters in x and two in y are restricted to constrain the translations in x and y and the rotations around the x-axis and y-axis. Since the z-shift is neglected, only one rotational parameter around the z-axis needs to be fixed. In this work, the first and the last planes are defined as references, such as $dx_1 = 0$, $dy_1 = 0$, $d\phi_1 = 0$, $dx_n = 0$ and $dy_n = 0$, where n is the number of planes.

3.2.1.3 Linear regression analysis for a single track

A track is defined as the linear fit, also called linear regression, of the measured positions from a particle passing through the sensors. The corresponding S is the square sum of the differences between the measured positions and the track positions in the sensors, defined as:

$$S(a,b) = \sum_{i=1}^{n} w_i^2 [(a + bz_i) - p_i]^2 \,, \tag{3.3}$$

where p_i is the coordinate (either x_i or y_i) of the measured particle for sensor i at position z_i, and w_i represents the weight given by the expected uncertainty of the measured event. In order to define the weight, the spatial distribution σ_i, induced by multiple Coulomb scattering at sensor i, is calculated as a function of the angular scattering distribution σ_α from the sensors and the air gaps, as given in equation 30 by Gottschalk et al. (1993) [142]. The applied weight, such as $w_i = 1/\tilde{\sigma}_{x,i}$, is the same for all events, and the same in x and y since MIMOSA-28 is composed of square pixels. The regression coefficients a and b of the linear fit are the parameters to be defined. In order to have the best possible fit, the least squares method is used to estimate a and b, which minimizes S leading to χ^2_S [143].
The optimized regression coefficients a and b become the least squares estimators $\hat{a}$ and $\hat{b}$, and are calculated as follows:

$$\begin{pmatrix} \hat{a} \\ \hat{b} \end{pmatrix} = A^{-1} B \begin{pmatrix} p_1 \\ \vdots \\ p_n \end{pmatrix} \,, \tag{3.4}$$

where A is a 2×2 matrix and B is a 2×n matrix:

$$\begin{aligned} A &= \begin{pmatrix} \sum_{i=1}^{n} w_i^2 & \sum_{i=1}^{n} w_i^2 z_i \\ \sum_{i=1}^{n} w_i^2 z_i & \sum_{i=1}^{n} w_i^2 z_i^2 \end{pmatrix} \,, \\ B &= \begin{pmatrix} w_1^2 & \cdots & w_n^2 \\ w_1^2 z_1 & \cdots & w_n^2 z_n \end{pmatrix} \,. \end{aligned} \tag{3.5}$$

After replacing the regression coefficients by the least squares estimators, the χ^2_S function can be written as:

$$\chi^2_S = \sum_{i=1}^{n} \left[w_i \left(\begin{pmatrix} 1 & z_i \end{pmatrix} \begin{pmatrix} \hat{a} \\ \hat{b} \end{pmatrix} - p_i \right) \right]^2 \,. \tag{3.6}$$

By combining equations (3.4) and (3.6), the χ^2_S becomes:

$$\chi^2_S = \left(\left[\overrightarrow{w} \odot (KL - I_n \right] \overrightarrow{p} \right)^2 , \tag{3.7}$$

where I_n is the $n \times n$ identity matrix, and L is the product $L = A^{-1}B$. The symbol "$\odot$" defines here the element-wise product. The n-vectors $\overrightarrow{w}$ and $\overrightarrow{p}$, and the K matrix of dimension $n \times 2$, are defined as the following:

$$\overrightarrow{w} = \begin{pmatrix} w_1 \\ \vdots \\ w_n \end{pmatrix} , \qquad \overrightarrow{p} = \begin{pmatrix} p_1 \\ \vdots \\ p_n \end{pmatrix} , \qquad K = \begin{pmatrix} 1 & z_1 \\ \vdots & \vdots \\ 1 & z_n \end{pmatrix} . \tag{3.8}$$

For readability simplification, the $n \times n$ matrix Q is introduced as $Q = \overrightarrow{w} \odot (KL - I_n)$, and is constant for a given setup with certain positions z_i and weights w_i. Equation 3.7 is then written in the following form:

$$\chi^2_S = \left(Q \overrightarrow{p} \right)^2 . \tag{3.9}$$

3.2.1.4 Definition of the χ^2 for the global alignment parameters optimization

The alignment algorithm is based on the minimization of a global χ^2 function, which combines the linear regression analysis for all tracks. The variables X_i and Y_i are the corrected coordinates, explicitly depending on the searched alignment parameters dx_i, dy_i and $d\phi_i$ (see equation 3.2), common for all tracks. For a single track, $\chi^2_{S_X}$ and $\chi^2_{S_Y}$ define the optimal linear fit in x and y, respectively, and are written as follows:

$$\begin{cases} \chi^2_{S_X} = \sum_{i=1}^{n} w_i^2 [(\hat{a}_X + \hat{b}_X z_i) - X_i]^2 \\ \chi^2_{S_Y} = \sum_{i=1}^{n} w_i^2 [(\hat{a}_Y + \hat{b}_Y z_i) - Y_i]^2 \end{cases} , \tag{3.10}$$

where $\hat{a}_X$, $\hat{b}_X$, $\hat{a}_Y$ and $\hat{b}_Y$ are the least squares estimators for the regression line of the corrected positions X_i and Y_i. These parameters differ for each independent track and the global χ^2 function, containing the alignment parameters, is then the sum over all tracks k (for sensor i and track j):

$$\chi^2(dx_i, dy_i, d\phi_i) = \sum_{j=1}^{k} \left[\sum_{i=1}^{n} w_i^2 [(\hat{a}_{X_j} + \hat{b}_{X_j} z_i) - X_{ij}]^2 + \sum_{i=1}^{n} w_i^2 [(\hat{a}_{Y_j} + \hat{b}_{Y_j} z_i) - Y_{ij}]^2 \right] . \tag{3.11}$$

This χ^2 defines the goodness of the linear fit of all tracks, and yields a minimum when the searched alignment parameters are optimum. The least squares estimators $\hat{a}_X$, $\hat{b}_X$, $\hat{a}_Y$ and $\hat{b}_Y$ implicitly depend on the searched alignment parameters (equation 3.4).

3.2.1.5 Calculation of the alignment parameters

The alignment parameters can be explicitly calculated after converting the χ^2 in equation 3.11 to a single matrix equation that can be solved after a matrix inversion. From equation 3.2, the coordinates X_i and Y_i of the corrected positions for a single event can be calculated as:

$$\begin{pmatrix} X_1 \\ \vdots \\ X_n \end{pmatrix} = \begin{pmatrix} x_1 + d\phi_1 y_1 + dx_1 \\ \vdots \\ x_n + d\phi_n y_n + dx_n \end{pmatrix} , \qquad \begin{pmatrix} Y_1 \\ \vdots \\ Y_n \end{pmatrix} = \begin{pmatrix} y_1 - d\phi_1 x_1 + dy_1 \\ \vdots \\ y_n - d\phi_n x_n + dy_n \end{pmatrix} . \tag{3.12}$$

After defining the vectors $\overrightarrow{X}$, $\overrightarrow{Y}$, $\overrightarrow{x}$ and $\overrightarrow{y}$, equation 3.12 can be re-written as:

$$\begin{aligned} \overrightarrow{X} &= \overrightarrow{x} + P_X \overrightarrow{m} , \\ \overrightarrow{Y} &= \overrightarrow{y} + P_Y \overrightarrow{m} , \end{aligned} \tag{3.13}$$

where P_X and P_Y are $n \times 3n$ matrices defined as:

$$P_X = \begin{pmatrix} 1 & \cdots & 0 & 0 & \cdots & 0 & y_1 & \cdots & 0 \\ \vdots & \ddots & \vdots & \vdots & \ddots & \vdots & \vdots & \ddots & \vdots \\ 0 & \cdots & 1 & 0 & \cdots & 0 & 0 & \cdots & y_n \end{pmatrix} , \qquad P_Y = \begin{pmatrix} 0 & \cdots & 0 & 1 & \cdots & 0 & -x_1 & \cdots & 0 \\ \vdots & \ddots & \vdots & \vdots & \ddots & \vdots & \vdots & \ddots & \vdots \\ 0 & \cdots & 0 & 0 & \cdots & 1 & 0 & \cdots & -x_n \end{pmatrix} . \tag{3.14}$$

The searched $3n$-vector $\overrightarrow{m}$ contains the alignment parameters common to all events:

$$\overrightarrow{m} = (dx_1, \quad \cdots , \quad dx_n, \quad dy_1, \quad \cdots , \quad dy_n, \quad d\phi_1, \quad \cdots , \quad d\phi_n)^{\mathrm{T}} . \tag{3.15}$$

The combination of equations 3.4 and 3.13 results to the minima $\chi^2_{S_X}$ and $\chi^2_{S_Y}$:

$$\begin{aligned} \chi^2_{S_X} &= \left(Q\,\overrightarrow{x} + QP_X\overrightarrow{m} \right)^2 , \\ \chi^2_{S_Y} &= \left(Q\,\overrightarrow{y} + QP_Y\overrightarrow{m} \right)^2 . \end{aligned} \tag{3.16}$$

By introducing the $n{\times}3n$ matrices C^X and C^Y, and the n-vectors $\overrightarrow{d^X}$ and $\overrightarrow{d^Y}$ as:

$$C^X = QP_X\ , \qquad C^Y = QP_Y\ , \qquad \overrightarrow{d^X} = Q\,\overrightarrow{x}\ , \qquad \overrightarrow{d^Y} = Q\,\overrightarrow{y}\ . \tag{3.17}$$

The χ^2 in equation 3.11 can now be re-written as a quadratic matrix equation:

$$\chi^2(\overrightarrow{m}) = \sum_{j=1}^{k} \left[(C_j^X\overrightarrow{m} + \overrightarrow{d_j^X})^2 + (C_j^Y\overrightarrow{m} + \overrightarrow{d_j^Y})^2 \right] , \tag{3.18}$$

The gradient of the χ^2 with respect to $\overrightarrow{m}$ is then a term linear in $\overrightarrow{m}$:

$$\overrightarrow{\nabla}\chi^2(\overrightarrow{m}) = C_m\overrightarrow{m} + \overrightarrow{d}_m\ , \tag{3.19}$$

where the $3n{\times}3n$ matrix C_m and the $3n$-vector $\overrightarrow{d}_m$ are built by summing all events:

$$\begin{aligned} C_m &= \sum_{j=1}^{k} \left(({C_j^X}^{\mathrm{T}} C_j^X) + ({C_j^X}^{\mathrm{T}} C_j^X)^{\mathrm{T}} + ({C_j^Y}^{\mathrm{T}} C_j^Y) + ({C_j^Y}^{\mathrm{T}} C_j^Y)^{\mathrm{T}} \right) , \\ \overrightarrow{d}_m &= \sum_{j=1}^{k} \left(2\,(\overrightarrow{d_j^X}^{\mathrm{T}} C_j^X + \overrightarrow{d_j^Y}^{\mathrm{T}} C_j^Y)^{\mathrm{T}} \right) . \end{aligned} \tag{3.20}$$

As mentioned in section 3.2.1.2, five global parameters have to be constrained in order to get a defined geometrical situation. Therefore, the alignment parameters of the first plane, and the transversal parameters of the last plane are set to 0. These restrictions are best suited for the coarse mechanical alignment since the first and the last sensors can be easier accessed than the intermediate ones during an experiment.
After constraining the tracker in the global coordinate system, the final gradient of the χ^2 can be expressed as the following:

$$\overrightarrow{\nabla}\chi^2(\overrightarrow{m}^f) = C_m^f\overrightarrow{m}^f + \overrightarrow{d}^f_m\ , \tag{3.21}$$

where the $(3n{-}5){\times}(3n{-}5)$ matrix C_m^f and the $(3n{-}5)$-vector $\overrightarrow{d}^f_m$ are obtained by canceling the five degrees of freedom (i.e., dx_1, dy_1, $d\phi_1$, dx_n and dy_n), and the corresponding columns, rows and elements in C_m and $\overrightarrow{d}_m$. The vector $\overrightarrow{m}^f$ contains the searched alignment parameters.

In order to obtain a minimum χ^2, its gradient with respect to $\overrightarrow{m}^f$ is set to 0. By inverting the matrix C_m^f, the searched alignment parameters are then calculated as follows:

$$\overrightarrow{m}_{opt}^f = -{C_m^f}^{-1} \overrightarrow{d}_m^f \,. \tag{3.22}$$

It should be noted that without the mentioned cancellation of the five degrees of freedom, the matrix C_m^f would be singular and could not be inverted. The matrix ${C_m^f}^{-1}$ is the so-called covariance matrix. The alignment parameters in $\overrightarrow{m}_{opt}^f$ define now an optimal correction for all events, with a minimum weighted (by the uncertainties) mean (quadratic) deviation between the corrected measured positions X_{ij} and Y_{ij}, and their corresponding individual regression lines. A package of script examples for the alignment algorithm is presented in the supplementary material at *http://dx.doi.org/10.17632/9g5r3ypcb6.2*.

3.2.2 Refinement of the algorithm

The described algorithm is able to determine the alignment parameters in one step, after accumulation of a given number of events. The tracking is not explicitly performed, which allows the procedure to be independent of the initial misalignments. The basic assumption exploited by the algorithm is that the particles traverse the sensors following almost a straight line. Therefore, strongly scattered events degrade the quality of the results. In order to avoid a significant influence on the alignment parameters results due to scattered particles, two further calculation steps are performed with the same algorithm. In these steps, the alignment parameters from the previous solution are applied, and the strongly scattered events (e.g., due to nuclear interaction) are rejected. Therefore, for each particle, the measured angular deflection from one sensor i to the next one is compared to the theoretical width σ_α^i of the angular distribution induced by the multiple Coulomb scattering at sensor i. The σ_α value is calculated by the Highland approximation [53, 54], which considers the multiple Coulomb scattering as a Gaussian process and provides an estimate for its standard deviation. In this work, the rejection thresholds were set to $20\sigma_\alpha^i$ (pre-filtering) and $4\sigma_\alpha^i$ for the second and third calculation steps, respectively. In each step, 10–40% of the events are eliminated by this filter procedure, and the calculated alignment parameters become more accurate. These additional steps are especially necessary for the accuracy of the rotation parameter, which is more sensitive to the scattering. Table 3.1 quantifies the accumulated angular distribution from a set of six MIMOSA-28 sensors, for 150 and 300 MeV/u protons, ^{4}He and ^{12}C ions.

Table 3.1: Accumulated angular distribution due to multiple Coulomb scattering for a set of six MIMOSA-28 sensors, for 150 and 300 MeV/u protons, ^{4}He and ^{12}C ions.

	Protons		Helium ions		Carbon ions	
Energy (MeV/u)	150	300	150	300	150	300
σ_α (mrad)	2.1	1.1	1.1	0.6	1.0	0.5

3.2.3 Evaluation of the procedure

The alignment procedure, described above, was implemented in the software QAPIVI. In the frame of this work, a new class was developed, and included in the reconstruction code. In this section, the Monte Carlo simulations and the experimental setups used for testing the performance of the alignment procedure are described.

3.2.3.1 Experimental setup

Dedicated alignment measurements were performed in the experimental room at the Proton Therapy Center in Trento [144] and at the Ion-beam Therapy Center in Heidelberg (HIT) [145]. An experimental setup composed of six MIMOSA-28 sensors was placed at an angle of 0° with respect to the beam axis. The sensors were mechanically aligned to the room laser by means of reference marks drawn on the sensor holders. The alignment runs were performed without target, without magnetic field and at low intensity (< 5 kHz) to avoid pile-up in the sensors. The beam particles used were protons and helium ions, within the therapeutic energy range from 80 to 220 MeV/u. The energies and FWHM, of the beam at the room isocenter, are listed in Table 3.2 for both experiments. Two different setup geometries were tested: one with a distance of 35 cm between the first and the last sensor (Figure 3.2 (top panel)), and one with a distance of 8.8 cm (Figure 3.2 (bottom panel)). For both experiments, the detector thresholds were set to six times the noise level (see section 2.2.1.2).

Table 3.2: Energy and FWHM of the proton beams from the Proton Therapy Center in Trento and helium ion beams from the HIT facility.

	Protons					
Energy (MeV)	90.8	125.3	148.5	164.4	188.8	219.8
FWHM (mm)	7.8	6.2	5.4	4.9	4.1	3.5
	Helium ions					
Energy (MeV/u)	80.64		130.25		220.51	
FWHM (mm)	11.8		7.6		4.9	

The performance of the alignment procedure for the experimental data are evaluated after computing the total residuals, determined from all tracks. The track resolution is then defined by the width of the residual distributions in x and y. The performance of the procedure implemented in this work (referred to as *ClusAlign*) was compared to the ones of the algorithm originally implemented in QAPIVI (referred to as *TrackAlign*), and to the state-of-the art algorithm MILLEPEDE II.

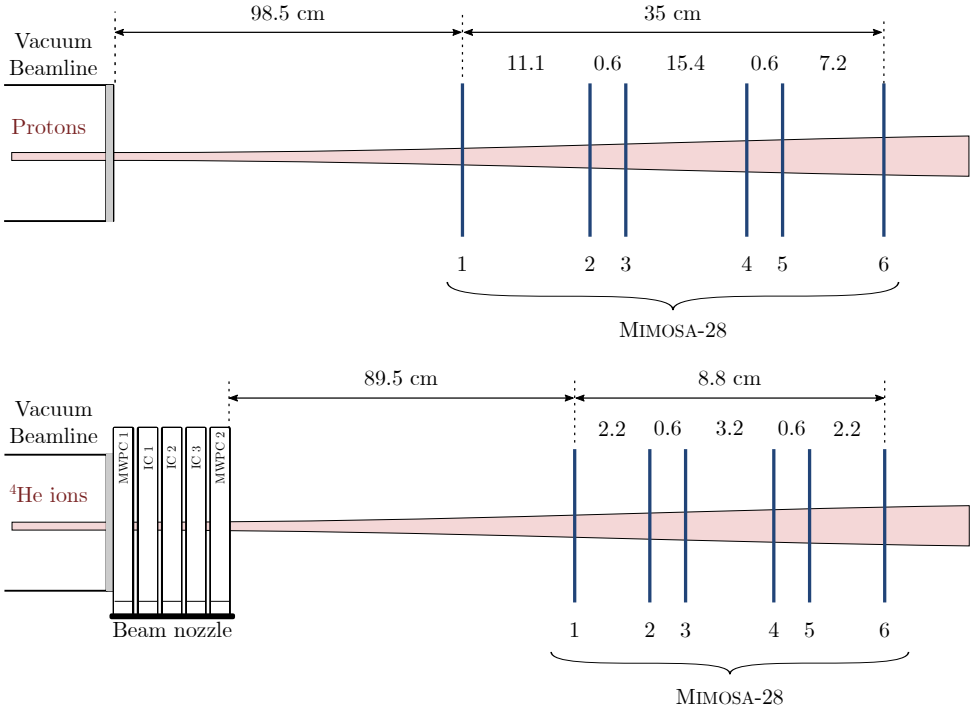

Figure 3.2: Experimental setups dedicated to test the performance of the alignment procedure. In both cases, the setup consisted of six MIMOSA-28 sensors placed along the beam axis. The top panel illustrates the setup with a spread geometry tested with protons at the Proton Therapy Center in Trento. The bottom panel sketches the setup with a compact geometry tested with helium ions at the HIT facility.

3.2.3.2 Data simulation

The Monte Carlo simulations for testing the alignment procedure were generated with the simulation package described in section 3.1.2, based on GEANT4 version 10.04. The ion optics of the beam (FWHM and beam divergence) were adapted to reproduce comparable beam characteristics to the ones used for therapy, listed in Table 3.2. Six sensors were placed along the beam axis, and noisy pixels were randomly created as a function of the signal to noise ratio. The threshold was set to six times the noise level in order to reproduce the experimental data.
Different ion beam configurations, listed in Table 3.3, were simulated for both setup geometries. The values of the beam divergence were defined as the angular distribution in front of the vacuum window. The position of the sensors along the beam axis are listed in Table 3.4 for a compact geometry (referred to as *Geo1*), and for a spread geometry (referred to as *Geo2*). For both geometries, the start position for the simulations was set to 50 cm upstream of the first sensor.

Table 3.3: Particle, energy and ion optical beam parameters (FWHM and divergence) at the vacuum window, used for the Monte Carlo simulations.

	Protons		Helium ions		Carbon ions	
Energy (MeV/u)	150.0	300.0	150.0	300.0	150.0	300.0
FWHM (mm)	7.1	7.1	7.1	5.9	5.9	4.7
Divergence (mrad)	5.0	3.0	3.0	2.5	2.5	2.0

Table 3.4: Sensor positions along the beam axis for a compact geometry (Geo1), and a spread geometry (Geo2).

	Sensor	1	2	3	4	5	6
Position (cm)	Geo1	−1.25	−0.75	−0.25	0.25	0.75	1.25
	Geo2	−12.50	−7.50	−2.50	2.50	7.50	12.50

To test the alignment procedure, some arbitrary set-values for the misalignments dx, dy and $d\phi$ were defined for each sensor. As explained in section 3.2.1.1, the translations and the rotation of the first sensor (primary reference plane) and the translations of the last sensor (secondary reference plane) were set to 0. Since the rotation is more sensitive and has a lower impact than the two translations, a first study only involving the translations dx and dy ($d\phi$ set to 0) was performed. Two scenarios were simulated: one with small misalignment values, slightly bigger than the intrinsic resolution of the detector (referred to as *Mis1*), and one with larger misalignment values in the order of the mechanical positioning uncertainty during an experiment (referred to as *Mis2*) (∼1 mm) (Table 3.5).
In the presented work, the deviations δ are defined as the absolute value of the difference between the calculated alignment parameters and the ones set for the Monte Carlo simulations (referred to as *set-misalignments*) such as $\delta = |d_{calc} - d_{set}|$.

Table 3.5: Two misalignment scenarios for a set of six sensors. Mis1 describes a scenario with small misalignment values, whereas Mis2 contains larger misalignment values. Rotational misalignments are set to zero in both cases.

	Sensor	1	2	3	4	5	6
Mis1	dx (µm)	0.0	−5.0	3.0	−15.0	6.0	0.0
	dy (µm)	0.0	5.0	−4.0	−8.0	12.0	0.0
Mis2	dx (µm)	0.0	−753.0	850.0	−978.0	925.0	0.0
	dy (µm)	0.0	928.0	−789.0	842.0	−891.0	0.0

The accuracy of the alignment algorithm as a function of the number of events ranging, from 2500 to 650000 events, was quantified with the misalignment scenarios listed in Table 3.6 (referred to as *Mis3*). The rotational misalignments are now set to non-zero values. Since the rotation matrix in equation (3.2) was approximated for small $d\phi$ values, the alignment procedure results for larger rotational misalignments (up to 10°) were also studied.

Table 3.6: Translational and rotational misalignment scenario Mis3, for a set of six sensors.

	Sensor	1	2	3	4	5	6
Mis3	dx (µm)	0.0	438.0	−349.0	−913.0	166.0	0.0
	dy (µm)	0.0	−225.0	574.0	−682.0	751.0	0.0
	$d\phi$ (°)	0.00	0.823	−0.150	−1.730	−0.340	1.228

All data sets were processed with an Intel Core i3-2100 CPU @ 3.10 GHz (2 physical cores and 4 threads).

3.3 Response of Mimosa-28

The response of Mimosa-28 is defined as the cluster size, representing the group of fired pixels from the ionizations of a charged particle passing through the sensor. The cluster size is thus explained by the number of pixels per cluster. This depends on the deposited energy, and the track structure of a particle passing through the epitaxial layer of the Mimosa-28 sensor.

3.3.1 Experimental study

Different experimental setup configurations were used for the study of the detector response, where several Mimosa-28 sensors were placed along the z-axis. In some cases, the setup was mounted without any target in front or in-between, and in other cases, additional materials, e.g., water, were placed along the beam axis.
A first study was carried out to compare the cluster size of the first generation (referred to as *Generation 1*) and the second generation (referred to as *Generation 2*) of Mimosa-28 sensors for 80.64, 130.25 and 220.51 MeV/u helium ion beams. The experimental setup described in Figure 3.2 (bottom panel) was composed of three sensors of Generation 1 (sensors 4–6), and three sensors of Generation 2 (sensors 1–3).
A second study investigated the cluster size for different ion species and beam energies. In Table 3.7, the particle beams and their energies as well as the accelerator facility where the measurements were conducted are listed.
In a third study, the cluster size was studied for an experimental setup where a water target was placed in-between two sets of three sensors. In this case, the experimental setup depicted in Figure 3.4 was used, where the target was replaced by a water phantom of 4 cm thickness, with an area larger than the beam FWHM. This study aimed to evaluate the

cluster size as a function of the different produced fragments from a 287.50 MeV/u carbon ion beam impinging on the water phantom.

Table 3.7: Particle species and beam energies used for the cluster size study of MIMOSA-28 sensor. The accelerator facilities where these measurements were conducted are also indicated.

Particle	Energy (MeV/u)	Facility
$^{1}H^{1+}$ ions	150.14	MIT[a]
$^{4}He^{2+}$ ions	80.64	HIT[b]
	130.25	HIT[b]
	220.51	HIT[b]
$^{12}C^{6+}$ ions	11.4	GSI[c]
	180	GSI[c]
	278.84	MIT[a]
	287.50	MIT[a]
	294.97	MIT[a]
	310.64	MIT[a]
$^{40}Ar^{18+}$ ions	225	GSI[c]
$^{56}Fe^{25+}$ ions	1000	GSI[c]

[a]Ion-beam Therapy Center in Marburg (Germany)
[b]Ion-beam Therapy Center in Heidelberg (Germany)
[c]Helmholtzzentrum für Schwerionenforschung GmbH in Darmstadt (Germany)

3.3.2 Cluster size analysis

The analysis of the detector response for MIMOSA-28 sensor was performed by using the clustering and tracking steps of the software QAPIVI. For this analysis, it is important to select the clusters produced by the primary particles. In order to do this, the tracks were reconstructed to reduce the noise, and eliminate the clusters that are not created from the primary particles. The cluster size is defined in this work as the maximum value from the cluster size distribution of one sensor. The energy losses were calculated with the software LISE++ [50] for 14 µm silicon thickness as the epitaxial layer of MIMOSA-28. The energy values in Table 3.7 are the ones of the primary particles before crossing the vacuum window. In case that some material layers were placed in front of the tracker, such as the beam nozzle or a water phantom, the primary energy of the particle was re-calculated to compensate the energy losses inside these materials.
The uncertainty for the cluster size was determined from the measured distribution, which is defined as the superposition of several Landau functions from the response of the fired pixels. The quartile at 15% of the distribution determines the lower limit, while the quartile

at 85% determines the upper one. The uncertainty on the deposited energy inside the epitaxial layer of the MIMOSA-28 sensor was quantified from the different energy losses in the material layers placed in front of the detector. The total uncertainty was then computed from the material thickness error, which is the main factor responsible for the energy loss variations.
The spatial distributions of the energy loss, detailed in section 1.4.1, for similar ion beams as the ones presented in Table 3.7, were computed with Monte Carlo simulations. With this purpose, the software TRAX [67] was used, which is a transport code at the nanoscopic level. With this code, the produced δ-electrons were tracked inside a volume material, defined as a 14 µm silicon layer. The deposited dose from the δ-electrons was calculated as a function of their distance from the primary track, and the radial dose distributions were computed.
To study the response of the MIMOSA-28 sensor as a function of the different produced fragments, when a thick target is placed in-between two sets of sensors, as explained above, the mean cluster size was computed. The mean cluster size is defined as the mean value of the different clusters that belong to a track, for all reconstructed tracks. This procedure was followed for the tracker placed in front (referred to as *bm–track*) and the tracker placed behind (referred to as *vt–track*) the target.

3.4 Lateral beam spread along the longitudinal axis

In this section, the lateral beam spread along the longitudinal axis is reported. The experimental setup, used for evaluating the beam settings, coincides with the one described in Figure 3.2 (top panel) of section 3.2.3.1. The beam profiles were measured at several positions along the longitudinal axis, and the transport of a pencil beam was computed to reproduce the measured data, after optimization of the initial ion optical parameters of the beam.

3.4.1 Beam profile analysis

The beam profiles were generated from the 2D cluster maps of the sensors at several positions along the beam axis. The profiles in x and y, at a certain position, were obtained with the projection of the cluster map in x and y, respectively. They were then fitted with a Gaussian function, whose mean and width were extracted. Regarding the lateral beam spread, calculated from the transport code, only the width parameter of the Gaussian function was used.

3.4.2 Particle transport

The transport code used to determine the lateral beam spread of a pencil beam was based on SCATTMAN [5, 10], and implemented in C++ including the ROOT libraries [133], in the frame of this work.

3.4.2.1 Ion optics and phase space distribution

The pencil beam model used relies on a non-parallel (focused) beam with a Gaussian distribution [146, 147]. The description of the ion optical phase space distribution of a pencil beam at a certain position z can be written as the following [148]:

$$f_z(x,\alpha) = C \exp\left[-\frac{1}{2}\left(\frac{(x-k\alpha)^2}{\sigma_x^2} + \frac{\alpha^2}{\sigma_\alpha^2}\right)\right], \tag{3.23}$$

where x is the lateral position of the beam, and α is the beam angle of the local angular distribution. The parameter k is the distance to the focus point z_{focus}, as $k = z - z_{focus}$, and is negative in the case that z is in front of the focus point. The values σ_x and σ_α are the widths of the spatial and angular distributions of the beam in the focal point, for a theoretically undisturbed beam ($k = 0$). Since the beam suffers elastic interactions when passing through different materials, the ion optic parameters σ_x, σ_α and k vary along the beam axis as a function of the multiple Coulomb scattering. After estimating the width of the angular distribution $d\sigma_\alpha$ of a pencil beam passing through a certain medium of distance dx by means of the Highland formula (equation 1.4) [53, 54], the unknown ion optic parameters at position i can be calculated as a function of the ion optic parameters at position $i-1$ by the following transport calculations:

$$\sigma_{x,i}^2 = \sigma_{x,i-1}^2 + \frac{k_{i-1}^2 \sigma_{\alpha,i-1}^2 d\sigma_{\alpha,i}^2}{\sigma_{\alpha,i-1}^2 + d\sigma_{\alpha,i}^2}\,, \tag{3.24}$$

$$\sigma_{\alpha,i}^2 = \sigma_{\alpha,i-1}^2 + d\sigma_{\alpha,i}^2\,, \tag{3.25}$$

$$k_i = k_{i-1} + \frac{\sigma_{\alpha,i-1}^2}{\sigma_{\alpha,i-1}^2 + d\sigma_{\alpha,i}^2} + d_i\,. \tag{3.26}$$

The width of the spatial distribution $\tilde{\sigma}_{x,i}$, which can be measured in practice at a certain position z_i along the beam axis, can be written as a function of the ion optic parameters:

$$\tilde{\sigma}_{x,i} = \sqrt{\sigma_{x,i}^2 + k_i^2 \sigma_{\alpha,i}^2}\,. \tag{3.27}$$

This procedure allows to calculate the envelope of a non-parallel (focused) beam, including the multiple Coulomb scattering, from a Gaussian approximation, for a sequence of targets and air gaps.

3.4.2.2 Fitting of the ion optical parameters for a focused beam

The formula described above were originally implemented in SCATTMAN. This transport code aims to calculate the width $\tilde{\sigma}_{x,i}$ of a pencil beam along the z-axis, based on the initial ion optic parameters σ_{x_0}, σ_{α_0} and k_0 defined for $z = 0$. To ensure that the calculated widths $\tilde{\sigma}_{x,i}$ fit the beam profile measurements along the z-axis, the initial ion optic parameters σ_{x_0}, σ_{α_0} and k_0 need to be optimized.

In this work, the formula were re-implemented in C++, and the calculation steps are based on ROOT functions. The implementation of the code improved, by adding an automatic optimization of the ion optic parameters, using a χ^2 minimization.

3.5 Online beam monitoring

In the frame of this work, a software was developed for online beam monitoring. The code was programmed in Python, and directly implemented in the DAQ system running Windows. The aim of this program is to give fast information regarding the position and the width of the beam to verify the beam profile during low intensity experiments. Only the first step of the reconstruction was implemented, where the raw data from the binary file are converted to hit pixels (detailed in section 3.1.1.1). The next reconstruction steps (e.g., clustering and tracking) would improve the precision of the beam profile information by reducing the noise. However, these steps are time consuming and can not be performed in the required time frame for online monitoring. Even though the hit pixels information is not as precise as the cluster one, beam profiles based on the reconstructed hits are suited to the needed precision for online beam monitoring.
The program was developed to read the data file at the same time the DAQ system is writing it. The raw data are then reconstructed to hit pixels, which are used to display a 2D hit map after a couple of seconds. Several parameters can be adjusted by the user depending on the needs. Since the file writing is faster than the file reading, the executed program can jump to the last written line of the file to ensure that the analyzed events are the most recently recorded. Depending on the set parameters, the code can deliver a profile within 2–5 s after the beam extraction from the accelerator. This program was successfully used during several data taking at GSI.

3.6 Fluence perturbation due to fiducial markers

The fluence perturbations due to fiducial markers, explained in section 1.6.3, were evaluated with a new measurement concept using a tracker system composed of six MIMOSA-28 sensors. This method uses high spatial resolution pixel detectors, and can provide three dimensional fluence distributions. The beam time campaign was performed at the Ion-beam Therapy Center in Marburg (MIT) [149] in Germany, and was divided in two sessions.
The first one intended to measure edge-scattering effects in targets with pronounced and sharp density gradients with a tracker system of MIMOSA-28 sensors. In the second session, several hours of beam time were dedicated to measure the fluence perturbations due to fiducial markers that are commercially available. Some hours were also dedicated to benchmark the measurements by using radiochromic films, which is a standard method for dose perturbation measurements. The results of the fluence perturbations from the fiducial markers are published in [150].

3.6.1 Edge-scattering effects

The experimental setup used to measure the edge-scattering effects with a tracker composed of MIMOSA-28 sensors and the beam profile analysis method are described in the two following sections.

3.6.1.1 Experimental setup

Two different targets were measured in the frame of this work, with different densities, shapes and thicknesses. The first target (referred to as *bone*) had a block shape, simulating cortical bone material with a thickness of 3 cm, and was manufactured with a round edge in order to have a more realistic case. The second target (referred to as *hammer*), made of gold had a triangular shape, with a maximal length of 18 mm, and a thickness of 0.5 mm. Figure 3.3 displays the targets and Table 3.8 describes their characteristics.

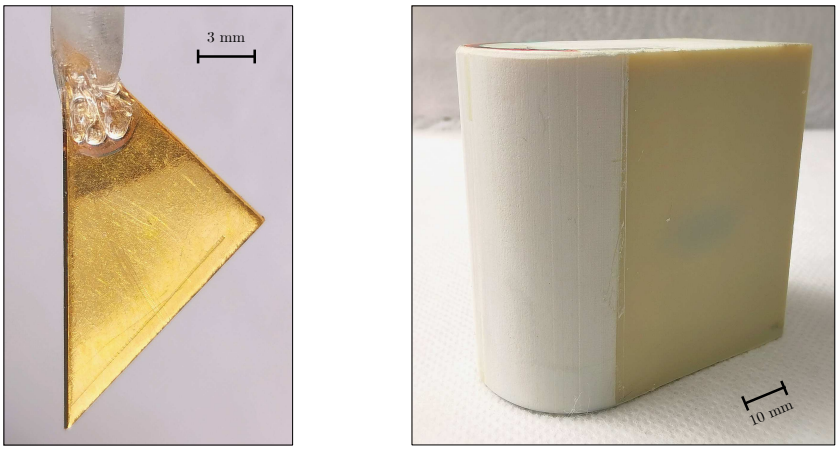

Figure 3.3: Targets used for the edge-scattering experiment: hammer target (left panel) and bone target (right panel).

Table 3.8: Characteristics of the targets used for the edge-scattering experiment.

Name	Shape	Material	ρ (g/cm^3)	Thickness (mm)
Bone	Block (round edge)	Cortical bone	1.82	30
Hammer	Triangle	Gold	19.3	0.5

The edge-scattering measurements were carried out at MIT, with 150.14 MeV proton beam. The experimental setup, depicted in Figure 3.4, consisted of two sets of three MIMOSA-28 sensors placed along the beam axis. A first run was performed without target for alignment purpose. The target was then positioned in-between the two sets of sensors, and adjusted along the lateral beam axis using the room laser system.

In the case of the bone target, the beam impinged on the round edge, while for the gold hammer, the beam covered the full target. The purpose of the first set of sensors was to verify the beam profile in front of the target. The second set of sensors was used for evaluating the fluence perturbation due to the target edge. The beam intensity was set lower than 5 kHz to avoid pile-up effects in the sensors.

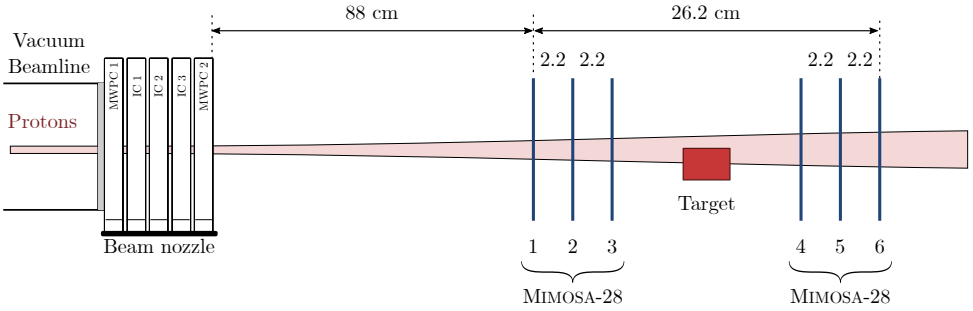

Figure 3.4: Experimental setup dedicated for the edge-scattering experiment with six MIMOSA-28 sensors placed along the beam axis. The target is positioned in-between two sets of three sensors, and adjusted along the lateral axis in order that the beam impinges the target edge. The measurements were performed at MIT with 150.14 MeV proton beam.

3.6.1.2 Beam profile analysis

This experiment aimed to verify the concept of measuring fluence perturbations due to edge-scattering effects, with a tracker system composed of several CMOS pixel sensors. The beam profiles were analyzed from the first sensor placed after the target (Figure 3.4). For this, the 2D beam profile (x, y) was extracted after the clustering and tracking reconstruction steps. The tracking was performed to reduce the noise contribution of the δ-electrons, which are produced from the interaction of the beam with the material layers of the setup, and therefore, considered as noise. Since these particles are emitted at large angles and generally penetrate only one sensor, the reconstructed tracks from the δ-electrons are in most cases not considered as valid ones.
The beam profiles were thus computed as the cluster positions from the clusters that were selected from the tracking. Since the targets used for this experiment were relatively large and thick, the profile in x was generated after integrating the 2D cluster map along the perpendicular direction y.

3.6.2 Fiducial markers

In this work, four common fiducial markers were selected to evaluate the induced fluence perturbation inside a target volume. Their characteristics are described in Table 3.9.

Table 3.9: Characteristics of the different fiducial markers used for the fluence perturbation measurements.

Name	Manufacturer	Material	Shape	Length (mm)	Diameter (mm)	Mass (mg)
Visicoil	IBA	Gold	coil-shaped	20	0.5	24
Gold Anchor #1	Naslund Medical AB	Gold	straight	11[b]	0.28	9[c]
Gold Anchor #2	Naslund Medical AB	Gold	folded	2.5[d]	0.28	14[e]
Acculoc Carbon marker	Carbon Medical Technologies	ZrO_2[a]	bone-shaped	3	1	5.5

[a] carbon-coated
[b] nominal length: 10 mm
[c] nominal mass: 8 mg
[d] unfolded: 17.5 mm, nominal length: 20 mm
[e] nominal mass: 17 mg

3.6.3 Experimental setup

The measurements were conducted at MIT with carbon ion beams, and two different methods were applied to determine the inhomogeneous scattering induced by fiducial markers: on the one hand with the Mimosa-28 pixel sensors, and on the other hand with EBT3 radiochromic films. The latter were used to validate the new concept of measuring the fluence perturbations due to fiducial markers with a set of CMOS pixel sensors. The two experiments were carried out with few months in-between. In order to perform clinically relevant measurements, each fiducial marker was placed inside a small water aquarium of 4 cm length and positioned at the isocenter of the treatment room. For better handling, the markers were glued to a polyethylene (referred to as *PE*) plate of 1 mm thickness, and positioned along the vertical axis perpendicular to the beam. In addition, a PE block of 9 cm length was placed in front of the water aquarium to simulate the healthy tissues of a patient. The beam energies were chosen in order to cover a range of 3 cm (slightly smaller than the length of the water aquarium). The energies, FWHM and the range in water of the carbon ion beams, used during the experiments at MIT, are listed in Table 3.10. The energies and FWHM at isocenter position were assumed as the nominal values from MIT (ensured by the regular QA), while the ranges were calculated with Lise++ [50]. The water equivalent path length of the experimental setup (computed with Lise++) was about 140 mm. The total range of the different ion beams used for the experiment was chosen to have enough energy to pass through the PE block, the water aquarium and the sensors placed after the water aquarium (see Figure 3.5 (bottom panel) in section 3.6.3.1).

Table 3.10: Beam energy, FWHM at the isocenter and range in water (calculated with LISE++) of the carbon ion beams used for the experimental measurements.

Energy (MeV/u)	FWHM (mm)	Range in water (mm)
278.84	5.6	150.4
294.97	5.5	165.1
310.61	5.4	179.9

3.6.3.1 MIMOSA-28 sensor measurements

To measure the fluence perturbation due to the fiducial markers, a tracker system of six MIMOSA-28 pixel sensors was placed at 0° with respect to the beam axis. The beam intensity was set to less than 5 kHz, and monitored using a 5 mm plastic scintillator (BC-400) placed upstream of the sensors.

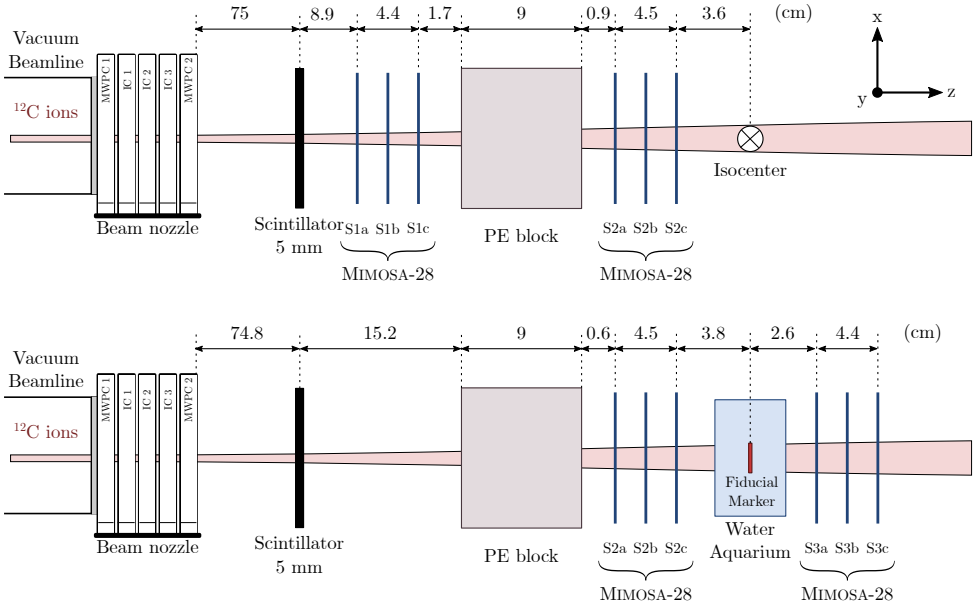

Figure 3.5: Experimental configurations used to measure the fluence perturbation of several carbon ion beams due to fiducial markers with six MIMOSA-28 pixel sensors placed along the beam axis.

Several beam profile measurements along the beam axis were performed for alignment purpose, and for benchmarking the measurements with other techniques (e.g., radiochromic films). Two sets of three sensors were placed on each side of the PE block (Figure 3.5 (top panel)). The beam profile measurements were performed with and without the PE block. The two sets of sensors were then moved to each side of the water aquarium (Figure 3.5 (bottom panel)), and a measurement with and without the PE block and

the water aquarium was performed. Afterwards, the fiducial markers were inserted into the water aquarium through the method explained in the previous section. The first three sensors were used to monitor the beam profile by verifying that it remains constant, while the three last sensors were used to measure the fluence perturbation induced by the marker.

3.6.3.2 Radiochromic film measurements

The experiment performed with the MIMOSA-28 sensors was validated with radiochromic films (GAFCHROMIC EBT3, Lot#: 06141702). EBT3 films have a total thickness of 278 µm, an active layer of 28 µm and are resistant to water during short time immersion [151]. They were cut in pieces of 6.4 × 6.8 cm^2, and protected with tape around the borders to prevent damage due to the water. During the irradiation, all films were placed in portrait orientation to avoid any changes in the film response due to its orientation [152]. The EBT3 films were then scanned after several hours using a VIDAR scanner (Dosimetry Pro Advantage) with a spatial resolution of 300 dpi (∼ 85 µm) and 16 bits resolution in portrait orientation [153].
Before the film analysis, a calibration curve was measured to correlate the film response to the delivered particle fluence from the accelerator. Therefore, a film from the same batch was irradiated with 8 different scanned squares, receiving a given fluence per square, within the range of 5×10^6–3×10^9 ions/cm^2, corresponding to a dose range of around 0–70 Gy, considering the film background. The gray values of the film were then calibrated according to the given fluence, and each irradiated film was analyzed by using the established calibration curve. The images from the films were processed using the software ImageJ [132].

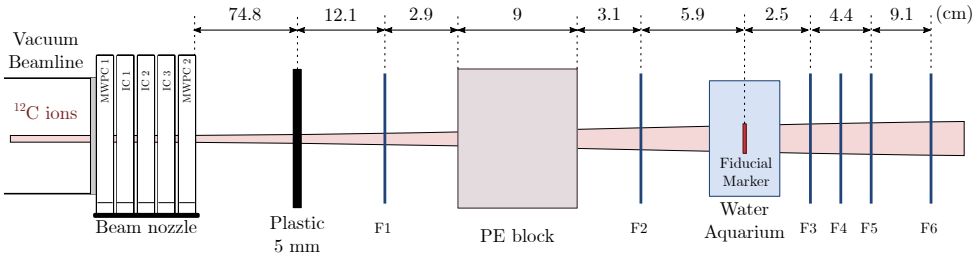

Figure 3.6: Experimental setup dedicated to measure the dose perturbation due to fiducial markers with EBT3 radiochromic films.

The radiochromic films were placed along the beam axis at similar positions than the MIMOSA-28 sensors, from the experiment described in section 3.6.3.1, in order to validate the measurement concept with a tracker system. The experimental setup is sketched in Figure 3.6 and the film positions i are referred to as *Fi*. A 5 mm plastic plate was placed in front of the first film to simulate the 5 mm plastic scintillator used during the CMOS sensors experiment. The same set of measurements was conducted: the beam profiles without any perturbations were measured without the 5 mm plastic, the PE block and the water aquarium. They were then measured with the addition of the 5 mm plastic, the PE block and the water aquarium. The perturbations from the fiducial markers were

later on measured by placing the marker inside the water aquarium at isocenter position (Figure 3.6), using the same technique as the one described in section 3.6.3.1. For the measurements with the fiducial markers, an additional film was inserted inside the water aquarium placed at 5 mm in front of the marker. This film is not represented in Figure 3.6 but was used to verify the stability of the beam profile during the measurements.

3.6.3.3 Beam profile analysis: MIMOSA-28 vs. radiochromic films

The experiment for the fluence perturbation due to fiducial markers using several CMOS pixel sensors aimed to provide a new measurement concept, which affords high precision measurements. The new measurement concept with the use of a tracker system was benchmarked against a standard measurement method with radiochromic films. In a first step, the beam profiles were analyzed from the measurements without perturbation, and in a second step they were analyzed from the measurements with the fiducial markers for the CMOS and film experiments (see Figures 3.5 and 3.6).
The MIMOSA-28 sensors data were processed by using QAPIVI, where the tracks could be reconstructed as described in section 3.1.1. Data from the radiochromic films were obtained from the scans, and calibrated as explained in section 3.6.3.2. From the reconstructed tracks, a 2D beam profile (x, y) can be extracted at any position along the z-axis. For both experiments, the beam profiles in x and y were obtained by integrating the distribution over the perpendicular directions y and x, respectively. Without perturbation due to the markers, the profiles were integrated over the full distribution. However, in the case that a fiducial marker was placed inside the water aquarium, the profiles in x were integrated over a smaller area in y that correlates to the length of the marker in order to evaluate its perturbation.
The data sets from the tracker and the films were analyzed independently, and normalized as a function of the profile integral in order to compare both measurement techniques. The normalization and shift of each x and y beam profile was performed by means of a cumulative distribution function (also referred to as *Gaussian integral function* Φ). In the case of the MIMOSA-28 beam profile analysis, each entry of the histogram was weighted as a function of the cluster size (see section 3.3). The applied weight was calculated following equation 3 of Spiriti et al. (2017) [9]. Since the absorbed dose is proportional to the deposited energy, this quantity is also correlated to the cluster size of MIMOSA-28. However, the energy resolution of the detector is low since the MIMOSA-28 output is a binary signal. The applied weight is thus a rough correction to the fluence profiles obtained with the CMOS sensors in order to get a more realistic comparison with the radiochromic films.

3.6.4 Fluence distribution measured with MIMOSA-28 sensors

The goal of this analysis part is to quantify the maximum value of the cold spot induced by the fiducial markers, and to determine its position along the beam axis with a precise and efficient method. With such purpose, a 3D fluence distribution is reconstructed after performing the tracking, which defines the trajectory of each single particle crossing the sensors. This 3D distribution is computed from all tracks, defined by 3D vectors, which can be reconstructed with the tracker placed after the water aquarium. For this, $10 \times 10 \times 100$ µm^3 voxels are computed, and the fluence in each voxel is specified by the

sum of all tracks passing through this voxel. The 3D fluence distributions are, therefore, the scoring of the total number of intersections between the reconstructed tracks and the voxels. The 2D fluence distribution (referred to as *fluence map*), presented in this study, illustrates the propagation of the perturbation in the (x, z) plane, integrated over a certain area along the y-axis. For the case of large targets, as the ones used for the experiment described in section 3.6.1, the integration was performed over the full area. In the case of the fiducial markers, the integrated area was chosen as for the beam profile analysis in section 3.6.3.3. The integration range in y-direction was varied to test the robustness of the chosen window. From the integrated 2D fluence map, the cold spots at any position along the beam axis were extracted. To determine the maximum cold spot, the beam profiles with and without marker were compared.

Chapter 4

Results & Discussion

In this chapter, the results from the different experiments described in the previous chapter are discussed. The performance of the alignment procedure was tested with experimental and simulated data, and the response of MIMOSA-28 was investigated for different ion species and energies. These preparatory steps were necessary to perform precise measurements for ion-beam therapy applications, like the characterization of beam profiles and the evaluation of the fluence perturbation induced by fiducial markers. The presented results of the alignment procedure and the fluence perturbation are published in [141] and [150], respectively.

4.1 Alignment procedure performance

The alignment procedure is a mandatory routine, which has to be performed before the data analysis, to be able to reconstruct particle tracks with high resolution. A successful convergence of the algorithm is achieved by the goodness of the alignment parameters, which must be better than the required track resolution. In this section, the results from simulated and experimental data are presented, and the performance of the new alignment procedure is benchmarked against the resulting accuracy of the alignment parameters.

4.1.1 Simulation results

The accuracy and precision of the alignment procedure were tested with Monte Carlo simulations for the setup geometries Geo1 and Geo2 (Table 3.4), beam configurations (Table 3.3), and misalignment scenarios Mis1, Mis2 (Table 3.5) and Mis3 (Table 3.6). The values $\overline{\delta x}$, $\overline{\delta y}$ and $\overline{\delta \phi}$, listed Table 4.1, represent the mean deviations between the calculated alignment parameters and the set-misalignments, averaged over six beam configurations for each misalignment scenario. These results fulfill the alignment procedure requirements for reconstructing tracks with high spatial resolution.
The accuracy and robustness of the results, with average deviations $\overline{\delta x}, \overline{\delta y} < 2$ µm and $\overline{\delta \phi} < 0.05°$, define the good reliability of the algorithm. The uncertainties of the alignment parameters, averaged over the six beam configurations, showed smaller values compared to the ones derived from the elements of the covariance matrix ${C_m^f}^{-1}$, defined in section 3.2.1.5. Since the results from the covariance matrix are less conservative, the

deviations from the averaged parameters of the different configurations are presented in Table 4.1. It can be observed that the uncertainty of the rotational parameter increases proportionally with the sensor distance along the beam axis. This systematic can be induced by different parameters, such as the so–called weak mode [140, 154] (e.g., torsion of the tracker) and the initial constraints. Since the rotation of the first plane is fixed, and the rotational parameter has a weak correlation with the other translational parameters, small errors can be induced on the rotational alignment parameter results with an increase proportional to the z-distance.
The influence of the rotation constraint was tested after performing the tracking for the case that the rotation of the first plane was fixed vs. the case that the rotations of the first and last planes were fixed during the alignment procedure. Even though the deviations δ on the rotational alignment parameters were smaller in the second case, the resulting residuals of the tracks were the same in both cases. In this work, only the first rotational parameter was fixed in order to correct the initial torsion of the setup. The CPU time for performing the complete alignment procedure was ~ 50 s in single-threaded mode for 50000 events.

Table 4.1: Average deviations between the calculated alignment parameters and the set-misalignments for all sensors (1–6). The deviations were averaged over six beam configurations, listed in Table 3.3. The standard deviations of the δ-values are given in parentheses, and indicate their fluctuations.

	Geo1 – Mis1			Geo1 – Mis2		
	$\overline{\delta x}$ (µm)	$\overline{\delta y}$ (µm)	$\overline{\delta\phi}$ (°)	$\overline{\delta x}$ (µm)	$\overline{\delta y}$ (µm)	$\overline{\delta\phi}$ (°)
1	0.00	0.00	0.000	0.00	0.00	0.000
2	0.01 (0.01)	0.02 (0.03)	0.005 (0.003)	0.21 (0.24)	0.19 (0.20)	0.008 (0.005)
3	0.03 (0.01)	0.03 (0.03)	0.010 (0.007)	0.38 (0.45)	0.41 (0.49)	0.017 (0.010)
4	0.02 (0.01)	0.02 (0.02)	0.015 (0.010)	0.60 (0.70)	0.71 (0.84)	0.025 (0.014)
5	0.02 (0.02)	0.02 (0.01)	0.020 (0.013)	0.83 (0.96)	0.87 (1.03)	0.034 (0.019)
6	0.00	0.00	0.025 (0.016)	0.00	0.00	0.042 (0.023)
	Geo2 – Mis1			Geo2 – Mis2		
	$\overline{\delta x}$ (µm)	$\overline{\delta y}$ (µm)	$\overline{\delta\phi}$ (°)	$\overline{\delta x}$ (µm)	$\overline{\delta y}$ (µm)	$\overline{\delta\phi}$ (°)
1	0.00	0.00	0.000	0.00	0.00	0.000
2	0.08 (0.09)	0.07 (0.03)	0.006 (0.008)	0.12 (0.09)	0.12 (0.06)	0.005 (0.004)
3	0.13 (0.11)	0.10 (0.06)	0.011 (0.012)	0.18 (0.15)	0.14 (0.08)	0.010 (0.007)
4	0.14 (0.13)	0.10 (0.07)	0.017 (0.015)	0.23 (0.19)	0.31 (0.17)	0.014 (0.011)
5	0.13 (0.09)	0.05 (0.06)	0.022 (0.018)	0.28 (0.28)	0.29 (0.25)	0.019 (0.014)
6	0.00	0.00	0.028 (0.015)	0.00	0.00	0.024 (0.016)

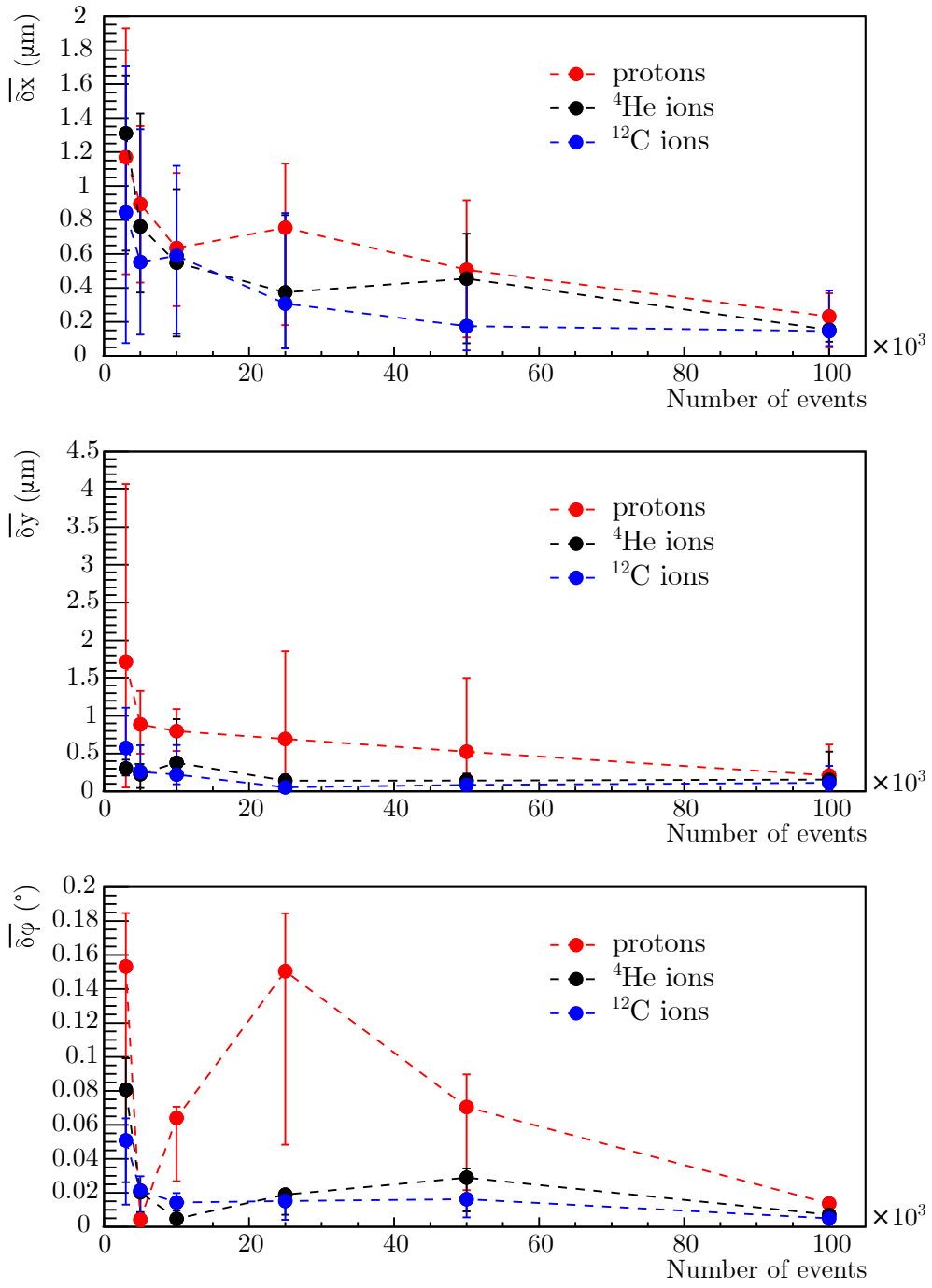

Figure 4.1: Average deviations $\overline{\delta x}$ (top), $\overline{\delta y}$ (middle) and $\overline{\delta \phi}$ (bottom) between the calculated alignment parameters and set-misalignments, for the Monte Carlo simulations, as a function of the number of events, for 150 MeV/u protons, ^{4}He and ^{12}C ions with the scenario Geo2 – Mis3. The δ-values are averaged over all sensors, and the error bars represent the range (min–max) of the δ-values.

The alignment procedure efficiency, in terms of time consumption, for converging to the required values, was evaluated for different amount of events given to the algorithm for protons, ^{4}He and ^{12}C ions at 150 MeV/u for the setup geometry Geo2. The setup geometry Geo1 was also tested for 150 MeV/u ^{4}He ions. The average deviations between the calculated alignment parameters and set-misalignments were evaluated, and are shown in Figure 4.1. The average deviations of the translation in x (Figure 4.1 (top)) and y (Figure 4.1 (middle)) are smaller than 2 µm for a minimum of 5000 events. However, the rotational parameter, being more sensitive to the scattering, converges slower (Figure 4.1 (bottom)), and a minimum of 50000 events is required for the convergence of the calculated alignment parameters to the real misalignment values. The heavier the particle is, the faster the algorithm converges because of the stronger angular deflections for light particles due to multiple Coulomb scattering. The results of the alignment parameters obtained for the setup geometry Geo1 were very similar to the ones presented for the setup geometry Geo2. In addition, results are independent from the ion optical parameters of the beam (FWHM and divergence) since the results remained the same even when the divergence values of Table 3.3 were increased to larger values up to 20 mrad.
The performance of the alignment procedure as a function of the rotational misalignment of the sensors were computed for 150 MeV protons and 300 MeV/u ^{12}C ions with the setup geometry Geo2. The translations dx and dy were set as the misalignment scenario Mis3 (Table 3.6), and the rotational parameter was varied from 0.5° up to 10° compared to the first sensor. Figure 4.2 depicts the deviations of the translations as a function of the rotational misalignment for 150 MeV protons. For $d\phi$ larger than 3°, the deviations of the translations increase significantly. The same test was performed for 300 MeV/u ^{12}C ions and very similar results were obtained. The large deviations of the calculated alignment parameters for $d\phi > 3°$ can be explained by the inaccurate approximation of $\cos(\phi) \approx 1$. However, in practice, the alignment accuracy of $\pm$ 3° for a stable mechanical setup is easily feasible.

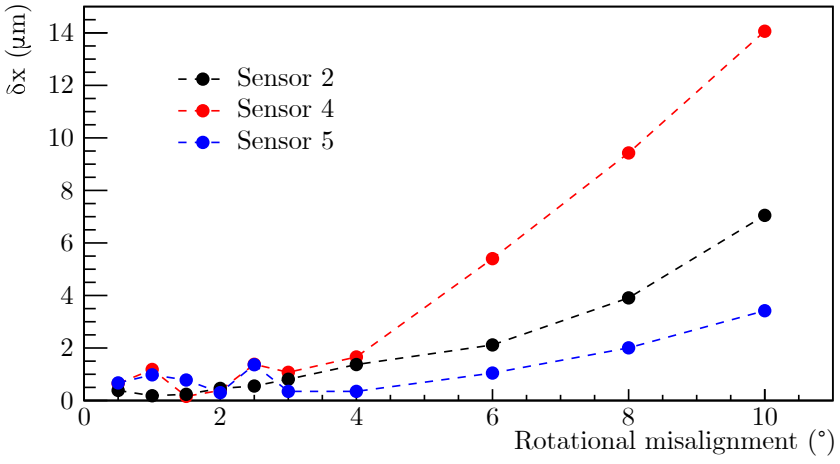

Figure 4.2: Deviation δx as a function of the rotational set-misalignments of different sensors for 150 MeV protons with the setup geometry Geo2.

4.1.2 Experimental results

To evaluate the performance of the alignment procedure for experimental data, the residuals of the reconstructed tracks were computed, and used as a control of the procedure success. As presented in Table 3.1, the angular distribution from the multiple Coulomb scattering for a set of six sensors is small for therapeutic ion beams. However, the track resolution depends on the setup geometry, influenced by the distance of the air gaps between the sensors. For particle energies presented in Table 3.1, the track resolution, for a set of six MIMOSA-28 placed along the beam axis with air gaps < 3 cm, is better than 10 µm. When increasing the air gaps, the track resolution becomes worse. Since the procedure developed in this work is based on the clustering, the influence from the air gaps between the sensors is negligible. Setup geometries with small air gaps (compact geometry) and bigger ones (spread geometry) are presented.

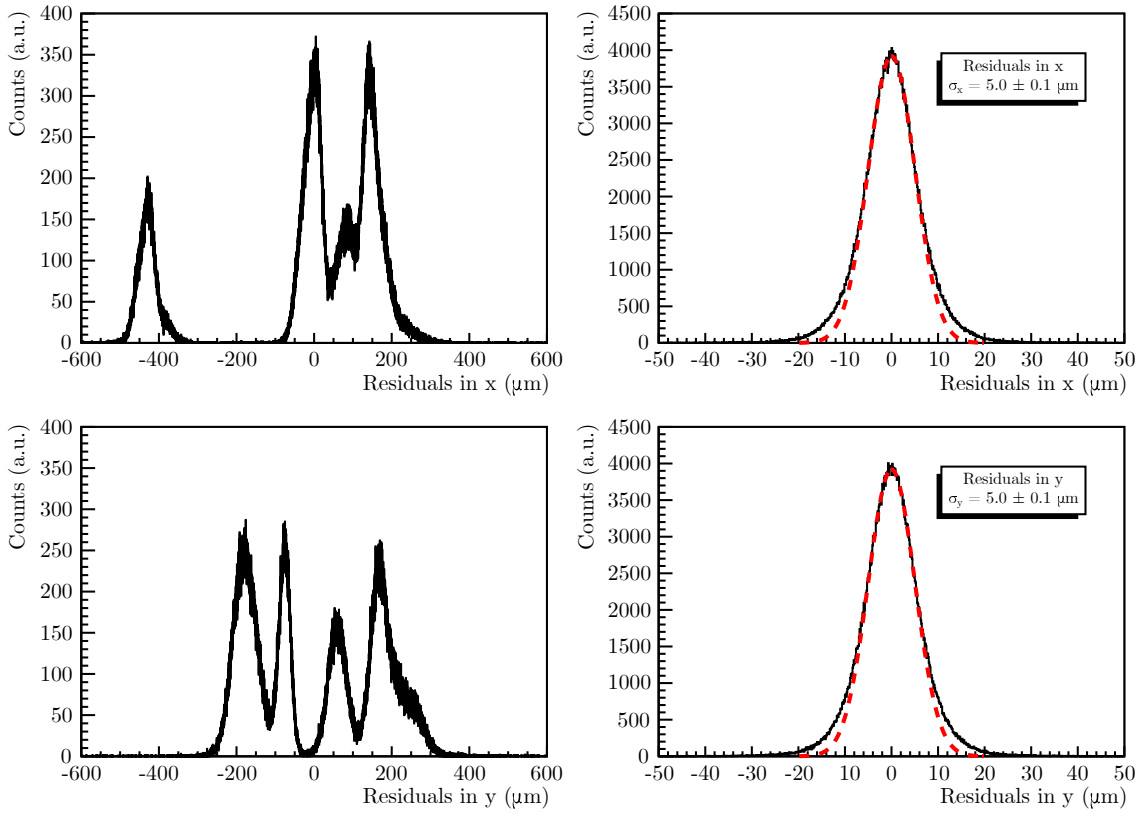

Figure 4.3: Histograms of the residuals in x (top panels) and y (bottom panels), before (left panels) and after (right panels) the alignment procedure ClusAlign for 220.51 MeV/u ^{4}He ions, for all sensors and all tracks (from the experimental data recorded at HIT). The red dotted line defines the Gaussian fit of the residuals.

The alignment procedure was tested on experimental data, obtained with the setups described in section 3.2. To show the effect of the procedure, the tracking was computed before and after the alignment. The residuals in x and y for 220.51 MeV/u ^{4}He ions are shown for all sensors in Figure 4.3. The residual distributions prove the success of the alignment procedure. A track resolution of 5.0 µm in x and y, for the presented experimental data, is obtained from the width of the residual distributions (as explained in section 3.1.1.3).

Table 4.2: Average value of the alignment parameter results over six energies, in the range of 80–220 MeV protons (from the experimental data recorded at the Proton Center Therapy in Trento), calculated with ClusAlign, TrackAlign and Millepede II. The standard deviation of the average value of the alignment parameters is given in parentheses.

Sensor	dx (µm)	dy (µm)	$d\phi$ (°)
		ClusAlign	
1	0.0	0.0	0.00
2	−125.5 (1.5)	159.9 (2.7)	−0.25 (0.03)
3	−5.4 (1.5)	157.7 (2.9)	0.14 (0.03)
4	122.6 (0.3)	291.2 (0.7)	−0.44 (0.08)
5	165.1 (0.7)	270.3 (0.9)	0.17 (0.08)
6	0.0	0.0	0.17 (0.09)
		TrackAlign	
1	0.0	0.0	0.00
2	−129.7 (1.4)	123.5 (6.5)	0.03 (0.17)
3	−9.0 (1.6)	122.9 (5.5)	0.04 (0.06)
4	114.5 (2.3)	263.9 (3.9)	−0.16 (0.27)
5	157.4 (3.0)	239.5 (3.9)	−0.04 (0.03)
6	0.0	0.0	−0.08 (0.02)
		Millepede II	
1	0.0	0.0	0.00
2	−126.0 (2.9)	155.5 (5.5)	−0.18 (0.13)
3	−5.8 (3.0)	153.1 (5.7)	0.21 (0.14)
4	123.0 (1.3)	287.4 (2.9)	−0.28 (0.28)
5	165.4 (1.8)	266.5 (2.9)	0.33 (0.28)
6	0.0	0.0	0.36 (0.34)

Since the accuracy of the alignment procedure is independent from the setup geometry, it is important to verify the robustness of the algorithm for different configurations. Each setup geometry was tested with several particle energies: on the one hand proton beams were used with a spread geometry, and on the other hand helium ion beams were used with a compact geometry. The average value of the alignment parameters were computed with the alignment procedure developed in this work (ClusAlign), and compared to the results obtained with the alignment procedure originally implemented in Qapivi (TrackAlign). The procedure was also benchmarked against the state-of-the-art algorithm Millepede II, used in stand-alone where the input parameters were given after fitting the same selection of data used for ClusAlign. In Table 4.2, the average value of the alignment parameter results calculated with the different alignment procedures are listed.
The alignment parameter results of ClusAlign and Millepede II are in agreement. The average values of TrackAlign, originally implemented in Qapivi, differ from the ones obtained with ClusAlign and Millepede II, with discrepancies up to 25 µm for the translations and 0.4° for the rotation. All alignment parameter results obtained with ClusAlign showed uncertainties < 3 µm for the translations and $< 0.1°$ for the rotation, concerning the experimental data. As explained in section 4.1.1, the deviation of the rotational parameter increases proportionally with the z-distance. To verify the influence of the rotational parameter on the track resolution, the first and the last rotations were fixed during the alignment procedure. As for the simulated data, the small error on the rotational parameter has no relevant influence on the track residuals.
The residuals in x and y for all sensors were computed after the alignment procedure of the different algorithms (ClusAlign, TrackAlign and Millepede II) with a compact setup geometry for 220.51 MeV/u ^{4}He ions, and are depicted in Figure 4.4. The residual distributions from ClusAlign illustrate the significant improvement of the procedure implemented in this work compared to TrackAlign. The residuals computed after performing the alignment procedures ClusAlign and Millepede II are comparable and result in a track resolution of 5.0 µm.

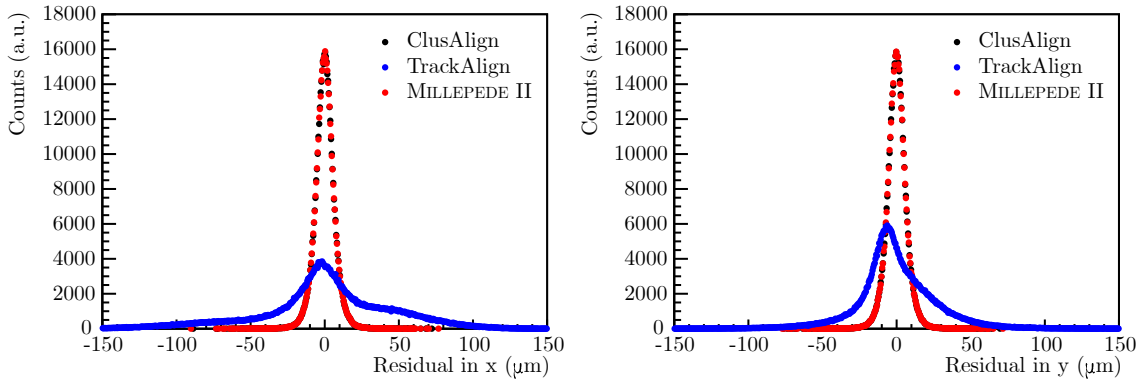

Figure 4.4: Histograms of the residuals in x (left panel) and y (right panel) after the alignment procedure with ClusAlign (black dots), TrackAlign (blue dots) and Millepede II (red dots) for 220.51 MeV/u ^{4}He ions (from the experimental data recorded at HIT), for all sensors and all tracks.

4.2 Response of Mimosa-28

In this section, the response of the Mimosa-28 sensor, for different charged particles and energies, was investigated with respect to the cluster size, which is determined from the number of pixels fired by the same particle.

4.2.1 Cluster size

4.2.1.1 Generation 1 vs. Generation 2

The response of two sensor generations of Mimosa-28, mentioned in section 2.2.2, were studied. As explained in section 3.3.1, the experimental setup consisted of six sensors placed along the beam axis, including two sensor generations, without any target for 220.51 MeV/u ^{4}He ions. Figure 4.5 shows the cluster size distributions for both sensor generations. Cluster size distributions for sensors of Generation 1 (sensor 4 and 6) and Generation 2 (sensor 1 and 3) are shown in the left and right panels, respectively.

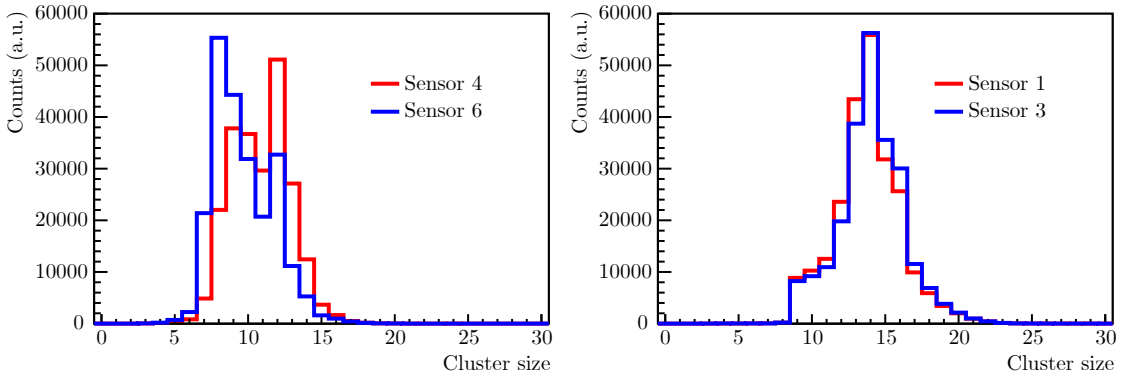

Figure 4.5: Cluster size distributions from the sensors of Generation 1 (left panel) and Generation 2 (right panel) for 220.51 MeV/u ^{4}He ions.

The distributions from the first sensor generation describe a double structure where two main cluster sizes are visible, while a single peak is formed for the second sensor generation. It is also important to note that sensor 4 and sensor 6 have different distributions even though they belong to the same generation. From one sensor to another, the deposited energy is slightly different due to the energy loss in the 50 µm thickness of Mimosa-28 and the air gaps in-between the sensors. However, the impact on the cluster size distribution in negligible for the particle energies used during this experiment. Moreover, the cluster distributions from the second generation (sensor 1 and 3) are in agreement, which confirms the small impact of the energy losses at these energies. The modifications performed on the second generation, concerning the noise repartition over the sensor area, manifest a significant improvement of the response homogeneity of Mimosa-28. Even though this sensor has a low energy resolution due to its binary output, this enhancement contributes to a better cluster definition with respect to the energy loss in the sensor.

4.2.1.2 Cluster size contributions

As explained in section 2.1.2, the electrons, created by ionizations in the epitaxial layer of the MIMOSA-28 sensor, thermally diffuse until they are collected by the diode of a pixel. Since the depleted region of this detector is small, the diffusion factor of the produced electrons plays an important role. Therefore, the cluster size depends on the energy deposited by the particle inside the sensitive volume. Additionally to the energy loss, the spatial energy distribution of the particle also contributes to the cluster size. As explained in section 1.4.1, the track structure depends on the particle species and its energy. Even though the particle track has a radial dose distribution smaller than the pixel pitch of 20.7 µm, the response of the detector is a convolution between the track structure, and the diffusion of the created electrons. In Figure 4.6, the cluster size is displayed, for all measurements performed at different accelerator facilities, for MIMOSA-28 Generation 2, as a function of the deposited energy, following the analysis method described in section 3.3.2. The asymmetric errors of the deposited energy are due to the non-linearity of the energy loss per path length as a function of the primary kinetic energy of the particle (section 1.3.2). The last measurement point shows a larger error than the other measurements since the sensor was positioned close to the Bragg peak region of the primary beam.

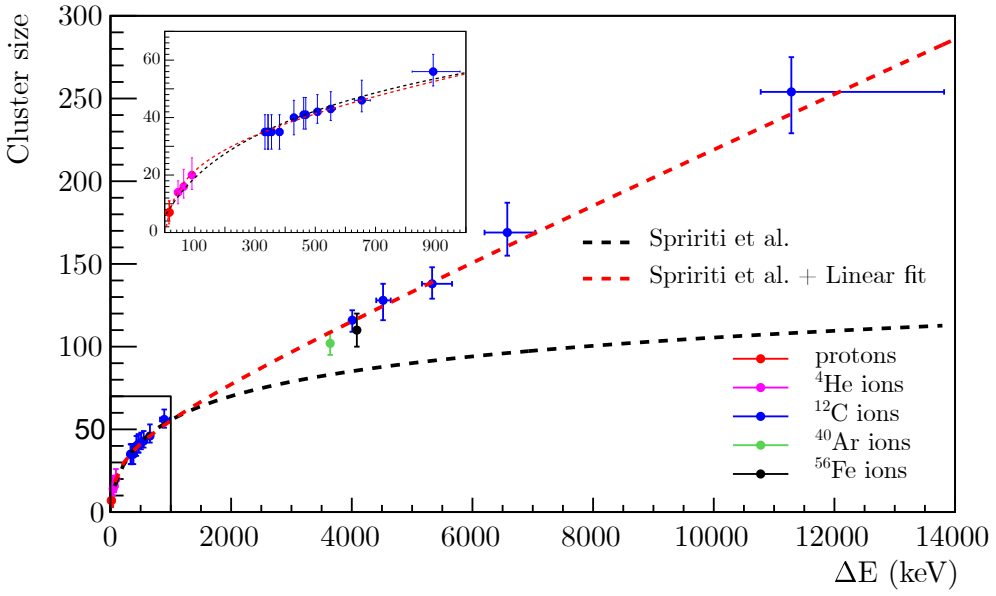

Figure 4.6: Measured cluster size as a function of the deposited energy in the active silicon layer of Mimosa-28.

The empirical model, used to fit the data collected with MIMOSA-18 by Spririti et al. (2017) [9], can not reproduce the trend of the experimental data from this work, properly. For a deposited energy < 1 MeV in 14 µm silicon layer, the model can be used to estimate the cluster size as a function of the energy loss. However, for a higher deposited energy, significant discrepancies are observed between the model and the experimental data.

In Figure 4.6, the model from Spiriti et al. was extended by a linear term, and thus fits better the number of pixels per cluster n_p for a deposited energy ΔE as:

$$n_p = \underbrace{2\pi r_s \ln\left(\frac{\Delta E}{2\pi E_g T_s} + \delta\right)}_{\text{Spriti et al.}} + \underbrace{a\Delta E + b}_{\text{Linear term}} , \tag{4.1}$$

where $E_g = 3.6$ eV for silicon, and the values of r_s, T_s, δ, a and b are listed in Table 4.3.

Table 4.3: Parameters used to fit the experimental data in Figure 4.6 from Spiriti et al. (2017) [9] and from equation 4.1.

	r_s	T_s	δ	a (keV^{-1})	b
Spririti et al.	3.61	4261.15	1.27	-	-
Equation 4.1	1.39	858.61	0.45	0.02	4.81

In Figure 4.7, radial dose distributions of different ion beams crossing a silicon volume equivalent to the one of Mimosa-28 sensor, are displayed. The radial dose distributions were computed with the Monte Carlo code Trax [67] for several ion species and energies, similar to the ones used in the experimental measurements.

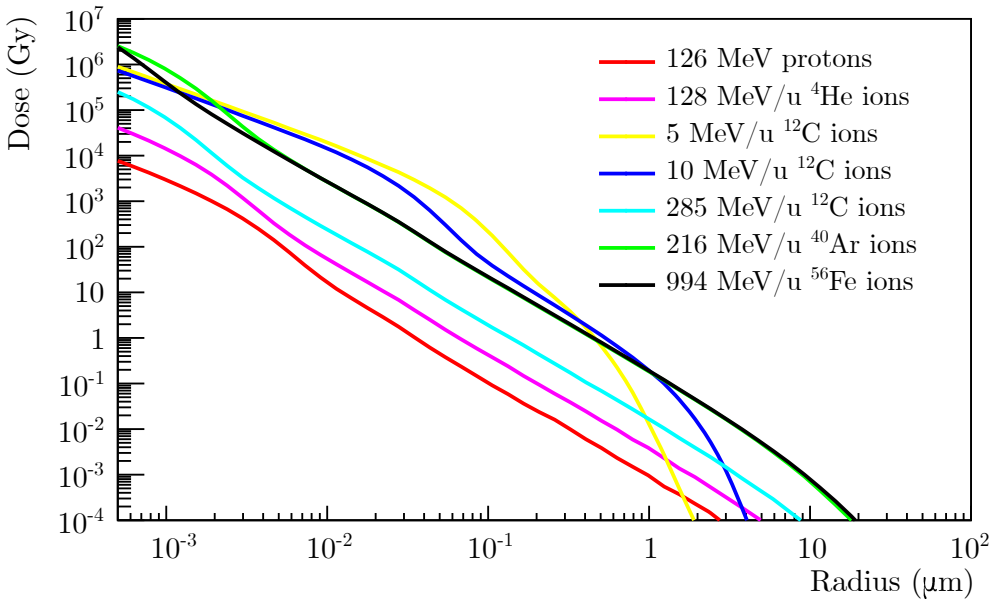

Figure 4.7: Radial dose distributions for 126 MeV protons (red line), 128 MeV/u ^{4}He ions (magenta line), 5 MeV/u ^{12}C ions (yellow line), 10 MeV/u ^{12}C ions (blue line), 285 MeV/u ^{12}C ions (cyan line), 216 MeV/u ^{40}Ar ions (green line) and 994 MeV/u ^{56}Fe ions (black line). These distributions were computed with the Monte Carlo code Trax [67]. Data courtesy of Dr. Daria Boscolo.

This study shows that the cluster size depends on the deposited energy of the primary particle. The results in Figure 4.6, do not show a dependence on the ion species. For instance, the high energy ^{56}Fe ions and the low energy ^{12}C ions with a similar energy loss in the sensor of around 4 MeV have a comparable cluster size, even though the radial dose distribution depends on the particle species (Figure 4.7). Other experiments could be performed in the future, to fully characterize MIMOSA-28, such as a threshold scan, and the study of the cluster size for other ion species and energies. The results from this work can be used for a better understanding of such a sensor. The FOOT experiment uses MIMOSA-28 as vertex detectors, and the simulation of the sensor is based on the experimental data presented in Figure 4.6. In addition, a future analog sensor based on MIMOSA-28 is intended to be produced within the STRONG project.

4.2.2 Response to different fragments

In this analysis, the mean cluster size was computed, following the method described in section 3.3.2. In Figure 4.8, the mean cluster size distribution, obtained with the tracker vt–track consisting of three MIMOSA-28 sensors placed behind a water phantom of 4 cm thickness for 287.50 MeV/u carbon ions, is depicted.

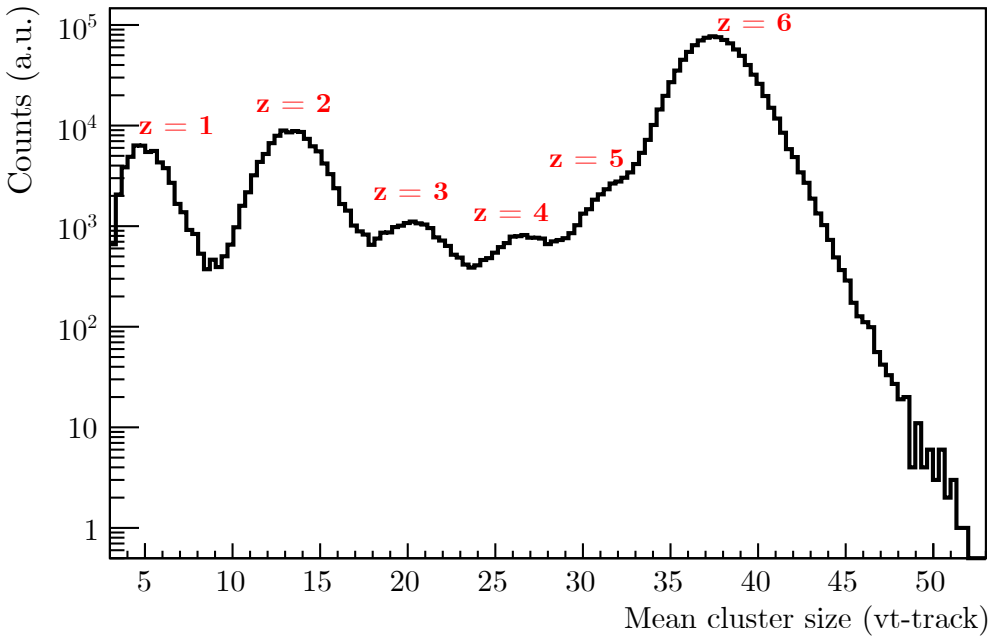

Figure 4.8: Mean cluster size distribution computed with a set of three MIMOSA-28 sensors placed behind a water phantom of 4 cm thickness, for 287.50 MeV/u carbon ions.

The same analysis was performed with the tracker bm–track, placed in front of the water phantom. In Figure 4.9, the 2D histogram defines the mean cluster size of vt–track as a function of the mean cluster size of bm–track, for 287.50 MeV/u carbon ions. From this analysis, it is possible to evaluate the correlation between the tracks in front and behind the target, similar to a ΔE–ΔE telescope. Figures 4.8 and 4.9 illustrate the response of MIMOSA-28 to a complex field composed of primary ions and the different emitted frag-

ments. The particle identification can not be performed precisely due to the low energy resolution of such sensor. However, the pronounced peak delivers reliable information to separate primary ions and lighter fragments.

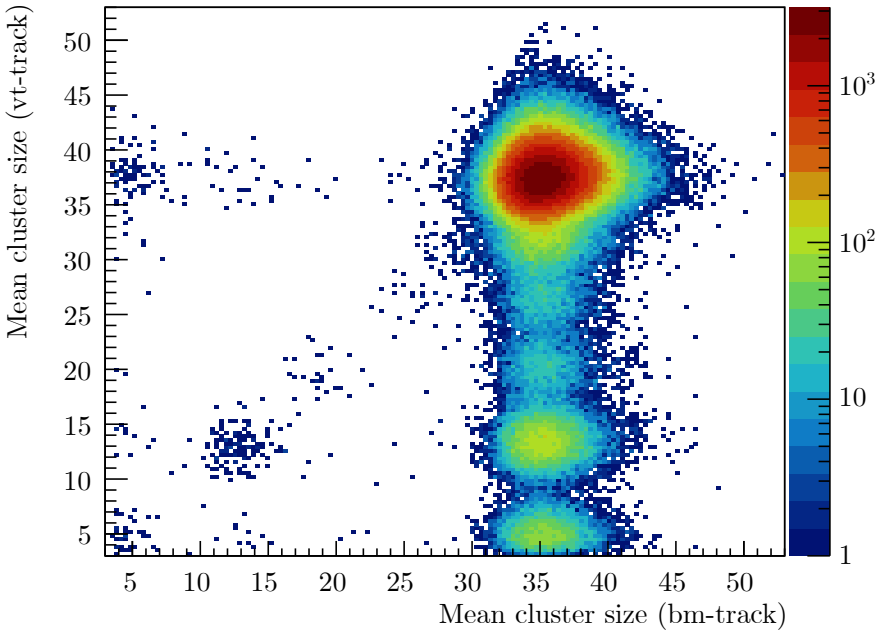

Figure 4.9: 2D histogram of the mean cluster size of vt–track as a function of bm–track from the two sets of MIMOSA-28 sensors placed in front and behind a water phantom of 4 cm thickness, for 287.50 MeV/u carbon ions.

This study revealed the dependence of the cluster size as a function of the energy loss in the MIMOSA-28 sensor. Even though the energy resolution of this sensor is low, the cluster size can be used as an information to separate the primary ions from the lighter fragments, and hence, improve the tracking. This is useful, especially, for larger and more complex multi detector experimental setups like FOOT [121].

4.3 Lateral beam spread along the longitudinal axis

In this section, the lateral beam spread was investigated for different proton beams at several therapeutic energies. The beam profiles, measured with a set of MIMOSA-28 sensors, are presented and compared to the predictions of the transport code SCATTMAN [5, 10].

4.3.1 Beam profiles from MIMOSA-28 sensors

The beam profiles were measured along the beam axis with the experimental setup described in Figure 3.2 (top panel). Figure 4.10 illustrates an example of 2D cluster maps for sensor 1, and their projections in x and y, for 123.3 MeV and 219.8 MeV proton beams. The profiles in x and y were fitted with a Gaussian function.

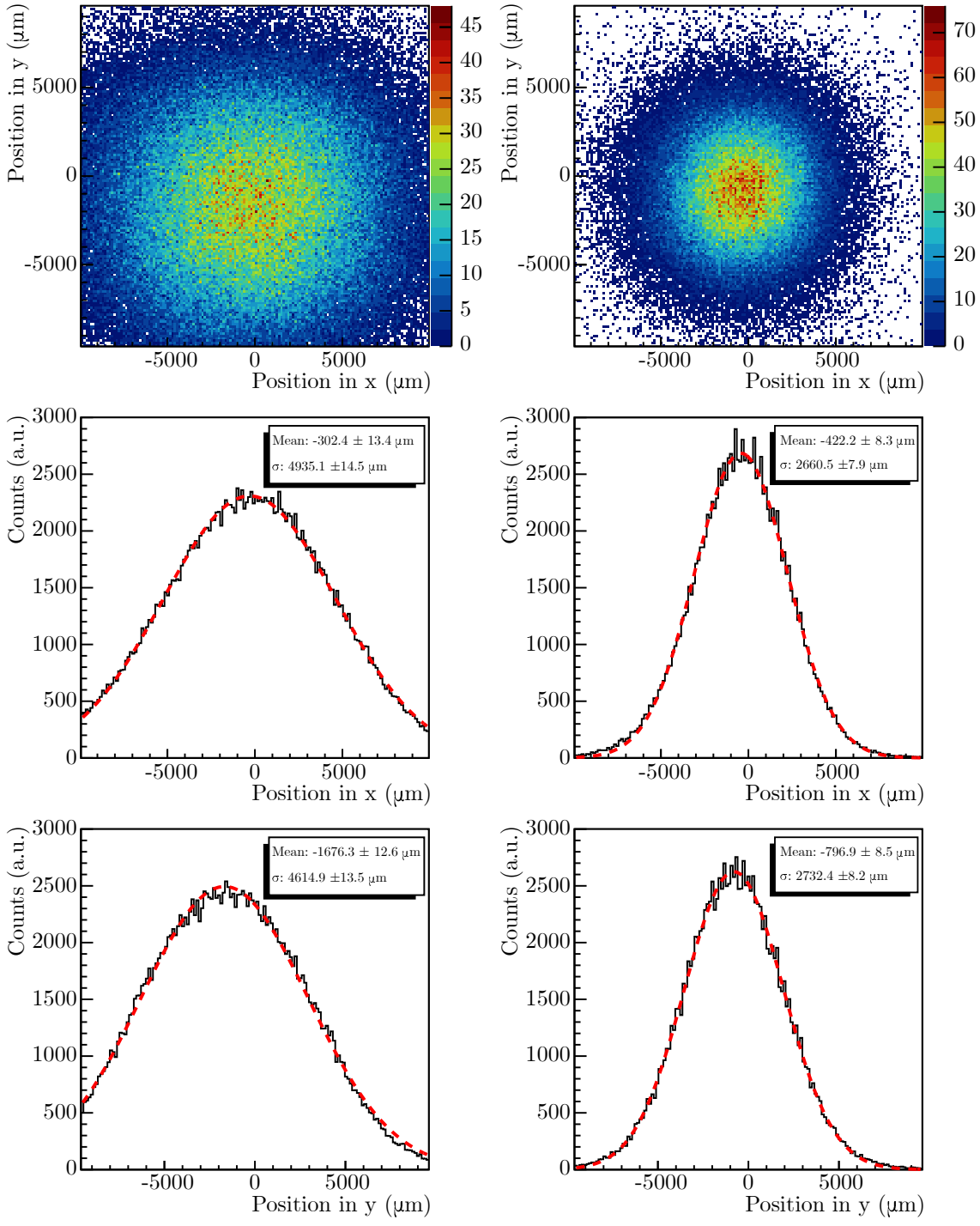

Figure 4.10: Beam profiles in x (middle panels) and y (bottom panels), computed from the 2D cluster maps (top panels), for 125.3 MeV (left panels) and 219.8 MeV (right panels) proton beams. The data, measured in the experimental room of the Proton Therapy Center in Trento, were obtained with sensor 1 from the experimental setup in Figure 3.2 (top panel). The red dotted line represents the Gaussian fit.

The profiles have a width of around 5 and 2.7 mm for 125.3 and 219.8 MeV protons, respectively. The larger width at lower energy is due to the increase of the angular distribution that can be estimated by the Highland formula (equation 1.4). The Gaussian fit can reproduce the measured data, but could be improved by its convolution with more complex functions to better fit the profile tails. Several studies were performed with a description of different parametrization models [155, 156]. However, a simple Gaussian fit was used in this work since the profile tails were not well measured due to the size of the sensor.

4.3.2 Particle transport

The particle transport code SCATTMAN, described in section 3.4.2, was compared to the measured data obtained with the experimental setup described in Figure 3.2 (top panel). The beam profiles, measured with the MIMOSA-28 sensors at different positions along the beam axis, were projected in x and y and fitted with a Gaussian function, as shown in Figure 4.10. In Figure 4.11, the beam widths σ_x and σ_y, obtained from the Gaussian fit of each sensor profile, are displayed as a function of the distance from the exit window, for 125.3, 188.8 and 219.8 MeV proton beams. In the same figure, the lateral beam spread along the longitudinal axis, which was determined from SCATTMAN, is shown. The initial ion optical parameters obtained from the fit optimization for the corresponding proton beams are listed in Table 4.4.

Table 4.4: Initial ion optical parameters obtained from SCATTMAN for different proton beams illustrated in Figure 4.11, and measured at the Proton Therapy Center in Trento.

		σ_0 (mm)	$\sigma_{\alpha,0}$ (mrad)	k_0 (mm)
125 MeV	x-axis	3.8	3.1	−770
	y-axis	3.5	6.6	−820
189 MeV	x-axis	2.0	1.0	460
	y-axis	2.2	3.8	−790
220 MeV	x-axis	1.4	1.3	67
	y-axis	1.7	3.2	−620

The initial ion optical parameters obtained from SCATTMAN vary in x and y for each particle beam. With the presented method, the beam width along the z-axis was determined with only six measured points. However, the robustness of the results could be improved in case that the beam profile would be measured with more spread distances along the z-axis, especially with measurement points closer to the exit window. In particle therapy, the beam width should be well known at the isocenter in the therapy room, due to the regular QA. In Table 4.5, the beam widths σ_x and σ_y obtained in this work were computed at isocenter position (120 cm from the exit window), and compared to the ones obtained one year earlier by Tommasino et al. (2017) [144]. The latter used the Lynx detector [157], which couples a scintillating screen with a charge couple device.

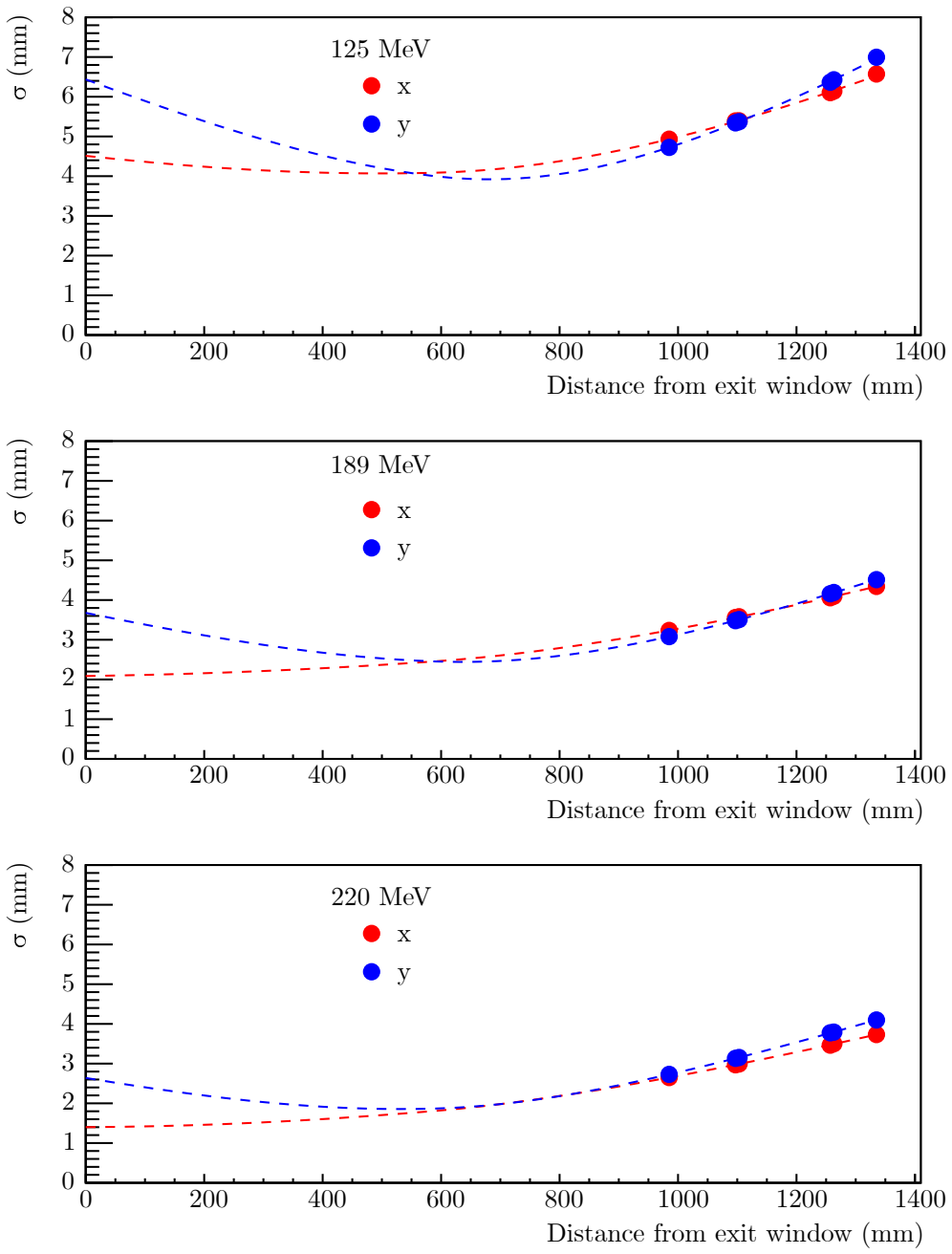

Figure 4.11: Lateral beam profile measurements of MIMOSA-28 sensors in x and y, and fitted with the transport code SCATTMAN for 125.3 MeV (top panel), 188.8 MeV (middle panel) and 219.8 MeV (bottom panel) proton beams. The data from the MIMOSA-28 sensors were recorded in the experimental room at the Proton Therapy Center in Trento.

Table 4.5: Beam widths in x and y obtained from the measurements performed in this work with MIMOSA-28 sensors for different energies proton beams at isocenter position. The measurements by Tommasino et al. (2017) [144] are also listed for the same z-position.

Energy (MeV)	σ_x (mm)	σ_x (mm) [144]	σ_y (mm)	σ_y (mm) [144]
90.8	7.35	6.04	7.58	6.15
125.3	5.90	4.90	5.98	5.09
148.5	5.15	4.39	5.22	4.52
164.4	4.65	4.02	4.76	4.19
188.8	3.87	3.66	3.90	3.83
219.8	3.28	3.10	3.52	3.08

The values in Table 4.5 show deviations between the measured beam widths with MIMOSA-28 and the ones in [144]. These deviations can be explained by the fact that the measurements were performed in the experimental room in the Trento Therapy Center, which means that the regular QA is not performed as for a patient treatment room. This can lead to deviations on the beam profiles from one day to another. In addition, the beam widths measured in this work are systematically larger than the ones from [144]. This could also be explained by the additional multiple Coulomb scattering caused by the sensors placed in front of the isocenter position while for the work in [144], the detector was placed only at the isocenter position.

4.4 Fluence perturbation due to fiducial markers

In this work, the results of the fluence perturbations due to fiducial markers are presented. In the first part, the edge-scattering effects are described with a proof-of-concept of the new measurement method, using a tracker system of six CMOS pixel sensors. In the second part, the fluence perturbation results from inhomogeneous scattering due to fiducial markers are reported, and are published in [150]. The measurements aimed to quantify the fluence perturbation caused by these markers used in particle therapy, detailed in section 1.6.

4.4.1 Edge-scattering effects

As explained in section 1.3.5, a particle beam passing through a target with sharp edges and strong density gradients suffers inhomogeneous scattering, creating fluence perturbations. In this section, the results from the experiment described in section 3.6.1 are presented.

4.4.1.1 Beam profiles of MIMOSA-28 sensors

The 2D cluster maps were computed following the method described in section 3.6.4 for the bone and the gold hammer targets, described in Table 3.8. The cluster map and its projection in x, from the first sensor placed behind the target of the experimental setup (Figure 3.4), are displayed in Figures 4.12 and 4.13 for the bone and the hammer targets,

respectively. In both cases, the fluence perturbations can be observed for a proton beam impinging on the target edge. For the bone target, one overshoot and one undershoot are produced from the round edge of the target placed around zero along the x-axis. In the case of the hammer target, the beam covered the full target area, and several perturbations were induced by the different edges of the triangular shaped target. These profiles in Figures 4.12 and 4.13 illustrate the fluence perturbations at the first sensor position placed behind the target along the z-axis.

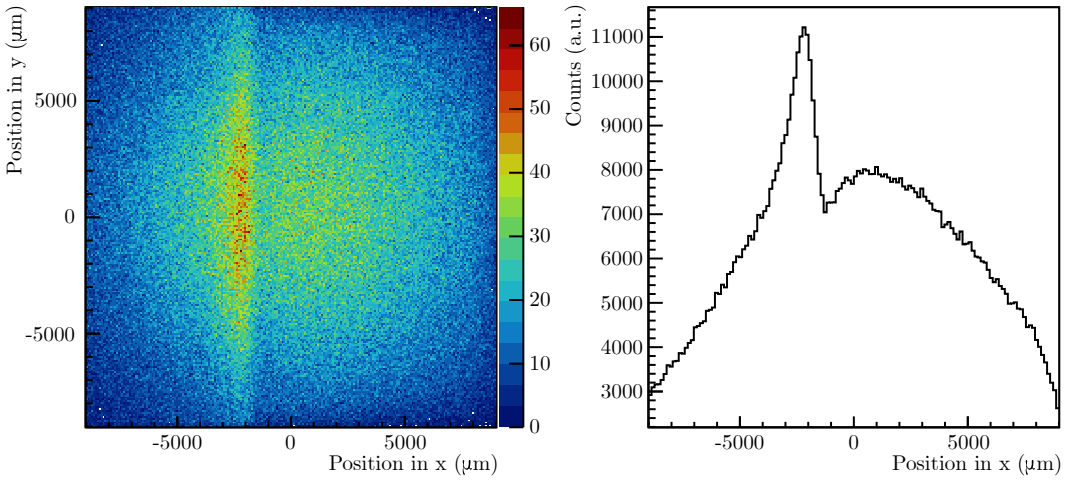

Figure 4.12: Two dimensional beam profile from MIMOSA-28 sensor (left panel), and its projection in x (right panel), for 150.14 MeV proton beam from the experimental measurements performed at MIT with the bone target placed along the beam axis.

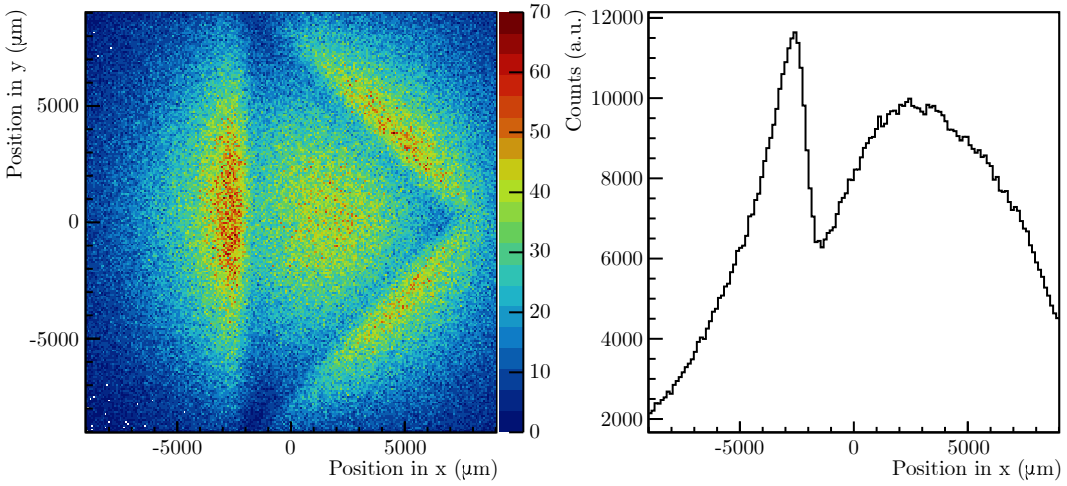

Figure 4.13: Two dimensional beam profile from MIMOSA-28 sensor (left panel), and its projection in x (right panel), for 150.14 MeV proton beam from the experimental measurements performed at MIT with the gold hammer target placed along the beam axis.

4.4.1.2 Fluence distribution

The reconstructed fluence maps were computed by following the analysis method assessed in section 3.6.4, based on all single reconstructed tracks. The fluence maps are presented in Figure 4.14 and Figure 4.15 for the bone target and the gold hammer, respectively.

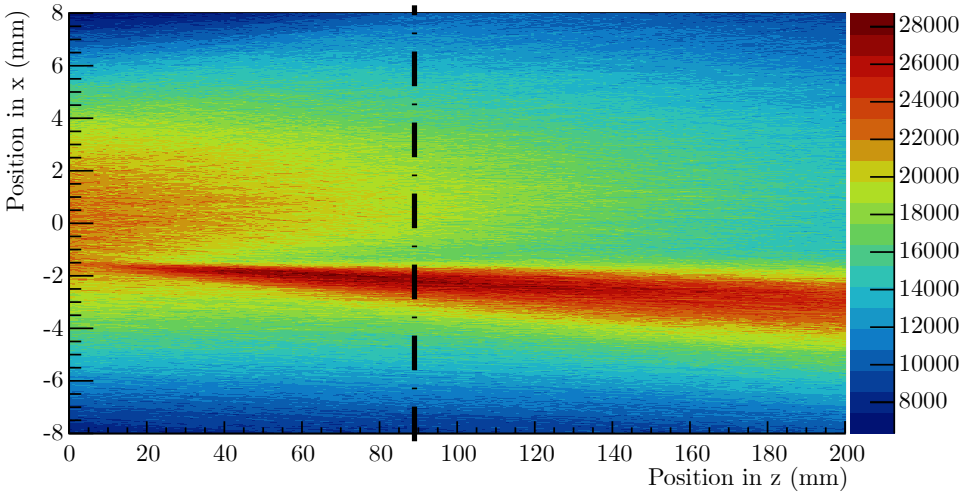

Figure 4.14: Reconstructed fluence map for 150.14 MeV proton beam passing through the bone target placed at position zero in (x,z) coordinates. The fluence map was computed from all tracks reconstructed with MIMOSA-28 sensors. The vertical dotted line shows the position of the first sensor placed behind the target.

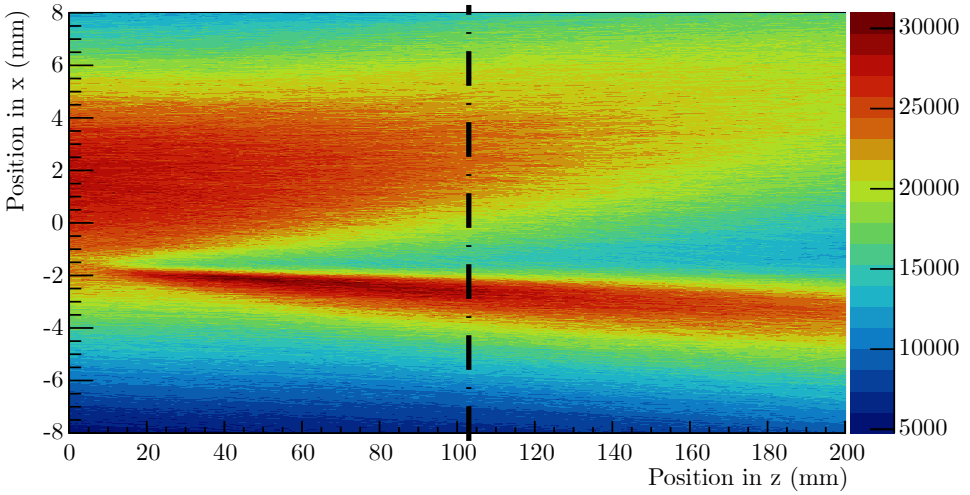

Figure 4.15: Reconstructed fluence map for 150.14 MeV proton beam passing through the gold hammer target placed at position zero in (x,z) coordinates. The fluence map was computed from all tracks reconstructed with MIMOSA-28 sensors. The vertical dotted line shows the position of the first sensor placed behind the target.

The propagation of the perturbation due to edge-scattering can be evaluated with fluence maps presented in Figures 4.14 and 4.15. Even though the thickness of the gold hammer is much smaller than the one of the bone target (see Table 3.8), the perturbations from both targets are similar along the beam axis. The strength of the perturbation can be correlated to the angular deflection, estimated by the Highland approximation (equation 1.4). Since the density of gold is around 10 times bigger than the one of cortical bone, the created perturbation of gold is much larger than from lighter materials for a given thickness.
The presented method is able to determine the propagation of the perturbation induced from edge-scattering effects. Both targets, evaluated above, produced a significant effect on the fluence since their dimensions and materials are relatively large.

4.4.2 Fiducial markers

The fiducial markers studied in this work are in use for image guidance in case of interfractional motions of the tumor during particle therapy. The markers need to follow several criteria: good visibility on X-ray projections or on CBCT images, low artifact production on the treatment planning CT, and low dose perturbations during the treatment. The latter criteria was evaluated with carbon ion beams of different energies for different small fiducial markers (e.g., 0.280 mm diameter for the gold Anchor) that were designed to produce low dose perturbations. The new measurement concept using six high resolution pixel sensors was applied to detect these small perturbations, and then compute a 3D image of the fluence reconstructed from all single tracks. With this method, the maximum perturbation from four different fiducial markers (Table 3.9) was evaluated for three energies of ^{12}C ion beams (Table 3.10).

4.4.2.1 Beam profiles: Mimosa-28 vs. radiochromic films

The beam profiles measured with Mimosa-28 and the radiochromic films were first compared without any perturbation. For this, the analysis method explained in section 3.6.3.3 was followed, and the beam profiles in x and y were computed at different positions along the z-axis. In Figure 4.16, the beam profiles in x and y are presented in front of the PE block, behind the PE block and behind the water aquarium from the CMOS measurements (S1b, S2b and S3a), superimposed with the film measurements (F1, F2 and F3), respectively (experimental setups in Figures 3.5 and 3.6). The mean value and RMS of each profile were computed after integration over a range of -8000 to $+8000$ µm, and are listed in Table 4.6. The resulting beam profile parameters, measured without any perturbation, of the radiochromic films and the Mimosa-28 sensors are in agreement. The mean value and RMS differences, in x and y, of the two experiments are smaller than 50 and 150 µm, respectively. The deviations between the two measurement methods can be explained by the different detector resolutions, and by the few months in-between the two measurements. Since the radiochromic films are used to measure the deposited dose, while Mimosa-28 sensors deliver a fluence information, the output from the two detectors differs. Even though the beam profiles measured with the pixel sensors were adjusted by applying a weighting factor, as explained in section 3.6.3.3, the correction is not precise since the energy resolution of the sensors is low.

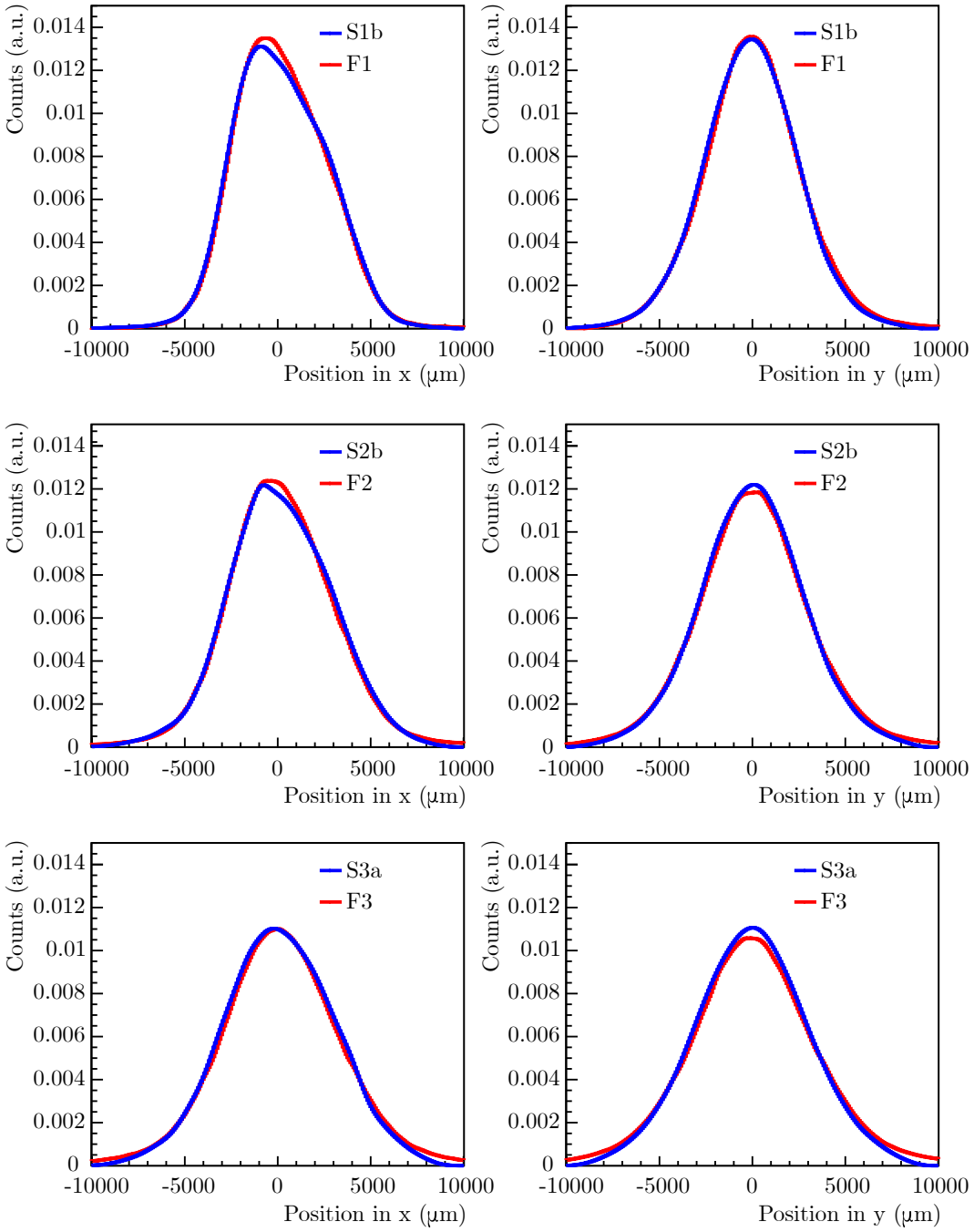

Figure 4.16: Beam profiles from MIMOSA-28 sensors and EBT3 radiochromic films irradiated with 294.97 MeV/u carbon ion beam. The left panels show the profiles in x, while the right panels show the profiles in y for the MIMOSA-28 sensors (blue line) and EBT3 radiochromic films (red line). Results at three different positions were compared: in front of the PE block with sensor S1b and film F1 (top panels), behind the PE block with sensor S2b and film F2 (middle panels), and behind the water aquarium with sensor S3a and film F3 (bottom panels).

Table 4.6: Mean and RMS values of the beam profiles in x and y from the MIMOSA-28 sensors and the radiochromic films, at equal positions along the beam axis for 294.97 MeV/u carbon ion beam.

	In front of PE		Behind PE		Behind aquarium	
	S1b	F1	S2b	F2	S3a	F3
Mean in x (µm)	181.3	188.8	172.3	156.7	104.4	157.2
RMS in x (µm)	2409	2372	2706	2674	2903	2973
Mean in y (µm)	−61.8	28.0	1.8	39.4	−41.3	1.0
RMS in y (µm)	2509	2551	2753	2837	2968	3090

As observed in Figure 4.16, the deviation increases behind the PE block and the water aquarium. The production of lighter fragments increases through these layers, and the resulting field becomes more complex, which also enlarges the deviation between the two measurement methods. In addition, the produced light fragments, such as protons, are emitted at larger angles than the heavier ones and deposit less energy. Therefore, the tail of the beam profiles from the film measurements is smaller than the one from the CMOS sensors before applying a correction factor. With the latter measurement concept, the deposited energy from the particles passing through the detectors and their charge can be correlated to the cluster size, as studied in section 4.2.1.2. Due to the digital output of the MIMOSA-28 [9], it is not possible to separate the different produced fragments clearly. However, the primary ^{12}C ions could be distinguished from the lighter fragments due to its well defined cluster size.
In the second part, the beam profiles from the MIMOSA-28 were benchmarked against the radiochromic film measurements when the particle beam suffers perturbations due to fiducial markers. The analysis method described in section 3.6.3.3 was followed again, where the length of the integrated area along the y-axis was 8 mm for the Gold Anchor #1 and the Visicoil markers, and 2.5 mm for the Gold Anchor #2 and the carbon-coated ZrO_2 markers. The selected area for the data analysis was identical for both experiments. Since the perturbation is determined compared to the beam profiles without any perturbation, the latter profiles were also analyzed by selecting the same area.
In Figure 4.17, the beam profiles from the sensor S3a and the film F3 with the Gold Anchor #1 are presented. The observed perturbation induced by this marker shows a cold spot of 2.4% from the MIMOSA-28 sensor and 2.5% from the radiochromic film, for measurements performed with 294.97 MeV/u ^{12}C ions.
The results obtained from both measurement techniques are in good agreement with and without a fiducial marker placed inside the water aquarium. Therefore, the new measurement concept with the use of high resolution tracker for the determination of fluence perturbations induced by fiducial markers is validated.

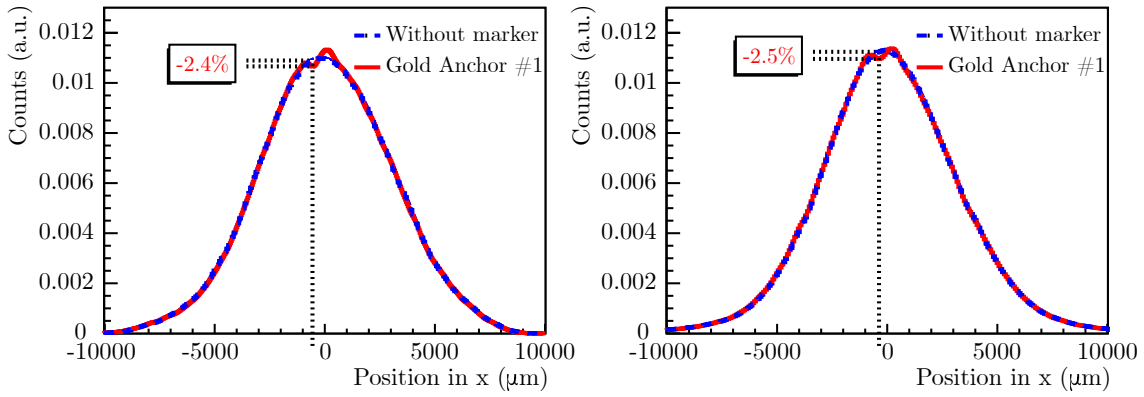

Figure 4.17: Experimental measurements of the beam profiles in x for 294.97 MeV/u carbon ion beam taken from MIMOSA-28 sensor S3a (left panel) and EBT3 radiochromic film F3 (right panel). The perturbation induced by the Gold Anchor #1 placed inside the aquarium (red line) is compared to the system without any perturbation (dashed blue line).

4.4.2.2 Fluence perturbation from MIMOSA-28 sensor measurements

Since the fluence perturbation from the fiducial markers is induced by multiple Coulomb scattering, the perturbation varies along the beam axis. A maximum cold spot is present at a certain position z, which is difficult to precisely predict before the analysis of the experimental data.
In this section, the results of the maximum perturbation due to the fiducial markers are computed from the fluence map of all reconstructed tracks, as explained in section 3.6.4. The fluence maps were integrated over a determined area as for the analysis in section 4.4.2.1. To determine the maximum cold spot, the beam profile with the marker was compared to the beam profile without marker for the same integrated area at the same position along the beam axis. In Figures 4.18, 4.19 and 4.20, the fluence maps and the corresponding beam profiles for the maximum induced cold spots are shown for the Gold Anchor #1, the Visicoil and the carbon-coated ZrO_2 fiducial markers, for every carbon ion beam listed in Table 3.10. The zero positions in x and z are the coordinates of the fiducial marker position.
A summary of the maximum cold spot values from the fiducial markers and their corresponding position along the beam axis are listed in Table 4.7. The uncertainties on the maximum cold spot values were calculated as the quadratic sum of the uncertainty on the beam profiles, with and without marker. The relative uncertainty on a single beam profile was calculated as a function of the integrated entries at the position x, where the maximum cold spot was determined. The uncertainty on the position z, where the maximum cold spot is present, was considered as 3 mm, comprising the uncertainty of the sensor positioning and the uncertainty on the reconstructed track.

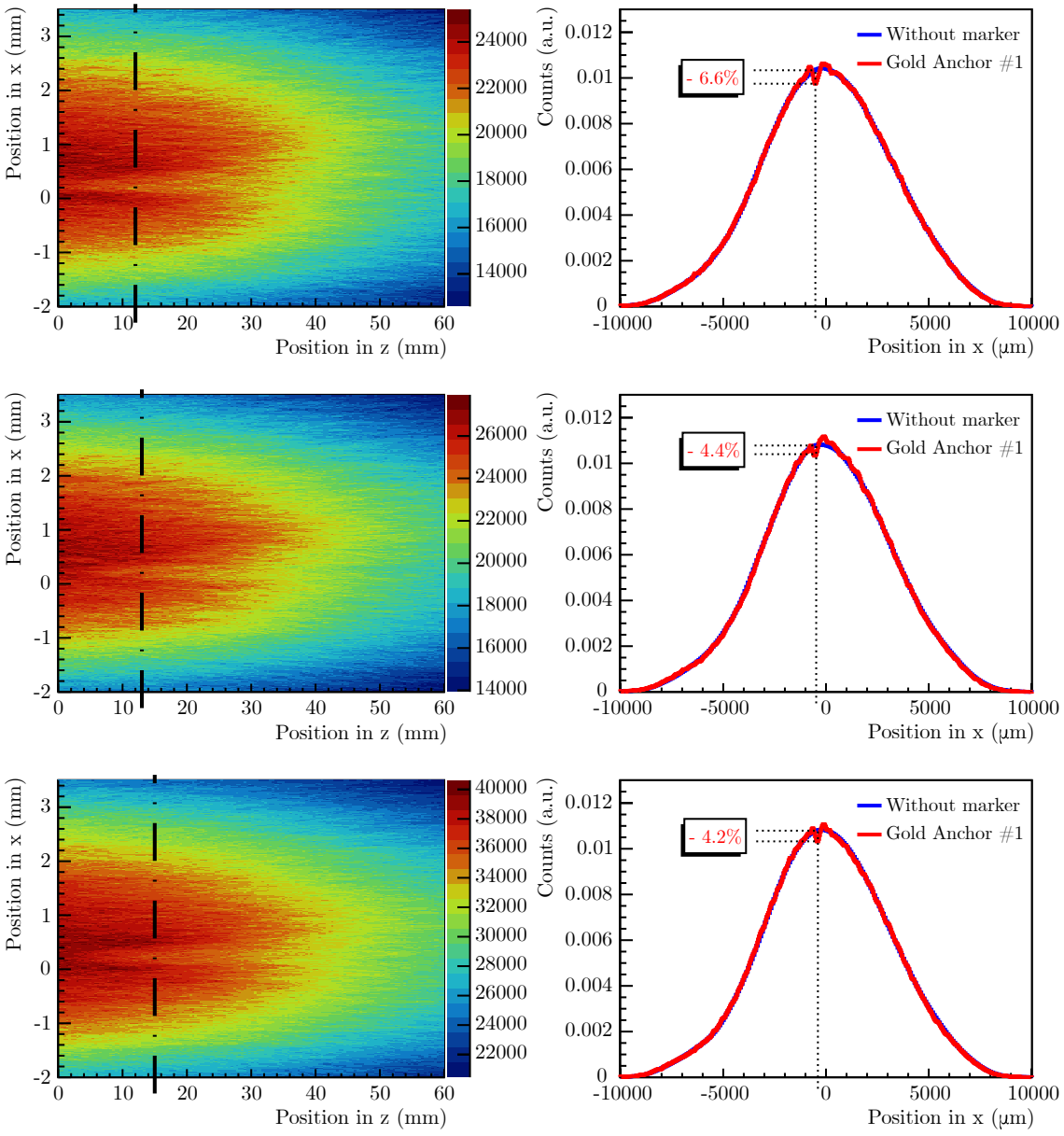

Figure 4.18: Reconstructed fluence maps and beam profiles of carbon ions at three different energies through the Gold Anchor #1 marker placed at position zero in (x,z) coordinates. The left panels show the fluence maps reconstructed from all tracks, and the right panels show their corresponding profile at the position z, where the perturbation is maximum for 278.84 (top panels), 294.97 (middle panels) and 310.61 MeV/u (bottom panels) carbon ion beams from the experimental measurements. The black vertical dash-dotted line on the fluence map represents the corresponding position along the beam axis where the cold spot is maximum. In the right panels, the red line shows the profile at this position when the marker is placed inside the water aquarium, while the blue line shows the profile when there is no perturbation for the same position z. In the same panels, the vertical dotted line indicates the position in x of the maximum perturbation, while the dotted horizontal lines quantify the cold spot from the profiles with and without perturbation at this position.

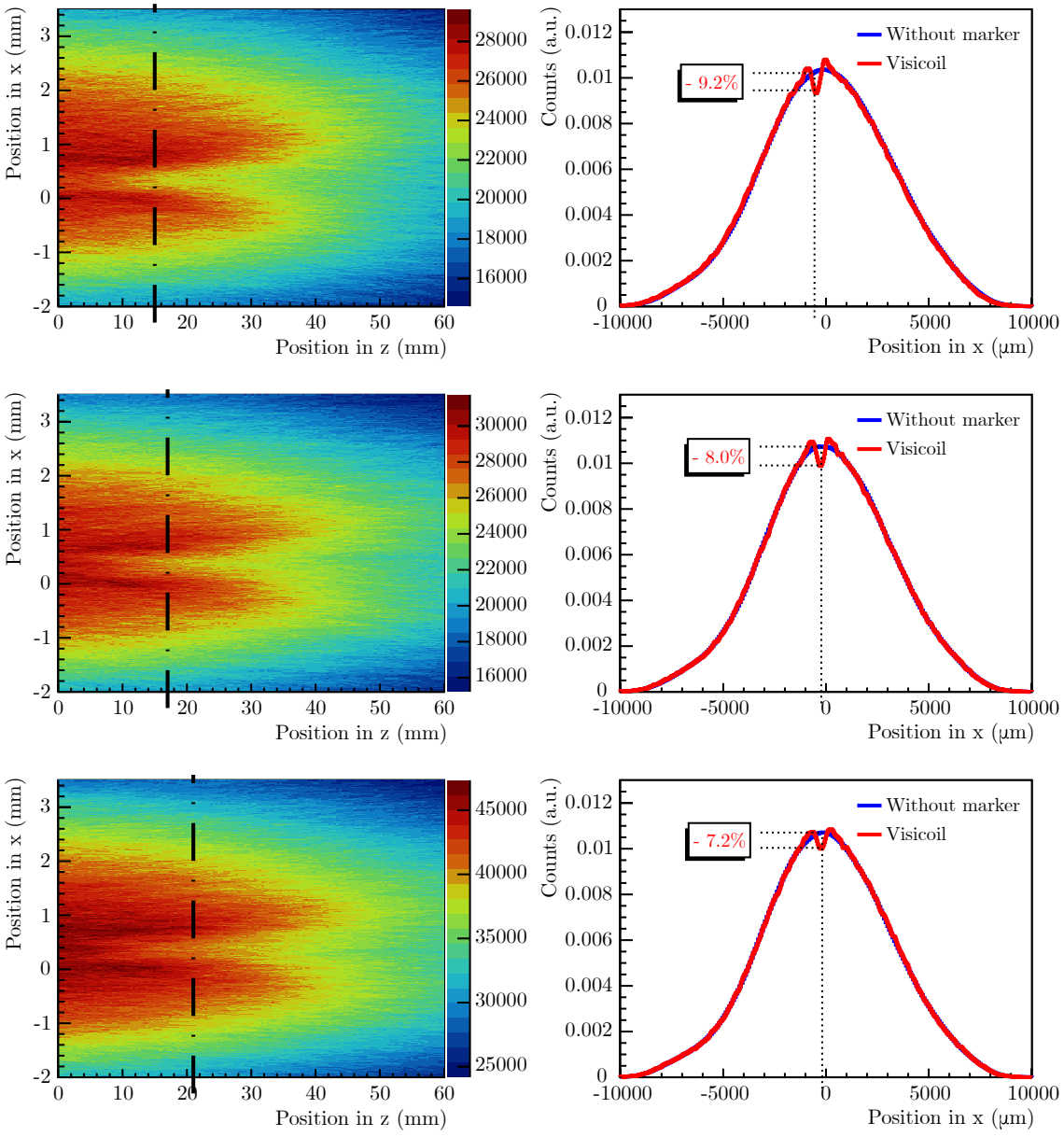

Figure 4.19: Reconstructed fluence maps and beam profiles of carbon ions at three different energies through the Visicoil marker placed at position zero in (x,z) coordinates. The panels description is the same as Figure 4.18.

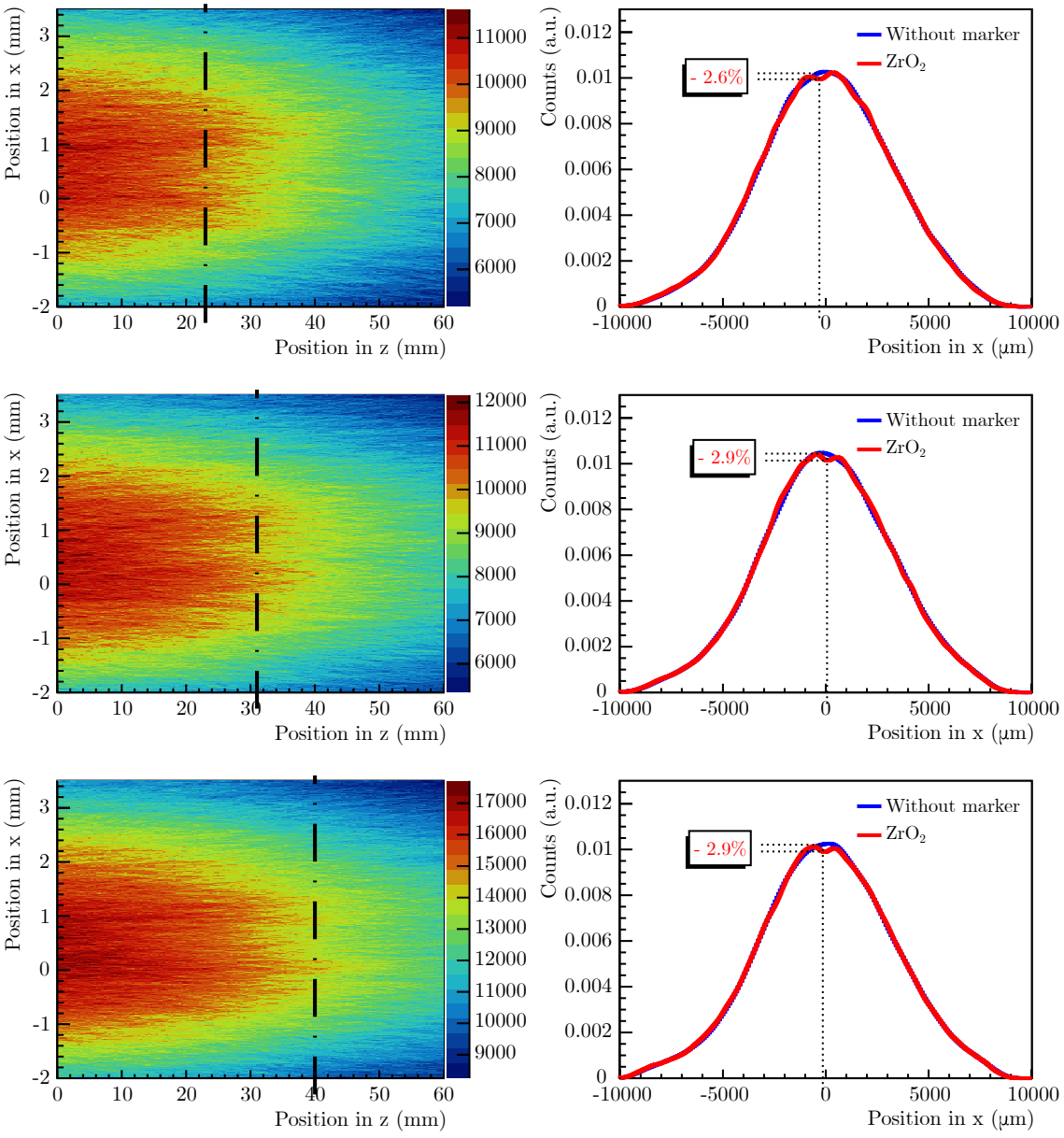

Figure 4.20: Reconstructed fluence maps and beam profiles of carbon ions at three different energies through the carbon-coated ZrO_2 marker placed at position zero in (x,z) coordinates. The panels description is the same as Figure 4.18.

Table 4.7: Summary of the cold spot values where the perturbation is maximum, and its position along the z-axis for the different fiducial markers measured with MIMOSA-28 sensors for carbon ions at three different energies.

	Maximum cold spot (%)			Position in z (mm)		
Energy (MeV/u)	ZrO_2	Gold Anchor #1	Visicoil	ZrO_2	Gold Anchor #1	Visicoil
278.84	2.8 ± 0.7	6.6 ± 0.4	9.2 ± 0.4	23 ± 3	12 ± 3	15 ± 3
294.97	2.9 ± 0.7	4.4 ± 0.4	8.0 ± 0.4	31 ± 3	13 ± 3	17 ± 3
310.61	2.9 ± 0.6	4.2 ± 0.4	7.2 ± 0.4	40 ± 3	15 ± 3	21 ± 3

The integration range in y-direction was varied to benchmark the robustness of the chosen window. The results obtained with the different integration ranges showed a good agreement. The values from Table 4.7 demonstrate that the maximum cold spots and their position in z vary as a function of the marker type, and the primary beam energy. The smaller the energy is, the stronger is the effect induced by the marker on the particle beam. Fiducial markers with high density and high atomic number create stronger and larger cold spots.
In this work, the Gold Anchor #2, described in Table 3.9, was also analyzed. In Figure 4.21, the fluence map and the beam profile at the maximum cold spot position is shown for 310.61 MeV/u carbon ions. The cold spot created by the Gold Anchor #2 is observed to be about 4.4%. However, the precise quantification of the cold spot induced by this fiducial marker was not possible, due to a lack of statistics and its more complex shape. The integrated area selected for this folded marker was relatively small compared to the Gold Anchor #1.

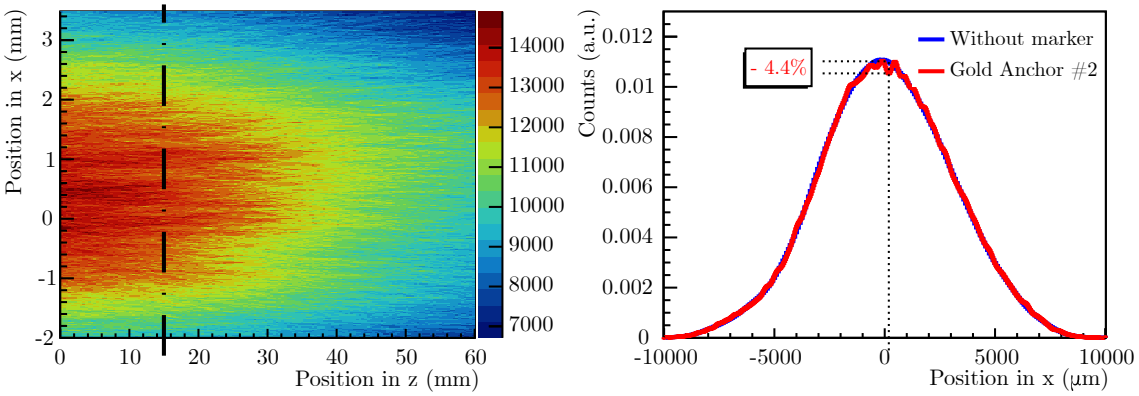

Figure 4.21: Reconstructed fluence map and beam profile for 310.61 MeV/u carbon ion beam through the Gold Anchor #2 marker placed at position zero in (x,z) coordinates. The panels description is the same as Figure 4.18.

The previous results show that the new measurement concept for evaluating fluence perturbations due to fiducial markers could be successfully applied to evaluate the resulting cold spots. The hot spots were not reported in this work even though they can also be identified. In general, a slight overdosage in a small part of the target volume is considered much less critical than a local underdosage that can potentially cause a recurrence of the tumor. A good rule of thumb is that the magnitude of the two hot spots is roughly 50% of the enclosed cold spot, as observed in Figures 4.18–4.20. However, this also depends on the orientation of the marker compared to the primary beam. It is important to note that, for all measurements, the beam profile was integrated, and the total area of the profiles with and without markers was found to be the same. The cold spot increases with the density and the atomic number of the marker material. The maximum cold spot created along the beam axis and its position differ for all markers since it depends on several factors such as the density, the orientation and the thickness of the marker. The beam energy also influences the perturbation since multiple Coulomb scattering depends on the projectile energy. All markers were measured in vertical position and the Gold Anchor was also measured when folded. This study shows that the Viscoil marker, which has a diameter of 0.5 mm, induces a stronger fluence perturbation than the Gold Anchor #1 of 0.28 mm diameter. The carbon-coated ZrO_2 is thicker, but induces less perturbation since it is less dense. The maximum cold spots, measured in this work for a 278.84 MeV/u carbon ion beam, were about 6.6 and 9.2% for the Gold Anchor #1 and the Viscoil, and their position downstream of the fiducial marker were 13 and 15 mm, respectively. For the carbon-coated ZrO_2 marker, the perturbation was found to be $< 3\%$ for all energies. Therefore, it could be a good candidate for image guidance during carbon ion therapy treatments. However, since it has a lower density than gold markers, it can be difficult to see it on X-ray projections. For instance, at HIT in Germany, the Gold Anchor is used for proton therapy treatments of prostate cancer. In contrast to the gold markers, the carbon-coated ZrO_2 marker is not visible on the daily X-ray imaging at HIT.

The measurements presented in this work were performed with a setup where the pixel sensors were placed in a short distance behind the water aquarium (see Figure 3.5). In general, the distance of the cold spot is larger for markers that induce smaller scattering angles, and the magnitude is then smaller. Therefore, the maximum cold spots for the ZrO_2 marker appear behind the water aquarium (compare Table 4.7 and Figure 3.5). The water equivalent path length of the sensors and the air gaps in-between were estimated to be < 1 mm in total, which has little influence on the results. If the air gap in front of the sensor would be replaced by water, the magnitude of the cold spot would be slightly but not significantly suppressed, and its distance from the marker would also decrease slightly. For the Gold Anchor and the Visicoil markers, the positions of the cold spots were found to be inside the water aquarium, and therefore, would not be different if the water aquarium would be larger.

The cold spots, evaluated with radiochromic films in previous studies for protons [87, 88], were bigger than the ones found in this work. This was expected since the multiple Coulomb scattering of protons is stronger than for ^{12}C ions. In addition, the gold markers investigated by Cheung et al. (2010) [87] had a diameter of 0.8 mm, which is bigger compared to the ones studied in this work, with a maximum diameter of 0.5 mm.

For the film measurements, the beam intensities are generally in the order of 10^7–10^8 particles/s, which means that after some seconds, a measurement is done. In the case of the MIMOSA-28 sensors, the beam intensity needs to be decreased to 10^3–10^4 particles/s to avoid pile-up in the detectors, leading to longer measurement times. Each measurement took about 1 hour, and the low particle rates can lead in some cases to a lack of statistics. For instance, precisely quantifying the cold spot of the Gold Anchor #2, which has a complex geometry and a smaller integrated area, was difficult within the measurement time. However, as shown in Figure 4.21, the structure of this fiducial marker creates several cold spots.

As investigated in this work, the perturbation is more important for lower energy beams since the scattering is stronger. The absorbed dose is proportional to the fluence and the LET. The latter varies along the particle path and is higher for low energies. This implies that the dose perturbation is stronger if the created cold spot appears to be in the Bragg peak region. For heavy ions (e.g., carbon ions), fragments of lower Z than the primary beam are produced, forming a fragmentation tail behind the Bragg peak. These fragments are also scattered by the markers, and contribute to the dose perturbation. However, they do not have a major impact compared to the primary ions.

The perturbations in this work were measured with markers positioned in a perpendicular orientation with respect to the beam axis, and showed cold spots ranging from less than 3% up to 9%. As studied by Newhauser et al. (2007) [84], the orientation of the marker has an impact on the dose perturbation. The magnitude of the perturbation is stronger for a parallel orientation of the marker with respect to the beam axis, resulting in a larger thickness of the scattering material. On the other hand, the volume of the perturbation becomes smaller. Within the available beam time of the presented measurement campaign, the work was focused more likely where the markers are not parallel to the beam. In a future work, the effect of different marker orientations could also be examined with the presented setup. From a clinical point of view, perturbations should be considered if the markers, used for image guidance, have a high atomic number and a diameter > 0.5 mm. However, for a clear statement about the clinical impact, it is necessary to include all parameters contributing to the dose perturbations. They depend on the type of markers used, their position inside the tumor, the type of particle and its energy, as well as the irradiation fields used for the patient treatment. In addition, it is very difficult to assess the clinical impact of the dose perturbations that also depends on complicated tissue effects, and is highly patient specific. However, there is a potential risk from the cold spots for a locale recurrence of the tumor. Therefore, it was one goal of this work to quantify and compare the effect on the dose for different markers in a sense that there is less or more risk.

It is also important to note that the perturbations measured in this work are due to an edge-scattering effect from the markers, and not to a range shift from different stopping powers. The hot spots were not investigated in this study, but could be measured as well as their position in order to verify that they are not produced inside healthy tissues, such as organs at risk. In a future work, the setup could be improved where the sensors would be placed inside the water aquarium, and using a scanned beam to have a homogeneous field instead of a Gaussian beam spot.

Conclusions & Outlook

The aim of this PhD thesis was to optimize and test measurement methods for ion-beam therapy applications, using CMOS pixel sensors. For this, Mimosa-28 sensors, which are high spatial resolution pixel detectors, were implemented in a series of several setups and experiments at different accelerator facilities.

In order to perform high precision measurements with Mimosa-28 sensors, mechanical accuracy and robustness of the setup are necessary. In this work, the setup was mechanically improved by placing each sensor proximity board in a robust holder, designed with CATIA V5, for a precise fitting. The experimental setup was also optimized by fitting several electronics boards inside a 19-inch rack drawer with all cables and interconnections, ameliorating the handling of the experimental setup and reducing the setup time. For a proper stability during the experiments, the sensors were attached to an optical bench, and all cables are clamped to avoid any sensor movement due to the cable strain. The changes to the experimental setup were successfully implemented and used for all experiments, demonstrating the good mechanical properties achieved in this work, and enabling a mobile setup that can be easily transported to different accelerator facilities.

Additionally, the sensor alignment is a crucial step in order to reach the micrometer precision of the sensors. With such purpose, an alignment procedure was developed, in the frame of this work, to correct the mechanical misalignment of a set of sensors placed along the beam axis. The procedure is based on a global χ^2 minimization and matrix operations for all events at the same time. Its performance was evaluated with simulated and experimental data, resulting in uncertainties < 3 µm for the translations and $< 0.1°$ for the rotation. This alignment procedure was used for all experimental data recorded during this work, and demonstrated its low time consumption and its reliability with a proper convergence, leading to a spatial resolution better than 10 µm on the reconstructed tracks. The new alignment procedure can be used for all linear CMOS tracker with an efficient, easy-to-implement and robust algorithm.

Since the response of the Mimosa-28 sensor to different ion species was not fully understood, the characterization of Mimosa-28 was performed by evaluating the response of the sensor, defined as the cluster size, against different particle species and energies. The study of two sensor generations showed the improved results of the second generation due to electronics upgrade of the sensor, resulting in a more homogeneous noise repartition over the full sensor area. This generation was then evaluated with different particle species and energies, demonstrating an energy loss dependence from the cluster size. Further tests

would be required to completely characterize the sensor performance, such as noise threshold scan and recording data with other ion species and energies than the ones used. The data collected in this work can be used for the FOOT experiment [121] that integrates several MIMOSA-28 sensors, and for the STRONG project that intends to develop an analog sensor based on the characteristics of MIMOSA-28.

In order to exploit the MIMOSA-28 sensors for characterization of beam envelope at low intensities, the profiles of therapeutic particle beams were measured for different ion beams in several facilities. The position and width of the beam were extracted from the Gaussian fit of the beam profiles. By placing a set of sensors along the beam axis, the lateral beam spread along the longitudinal axis, was determined with the transport code SCATTMAN. With this method, the initial ion optical parameters of the beam were extracted, and the beam width at any position along the beam axis could be determined. An online tool for beam monitoring was also developed in order to obtain the beam information for experiments requiring low beam intensities. This tool was successfully used during several experiments to adjust the beam as needed, and can also be used in the future for various experiments to monitor the profiles of particle beams at low intensity.

The MIMOSA-28 was also successfully used for the evaluation of fluence perturbations due to edge-scattering effects induced by fiducial markers that were evaluated with a new measurement method, using a set of MIMOSA-28 sensors. The 3D fluence distributions were computed with all reconstructed tracks, and the propagation of the perturbation along the beam axis was established after calculating the 2D fluence maps. The fluence perturbations were then quantified for several small fiducial markers, used in ion-beam therapy for patient positioning verification in case of interfractional motions of the tumor. The studied markers were composed of different materials and had different geometries. The maximum cold spots, created behind the fiducial markers, were quantified as well as their longitudinal position after computing the 2D fluence maps. This measurement method was validated against the standard measurement method, using radiochromic films. The measurements showed that the fluence perturbations due to edge-scattering effects can be significantly reduced when low density and low atomic number materials are used, such as the carbon-coated ZrO_2 marker instead of the gold ones. Therefore, such markers should be preferred for carbon ion treatments if the imaging method used for positioning can recognize them. With the use of a tracker system, the maximum cold spots from fiducial markers could be determined without knowing their position along the beam axis in advance, which makes this measurement concept superior compared to radiochromic films. The measurement of fluence perturbations with this new method should also be done for other therapy beams, especially for light ions such as protons or helium ions since they scatter differently compared to carbon beams. Additionally, the experimental data from this study can be useful for the benchmarking of Monte Carlo codes or other dose calculation algorithms.

In a future work, MIMOSA-28 could be used to detect strong gradients edges for monitoring intrafractional motions of a tumor during ion-beam therapy. The vertex distributions can be reconstructed to verify the treatment delivery in the case of moving targets. Preliminary tests have been performed at GSI, with the detection of prompt particles, showing promising results.

Bibliography

[1] J. Ferlay, et al. Estimating the global cancer incidence and mortality in 2018: GLOBOCAN sources and methods. *Int. J. Cancer*, 144(8):1941–1953, 2019. doi: 10.1002/ijc.31937.

[2] M. Durante and S. Formenti. Harnessing radiation to improve immunotherapy: better with particles? *Br. J. Radiol.*, 93(1107):20190224, 2020. doi: 10.1259/bjr.20190224.

[3] M. Durante and J. S. Loeffler. Charged particles in radiation oncology. *Nat. Rev. Clin. Oncol.*, 7(1):37, 2010. doi: 10.1038/nrclinonc.2009.183.

[4] M. Durante, R. Orecchia, and J. S. Loeffler. Charged-particle therapy in cancer: clinical uses and future perspectives. *Nat. Rev. Clin. Oncol.*, 14(8):483, 2017. doi: 10.1038/nrclinonc.2017.30.

[5] D. Schardt, T. Elsässer, and D. Schulz-Ertner. Heavy-ion tumor therapy: Physical and radiobiological benefits. *Rev. Mod. Phys.*, 82(1):383, 2010. doi: 10.1103/RevModPhys.82.383.

[6] R. Turchetta, et al. CMOS Monolithic Active Pixel Sensors (MAPS): New 'eyes' for science. *Nucl. Instrum. Meth. A*, 560(1):139 – 142, 2006. ISSN 0168-9002. doi: 10.1016/j.nima.2005.11.241. Proceedings of the 13th International Workshop on Vertex Detectors.

[7] I. Valin, et al. A reticle size CMOS pixel sensor dedicated to the STAR HFT. *J. Instrum.*, 7(01):C01102, 2012. doi: 10.1088/1748-0221/7/01/C01102.

[8] C. Finck, et al. Study for online range monitoring with the interaction vertex imaging method. *Phys. Med. Biol.*, 62(24):9220, 2017. doi: 10.1088/1361-6560/aa954e.

[9] E. Spiriti, et al. CMOS active pixel sensors response to low energy light ions. *Nucl. Instrum. Meth. A*, 875:35–40, 2017. doi: 10.1016/j.nima.2017.08.058.

[10] U. Weber. *Volumenkonforme Bestrahlung mit Kohlenstoff-Ionen zur Vorbereitung einer Strahlentherapie*. PhD thesis, Universität Kassel, 1996.

[11] W. C. Röntgen. Über eine neue Art von Strahlen. *Sitzungsber. Physikal. Med. Gesellsch. Würzburg*, 9:132–141, 1895.

[12] A. H. Becquerel. Sur les radiations invisibles émises par les corps phosphorescents. *CR Acad. Sci. Paris*, 122:501, 1896.

[13] P. Curie. Radioactive substances, especially radium. *Nobel lecture*, 6, 1905.

[14] M. Lederman. The early history of radiotherapy: 1895–1939. *Int. J. Radiat. Oncol. Biol. Phys.*, 7(5):639–648, 1981. doi: 10.1016/0360-3016(81)90379-5.

[15] H. S. Kaplan. Basic principles in radiation oncology. *Cancer*, 39(S2):689–693, 1977. doi: 10.1002/1097-0142(197702)39:2+<689::AID-CNCR2820390702>3.0.CO;2-W.

[16] W. D. Coolidge. A powerful Röntgen ray tube with a pure electron discharge. *Phys. Rev.*, 2(6):409, 1913. doi: 10.1103/PhysRev.2.409.

[17] R. F. Robison. The Race For Megavoltage X-Rays Versus Telegamma. *Acta Oncol.*, 34(8):1055–1074, 1995. doi: 10.3109/02841869509127233.

[18] R. J. Van de Graaff, K. T. Compton, and L. C. Van Atta. The Electrostatic Production of High Voltage for Nuclear Investigations. *Phys. Rev.*, 43:149–157, Feb 1933. doi: 10.1103/PhysRev.43.149.

[19] E. O. Lawrence and M. S. Livingston. The production of high speed light ions without the use of high voltages. *Phys. Rev.*, 40(1):19, 1932. doi: 10.1103/PhysRev.40.19.

[20] J. Chadwick. Possible existence of a neutron. *Nature*, 129(3252):312–312, 1932. doi: 10.1038/129312a0.

[21] D. W. Kerst. The acceleration of electrons by magnetic induction. *Phys. Rev.*, 60 (1):47, 1941. doi: 10.1103/PhysRev.60.47.

[22] E. M. McMillan. The synchrotron–a proposed high energy particle accelerator. *Phys. Rev.*, 68(5-6):143, 1945. doi: 10.1103/PhysRev.68.143.

[23] H. Johns, et al. 1,000-Curie Cobalt-60 units for radiation therapy. *Nature*, 168(4285): 1035–1036, 1951. doi: 10.1038/1681035a0.

[24] C. Karzmark and N. C. Pering. Electron linear accelerators for radiation therapy: history, principles and contemporary developments. *Phys. Med. Biol.*, 18(3):321, 1973. doi: 10.1088/0031-9155/18/3/001.

[25] A. Brahme, J.-E. Roos, and I. Lax. Solution of an integral equation encountered in rotation therapy. *Phys. Med. Biol.*, 27(10):1221, 1982. doi: 10.1088/0031-9155/27/10/002.

[26] E. Courant. Early Milestones in the Evolution of Accelerators. In *Reviews Of Accelerator Science And Technology: Volume 1*, pages 1–5. World Scientific, 2008.

[27] R. R. Wilson. Radiological use of fast protons. *Radiology*, 47(5):487–491, 1946. doi: 10.1148/47.5.487.

[28] C. Tobias and P. Todd. Heavy charged particles in cancer therapy. *Nat. Cancer Inst. Monogr.*, (24):1–21, 1 1967.

[29] G. Chen, J. Castro, and J. Quivey. Heavy charged particle radiotherapy. *Ann. Rev. Biophys. Bioeng.*, 10(1):499–529, 1981. doi: 10.1146/annurev.bb.10.060181.002435.

[30] W. Chu, B. Ludewigt, and T. Renner. Instrumentation for treatment of cancer using proton and light-ion beams. *Rev. Sci. Instrum.*, 64(8):2055–2122, 1993. doi: 10.1063/1.1143946.

[31] M. L. Boone, et al. Introduction to the use of protons and heavy ions in radiation therapy: Historical perspective. *Int. J. Radiat. Oncol. Biol. Phys.*, 3:65–69, 1977. doi: 10.1016/0360-3016(77)90229-2.

[32] M. Goitein, et al. Planning treatment with heavy charged particles. *Int. J. Radiat. Oncol. Biol. Phys.*, 8(12):2065–2070, 1982. doi: 10.1016/0360-3016(82)90546-6.

[33] L. J. Verhey, M. Goitein, P. McNulty, J. E. Munzenrider, and H. D. Suit. Precise positioning of patients for radiation therapy. *Int. J. Radiat. Oncol. Biol. Phys.*, 8(2): 289–294, 1982. doi: 10.1016/0360-3016(82)90530-2.

[34] Y. Hirao, et al. Heavy ion synchrotron for medical use—HIMAC project at NIRS-Japan—. *Nucl. Phys. A*, 538:541–550, 1992. doi: 10.1016/0375-9474(92)90803-R.

[35] E. Pedroni, et al. The 200-MeV proton therapy project at the Paul Scherrer Institute: Conceptual design and practical realization. *Med. Phys.*, 22(1):37–53, 1995. doi: 10.1118/1.597522.

[36] T. Haberer, W. Becher, D. Schardt, and G. Kraft. Magnetic scanning system for heavy ion therapy. *Nucl. Instrum. Meth. A*, 330(1-2):296–305, 1993. doi: 10.1016/0168-9002(93)91335-K.

[37] M. Krämer, et al. Treatment planning for heavy-ion radiotherapy: physical beam model and dose optimization. *Phys. Med. Biol.*, 45(11):3299, 2000. doi: 10.1088/0031-9155/45/11/313.

[38] M. Scholz and G. Kraft. Calculation of Heavy Ion Inactivation Probabilities Based on Track Structure, X Ray Sensitivity and Target Size. *Radiat. Prot. Dosim.*, 52 (1–4):29–33, 1994. doi: 10.1093/oxfordjournals.rpd.a082156.

[39] K. Parodi, et al. PET imaging for treatment verification of ion therapy: Implementation and experience at GSI Darmstadt and MGH Boston. *Nucl. Instrum. Meth. A*, 591(1):282–286, 2008. doi: 10.1016/j.nima.2008.03.075.

[40] D. Sheikh-Bagheri and D. Rogers. Monte Carlo calculation of nine megavoltage photon beam spectra using the BEAM code. *Med. Phys.*, 29(3):391–402, 2002. doi: 10.1118/1.1445413.

[41] G. Battistoni, et al. The FLUKA Code: An Accurate Simulation Tool for Particle Therapy. *Front. Oncol.*, 6:116, 2016. ISSN 2234-943X. doi: 10.3389/fonc.2016.00116.

[42] W. D. Newhauser and R. Zhang. The physics of proton therapy. *Phys. Med. Biol.*, 60(8):R155, 2015. doi: 10.1088/0031-9155/60/8/R155.

[43] R. Serber. Nuclear reactions at high energies. *Phys. Rev.*, 72(11):1114, 1947. doi: 10.1103/PhysRev.72.1114.

[44] J.-J. Gaimard and K.-H. Schmidt. A reexamination of the abrasion-ablation model for the description of the nuclear fragmentation reaction. *Nucl. Phys. A*, 531(3-4): 709–745, 1991. doi: 10.1016/0375-9474(91)90748-U.

[45] F. A. Cucinotta, L. W. Townsend, and J. W. Wilson. Description of alpha-nucleus interaction cross sections for cosmic ray shielding studies. Technical report, NASA Langley Research Center, 1993.

[46] H. Bethe. Zur Theorie des Durchgangs schneller Korpuskularstrahlen durch Materie. *Ann. Phys.*, 397(3):325–400, 1930. doi: 10.1002/andp.19303970303.

[47] F. Bloch. Zur Bremsung rasch bewegter Teilchen beim Durchgang durch Materie. *Ann. Phys.*, 408(3):285–320, 1933. doi: 10.1002/andp.19334080303.

[48] J. Herault, et al. Stopping powers of gases for heavy ions (O, Ar, Kr, Xe) at intermediate energy (20–100 MeV/u). Vanishing of the gas–solid effect. *Nucl. Instrum. Meth. B*, 61(2):156–166, 1991. doi: 10.1016/0168-583X(91)95455-M.

[49] W. H. Barkas. *Nuclear research emulsions. Vol. 1: Techniques and theory.* Pure and Applied Physics, 1963.

[50] O. Tarasov and D. Bazin. LISE++: Radioactive beam production with in-flight separators. *Nucl. Instrum. Meth. B*, 266(19-20):4657–4664, 2008. doi: 10.1016/j.nimb.2008.05.110.

[51] J. Ashley, C. Tung, and R. Ritchie. Inelastic Interactions of Electrons with Polystyrene: Calculations of Mean Free Paths, Stopping Powers, and CSDA Ranges. *IEEE Trans. Nucl. Sci.*, 25(6):1566–1570, 1978. doi: 10.1109/TNS.1978.4329573.

[52] G. Molière. Theorie der Streuung schneller geladener Teilchen II Mehrfach-und Vielfachstreuung. *Z. Naturforsch. A*, 3(2):78–97, 1948. doi: 10.1515/zna-1948-0203.

[53] V. L. Highland. Some practical remarks on multiple scattering. *Nucl. Instrum. Meth.*, 129(2):497 – 499, 1975. ISSN 0029-554X. doi: https://doi.org/10.1016/0029-554X(75)90743-0.

[54] Highland. Erratum. *Nucl. Instrum. Meth.*, 161(1):171, 1979. ISSN 0029-554X. doi: https://doi.org/10.1016/0029-554X(79)90379-3.

[55] W. R. Leo. *Techniques for nuclear and particle physics experiments: a How-to Approach.* Springer Science & Business Media, 1994.

[56] H. Bradt and B. Peters. The heavy nuclei of the primary cosmic radiation. *Phys. Rev.*, 77(1):54, 1950. doi: 10.1103/PhysRev.77.54.

[57] L. Townsend and J. Wilson. Energy-dependent parameterization of heavy-ion absorption cross sections. *Radiat. Res.*, 106(3):283–287, 1986. doi: 10.2307/3576735.

[58] J. Dudouet, et al. Double-differential fragmentation cross-section measurements of 95 MeV/nucleon ^{12}C beams on thin targets for hadron therapy. *Phys. Rev. C*, 88(2): 024606, 2013. doi: 10.1103/PhysRevC.88.024606.

[59] F. Horst, C. Schuy, U. Weber, K.-T. Brinkmann, and K. Zink. Measurement of charge-and mass-changing cross sections for ^{4}He + ^{12}C collisions in the energy range 80–220 MeV/u for applications in ion beam therapy. *Phys. Rev. C*, 96(2):024624, 2017. doi: 10.1103/PhysRevC.96.024624.

[60] E. Haettner, H. Iwase, and D. Schardt. Experimental fragmentation studies with ^{12}C therapy beams. *Radiat. Prot. Dosim.*, 122(1-4):485–487, 2006. doi: 10.1093/rpd/ncl402.

[61] E. Haettner, H. Iwase, M. Krämer, G. Kraft, and D. Schardt. Experimental study of nuclear fragmentation of 200 and 400 MeV/u ^{12}C ions in water for applications in particle therapy. *Phys. Med. Biol.*, 58(23):8265, 2013. doi: 10.1088/0031-9155/58/23/8265.

[62] ICRU. Quantities and units in radiation protection dosimetry. *Report 51, International Commission on Radiation Units and Measurements, Washington DC*, 1993. doi: 10.1093/jicru/os26.2.Report51.

[63] ICRU. Linear Energy Transfer. *Report 16, International Commission on Radiation Units and Measurements, Washington DC*, 1970. doi: 10.1093/jicru/os9.1.Report16.

[64] A. Wambersie. The future of high-let radiation in cancer therapy. justification of the heavy-ion therapy programmes. Technical report, International Atomic Energy Agency (IAEA), 1989.

[65] B. Alberts. *Molecular Biology of the Cell.* CRC Press, 2017. ISBN 9781317563754.

[66] E. J. Hall and A. J. Giaccia. *Radiobiology for the Radiologist*, volume 6. Lippincott Williams & Wilkins, 2006.

[67] M. Krämer and G. Kraft. Calculations of heavy-ion track structure. *Radiat. Environ. Biophys.*, 33(2):91–109, 1994. doi: 10.1007/BF01219334.

[68] G. Kraft, M. Scholz, and U. Bechthold. Tumor therapy and track structure. *Radiat. Environ. Biophys.*, 38(4):229–237, 1999. doi: 10.1007/s004110050163.

[69] B. Fertil, H. Dertinger, A. Courdi, and E. Malaise. Mean inactivation dose: a useful concept for intercomparison of human cell survival curves. *Radiat. Res.*, 99(1):73–84, 1984. doi: 10.2307/3576448.

[70] S. J. McMahon. The linear quadratic model: usage, interpretation and challenges. *Phys. Med. Biol.*, 64(1):01TR01, 2018. doi: 10.1088/1361-6560/aaf26a.

[71] H. Paganetti, et al. Relative biological effectiveness (RBE) values for proton beam therapy. *Int. J. Radiat. Oncol. Biol. Phys.*, 53(2):407–421, 2002. doi: 10.1016/S0360-3016(02)02754-2.

[72] T. Friedrich, U. Scholz, T. Elsässer, M. Durante, and M. Scholz. Systematic analysis of RBE and related quantities using a database of cell survival experiments with ion beam irradiation. *J. Radiat. Res.*, 54(3):494–514, 12 2012. ISSN 0449-3060. doi: 10.1093/jrr/rrs114.

[73] M. Krämer and M. Scholz. Treatment planning for heavy-ion radiotherapy: calculation and optimization of biologically effective dose. *Phys. Med. Biol.*, 45(11):3319, 2000. doi: 10.1088/0031-9155/45/11/314.

[74] K. Gunzert-Marx, H. Iwase, D. Schardt, and R. Simon. Secondary beam fragments produced by 200 MeV u^{-1} ^{12}C ions in water and their dose contributions in carbon ion radiotherapy. *New J. Phys.*, 10(7):075003, 2008. doi: 10.1088/1367-2630/10/7/075003.

[75] H.-P. Wieser, et al. Development of the open-source dose calculation and optimization toolkit matRad. *Med. Phys.*, 44(6):2556–2568, 2017. doi: 10.1002/mp.12251.

[76] K. Langen and D. Jones. Organ motion and its management. *Int. J. Radiat. Oncol. Biol. Phys.*, 50(1):265–278, 2001. doi: 10.1016/S0360-3016(01)01453-5.

[77] O. Nairz, M. Winter, P. Heeg, and O. Jäkel. Accuracy of robotic patient positioners used in ion beam therapy. *Radiat. Oncol.*, 8(1):124, 2013.

[78] J. M. Balter, et al. Measurement of prostate movement over the course of routine radiotherapy using implanted markers. *Int. J. Radiat. Oncol. Biol. Phys.*, 31(1):113–118, 1995. doi: 10.1016/0360-3016(94)00382-U.

[79] J. Crook, Y. Raymond, D. Salhani, H. Yang, and B. Esche. Prostate motion during standard radiotherapy as assessed by fiducial markers. *Radiother. Oncol.*, 37(1):35–42, 1995. doi: 10.1016/0167-8140(95)01613-L.

[80] R. Ten Haken, et al. Treatment planning issues related to prostate movement in response to differential filling of the rectum and bladder. *Int. J. Radiat. Oncol. Biol. Phys.*, 20(6):1317–1324, 1991. doi: 10.1016/0360-3016(91)90244-X.

[81] P. A. Kupelian, et al. Intraprostatic fiducials for localization of the prostate gland: monitoring intermarker distances during radiation therapy to test for marker stability. *Int. J. Radiat. Oncol. Biol. Phys.*, 62(5):1291–1296, 2005. doi: 10.1016/j.ijrobp.2005.01.005.

[82] L. L. Handsfield, N. J. Yue, J. Zhou, T. Chen, and S. Goyal. Determination of optimal fiducial marker across image-guided radiation therapy (IGRT) modalities: visibility and artifact analysis of gold, carbon, and polymer fiducial markers. *J. Appl. Clin. Med. Phys.*, 13(5):181–189, 2012. doi: 10.1120/jacmp.v13i5.3976.

[83] D. Habermehl, et al. Evaluation of different fiducial markers for image-guided radiotherapy and particle therapy. *J. Radiat. Res.*, 54(suppl_1):i61–i68, 2013. doi: 10.1093/jrr/rrt071.

[84] W. Newhauser, et al. Monte Carlo simulations of the dosimetric impact of radiopaque fiducial markers for proton radiotherapy of the prostate. *Phys. Med. Biol.*, 52(11):2937, 2007. doi: 10.1088/0031-9155/52/11/001.

[85] A. Giebeler, et al. Dose perturbations from implanted helical gold markers in proton therapy of prostate cancer. *J. Appl. Clin. Med. Phys.*, 10(1):63–70, 2009. doi: 10.1120/jacmp.v10i1.2875.

[86] R. Herrmann, J. Carl, O. Jäkel, N. Bassler, and J. B. Petersen. Investigation of the dosimetric impact of a Ni-Ti fiducial marker in carbon ion and proton beams. *Acta Oncol.*, 49(7):1160–1164, 2010. doi: 10.3109/0284186X.2010.505934.

[87] J. Cheung, R. J. Kudchadker, X. R. Zhu, A. K. Lee, and W. D. Newhauser. Dose perturbations and image artifacts caused by carbon-coated ceramic and stainless steel fiducials used in proton therapy for prostate cancer. *Phys. Med. Biol.*, 55(23):7135, 2010. doi: 10.1088/0031-9155/55/23/s13.

[88] J. Y. Huang, W. D. Newhauser, X. R. Zhu, A. K. Lee, and R. J. Kudchadker. Investigation of dose perturbations and the radiographic visibility of potential fiducials for proton radiation therapy of the prostate. *Phys. Med. Biol.*, 56(16):5287, 2011. doi: 10.1088/0031-9155/56/16/014.

[89] T. Matsuura, et al. Biological effect of dose distortion by fiducial markers in spot-scanning proton therapy with a limited number of fields: A simulation study. *Med. Phys.*, 39(9):5584–5591, 2012. doi: 10.1118/1.4745558.

[90] E. H. Heijne, et al. A silicon surface barrier microstrip detector designed for high energy physics. *Nucl. Instrum. Meth.*, 178(2-3):331–343, 1980. doi: 10.1016/0029-554X(80)90812-5.

[91] J. Kemmer. Fabrication of low noise silicon radiation detectors by the planar process. *Nucl. Instrum. Meth.*, 169(3):499 – 502, 1980. ISSN 0029-554X. doi: 10.1016/0029-554X(80)90948-9.

[92] A. J. Theuwissen. CMOS image sensors: State-of-the-art. *Solid State Electron.*, 52(9): 1401 – 1406, 2008. ISSN 0038-1101. doi: 10.1016/j.sse.2008.04.012. Papers Selected from the 37^{th} European Solid-State Device Research Conference - ESSDERC'07.

[93] J. Behr. Test beam measurements with the EUDET pixel telescope. *EUDET-Report-2010-01*, 2, 2010.

[94] R. Turchetta, et al. A monolithic active pixel sensor for charged particle tracking and imaging using standard VLSI CMOS technology. *Nucl. Instrum. Meth. A*, 458 (3):677–689, 2001. doi: 10.1016/S0168-9002(00)00893-7.

[95] G. Deptuch, et al. Simulation and measurements of charge collection in monolithic active pixel sensors. *Nucl. Instrum. Meth. A*, 465(1):92 – 100, 2001. ISSN 0168-9002. doi: 10.1016/S0168-9002(01)00361-8. SPD2000.

[96] G. Claus, et al. Particle tracking using CMOS monolithic active pixel sensor. *Nucl. Instrum. Meth. A*, 465(1):120–124, 2001. doi: 10.1016/S0168-9002(01)00368-0.

[97] G. Deptuch, et al. Development of monolithic active pixel sensors for charged particle tracking. *Nucl. Instrum. Meth. A*, 511(1):240 – 249, 2003. ISSN 0168-9002. doi: 10.1016/S0168-9002(03)01801-1. Proceedings of the 11th International Workshop on Vertex Detectors.

[98] A. Gay, et al. High-resolution CMOS sensors for a vertex detector at the Linear Collider. *Nucl. Instrum. Meth. A*, 549(1):99 – 102, 2005. ISSN 0168-9002. doi: 10.1016/j.nima.2005.04.033. VERTEX 2003.

[99] G. Gaycken, et al. Monolithic active pixel sensors for fast and high resolution vertex detectors. *Nucl. Instrum. Meth. A*, 560(1):44 – 48, 2006. ISSN 0168-9002. doi: 10.1016/j.nima.2005.11.233. Proceedings of the 13^{th} International Workshop on Vertex Detectors.

[100] M. Szelezniak, et al. Application-specific architectures of CMOS monolithic active pixel sensors. *Nucl. Instrum. Meth. A*, 568(1):185 – 190, 2006. ISSN 0168-9002. doi: 10.1016/j.nima.2006.05.226. New Developments in Radiation Detectors.

[101] A. Besson, et al. A vertex detector for the International Linear Collider based on CMOS sensors. *Nucl. Instrum. Meth. A*, 568(1):233 – 239, 2006. ISSN 0168-9002. doi: 10.1016/j.nima.2006.05.279. New Developments in Radiation Detectors.

[102] J. Adams, et al. Experimental and theoretical challenges in the search for the quark–gluon plasma: The STAR Collaboration's critical assessment of the evidence from RHIC collisions. *Nucl. Phys. A*, 757(1-2):102–183, 2005. doi: 10.1016/j.nuclphysa.2005.03.085.

[103] G. Deptuch, et al. Monolithic active pixel sensors with in-pixel double sampling operation and column-level discrimination. *IEEE Trans. Nucl. Sci.*, 51(5):2313–2321, 2004. doi: 10.1109/TNS.2004.835551.

[104] Y. Deerli, N. Fourches, M. Rouger, and P. Lutz. Low-power autozeroed high-speed comparator for the readout chain of a CMOS monolithic active pixel sensor based vertex detector. *IEEE Trans. Nucl. Sci.*, 50(5):1709–1717, 2003. doi: 10.1109/TNS.2003.818266.

[105] Y. Deerli, et al. Performance of a fast binary readout CMOS active pixel sensor chip designed for charged particle detection. *IEEE Trans. Nucl. Sci.*, 53(6):3949–3955, 2006. doi: 10.1109/TNS.2006.886151.

[106] M. Deveaux, et al. Charge collection properties of Monolithic Active Pixel Sensors (MAPS) irradiated with non-ionising radiation. *Nucl. Instrum. Meth. A*, 583(1):134–138, 2007. doi: 10.1016/j.nima.2007.08.189.

[107] T. Haas. A pixel telescope for detector R&D for an international linear collider. *Nucl. Instrum. Meth. A*, 569(1):53 – 56, 2006. ISSN 0168-9002. doi: 10.1016/j.nima.2006.09.011. Proceedings of the 14th International Workshop on Vertex Detectors.

[108] Y. Deerli, et al. Development of binary readout CMOS monolithic sensors for MIP tracking. *IEEE Trans. Nucl. Sci.*, 56(1):354–363, 2009. doi: 10.1109/TNS.2008.2009985.

[109] M. Gélin, et al. Intermediate digital monolithic pixel sensor for the EUDET high resolution beam telescope. *IEEE Trans. Nucl. Sci.*, 56(3):1677–1684, 2009. doi: 10.1109/TNS.2009.2017921.

[110] F. Orsini, et al. A radiation hard digital monolithic pixel sensor for the EUDET-JRA1 project. *IEEE Trans. Nucl. Sci.*, 57(4):2287–2293, 2010. doi: 10.1109/TNS.2010.2050148.

[111] C. Hu-Guo, et al. CMOS pixel sensor development: a fast read-out architecture with integrated zero suppression. *J. Instrum.*, 4(04):P04012, 2009. doi: 10.1088/1748-0221/4/04/P04012.

[112] M. Winter, I.-I. Collaboration, et al. Achievements and perspectives of CMOS pixel sensors for charged particle tracking. *Nucl. Instrum. Meth. A*, 623(1):192–194, 2010. doi: 10.1016/j.nima.2010.02.192.

[113] C. Hu-Guo, et al. First reticule size MAPS with digital output and integrated zero suppression for the EUDET-JRA1 beam telescope. *Nucl. Instrum. Meth. A*, 623(1): 480 – 482, 2010. ISSN 0168-9002. doi: 10.1016/j.nima.2010.03.043. 1^{st} International Conference on Technology and Instrumentation in Particle Physics.

[114] J. Baudot, et al. First test results of MIMOSA-26, a fast CMOS sensor with integrated zero suppression and digitized output. In *2009 IEEE Nuclear Science Symposium Conference Record (NSS/MIC)*, pages 1169–1173. IEEE, 2009. doi: 10.1109/NSSMIC.2009.5402399.

[115] M. Deveaux, et al. Radiation tolerance of a column parallel CMOS sensor with high resistivity epitaxial layer. *J. Instrum.*, 6(02):C02004, 2011. doi: 10.1088/1748-0221/6/02/C02004.

[116] A. Dorokhov, et al. High resistivity CMOS pixel sensors and their application to the STAR PXL detector. *Nucl. Instrum. Meth. A*, 650(1):174–177, 2011. doi: 10.1016/j.nima.2010.12.112.

[117] J. Schambach, et al. A MAPS Based Micro-Vertex Detector for the STAR Experiment. *Phys. Procedia*, 66:514–519, 2015. doi: 10.1016/j.phpro.2015.05.067.

[118] G. Contin, et al. The STAR Heavy Flavor Tracker (HFT): focus on the MAPS based PXL detector. *Nucl. Part. Phys. Proc.*, 273-275:1155 – 1159, 2016. ISSN 2405-6014. doi: 10.1016/j.nuclphysbps.2015.09.181. $37^{[th}$] International Conference on High Energy Physics (ICHEP).

[119] R. Pleskac, et al. The FIRST experiment at GSI. *Nucl. Instrum. Meth. A*, 678: 130–138, 2012. doi: 10.1016/j.nima.2012.02.020.

[120] C. Agodi, et al. FIRST experiment: Fragmentation of Ions Relevant for Space and Therapy. *J. Phys. Conf. Ser.*, 420:012061, mar 2013. doi: 10.1088/1742-6596/420/1/012061.

[121] S. Valle, et al. FOOT: a new experiment to measure nuclear fragmentation at intermediate energies. *Perspectives in Science*, 12:100415, 2019. doi: 10.1016/j.pisc.2019.100415.

[122] W. Snoeys. Development of monolithic sensors for high energy physics in commercial CMOS technologies. *Nucl. Instrum. Meth. A*, 938:41 – 50, 2019. ISSN 0168-9002. doi: 10.1016/j.nima.2019.05.033.

[123] M. Deveaux. Development of CMOS Monolithic Active Pixel Sensors for the ALICE-ITS Outer Barrel and for the CBM-MVD. *24^{th} International Workshop on Vertex Detectors*, page 045, 2015. doi: 10.22323/1.254.0045.

[124] T. A. Collaboration, et al. The ALICE experiment at the CERN LHC. *J. Instrum.*, 3(08):S08002–S08002, aug 2008. doi: 10.1088/1748-0221/3/08/s08002.

[125] A. Besson, et al. From vertex detectors to inner trackers with CMOS pixel sensors. *Nucl. Instrum. Meth. A*, 845:33–37, 2017. doi: 10.1016/j.nima.2016.04.081.

[126] A. D. Mauro. The new inner tracking system for the ALICE upgrade at the LHC. *Nucl. Instrum. Meth. A*, 936:625 – 629, 2019. ISSN 0168-9002. doi: 10.1016/j.nima.2018.10.047. Frontier Detectors for Frontier Physics: 14th Pisa Meeting on Advanced Detectors.

[127] T. Ablyazimov, et al. Challenges in QCD matter physics–The scientific programme of the Compressed Baryonic Matter experiment at FAIR. *Eur. Phys. J. A*, 53(3):60, 2017. doi: 10.1140/epja/i2017-12248-y.

[128] A. Dorokhov. Optimization of amplifiers for monolithic active pixel sensors. *Topical Workshop on Electronics for Particle Physics*, 2007. doi: 10.5170/CERN-2007-007.423.

[129] W. Dulinski, et al. Beam telescope for medium energy particles based on thin, submicron precision MAPS. In *2007 IEEE Nuclear Science Symposium Conference Record*, volume 2, pages 995–1002. IEEE, 2007. doi: 10.1109/NSSMIC.2007.4437182.

[130] C. J. Kalkman. LabVIEW: a software system for data acquisition, data analysis, and instrument control. *J. Clin. Monit. Comput.*, 11(1):51–58, 1995. doi: 10.1007/BF01627421.

[131] J. Koh. *Catia V5 design fundamentals*. Onsia, 2012.

[132] C. A. Schneider, W. S. Rasband, and K. W. Eliceiri. NIH Image to ImageJ: 25 years of image analysis. *Nat. Methods*, 9(7):671, 2012. doi: 10.1038/nmeth.2089.

[133] R. Brun and F. Rademakers. ROOT – an object oriented data analysis framework. *Nucl. Instrum. Meth. A*, 389(1-2):81–86, 1997. doi: 10.1016/S0168-9002(97)00048-X.

[134] S. Agostinelli, et al. Geant4—a simulation toolkit. *Nucl. Instrum. Meth. A*, 506 (3):250 – 303, 2003. ISSN 0168-9002. doi: https://doi.org/10.1016/S0168-9002(03)01368-8.

[135] R. Rescigno, et al. Performance of the reconstruction algorithms of the FIRST experiment pixel sensors vertex detector. *Nucl. Instrum. Meth. A*, 767:34–40, 2014. doi: 10.1016/j.nima.2014.08.024.

[136] Folger, G., Ivanchenko, V. N., and Wellisch, J. P. The Binary Cascade - Nucleon nuclear reactions. *Eur. Phys. J. A*, 21(3):407–417, 2004. doi: 10.1140/epja/i2003-10219-7.

[137] V. N. Ivanchenko, O. Kadri, M. Maire, and L. Urban. Geant4 models for simulation of multiple scattering. *J. Phys. Conf. Ser.*, 219(3):032045, apr 2010. doi: 10.1088/1742-6596/219/3/032045.

[138] V. Blobel. Software alignment for tracking detectors. *Nucl. Instrum. Meth. A*, 566 (1):5–13, 2006. doi: 10.1016/j.nima.2006.05.157.

[139] V. Karimaki, A. Heikkinen, T. Lampen, and T. Linden. Sensor Alignment by Tracks, 2003.

[140] V. Blobel and C. Kleinwort. A New Method for the High-Precision Alignment of Track Detectors, 2002.

[141] C.-A. Reidel, C. Finck, C. Schuy, M. Rovituso, and U. Weber. Alignment procedure of silicon pixel detectors for ion-beam therapy applications. *Nucl. Instrum. Meth. A*, 931:142–150, 2019. doi: 10.1016/j.nima.2019.03.042.

[142] B. Gottschalk, A. Koehler, R. Schneider, J. Sisterson, and M. Wagner. Multiple Coulomb scattering of 160 MeV protons. *Nucl. Instrum. Meth. B*, 74(4):467–490, 1993. doi: 10.1016/0168-583X(93)95944-Z.

[143] D. C. Montgomery, E. A. Peck, and G. G. Vining. *Introduction to Linear Regression Analysis*, volume 821, chapter 2, pages 12–14. John Wiley & Sons, 5 edition, 2012.

[144] F. Tommasino, et al. Proton beam characterization in the experimental room of the Trento Proton Therapy facility. *Nucl. Instrum. Meth. A*, 869:15–20, 2017. doi: 10.1016/j.nima.2017.06.017.

[145] T. Haberer, et al. The heidelberg ion therapy center. *Radiother. Oncol.*, 73:S186–S190, 2004. doi: 10.1016/S0167-8140(04)80046-X.

[146] L. Eyges. Multiple scattering with energy loss. *Phys. Rev.*, 74(10):1534, 1948. doi: 10.1103/PhysRev.74.1534.

[147] M. Hollmark, J. Uhrdin, D. Belkić, I. Gudowska, and A. Brahme. Influence of multiple scattering and energy loss straggling on the absorbed dose distributions of therapeutic light ion beams: I. Analytical pencil beam model. *Phys. Med. Biol.*, 49 (14):3247, 2004. doi: 10.1088/0031-9155/49/14/016.

[148] T. P. Ringbæk, et al. Fluence inhomogeneities due to a ripple filter induced Moiré effect. *Phys. Med. Biol.*, 60(3):N59, 2015. doi: 10.1088/0031-9155/60/3/N59.

[149] U. Scheeler et al. Recommissioning of the Marburg Ion-beam Therapy Centre (MIT) Accelerator Facility. In *Proceedings, 7th International Particle Accelerator Conference (IPAC 2016): Busan, Korea, May 8-13, 2016*, page TUPOY004, 2016. doi: 10.18429/JACoW-IPAC2016-TUPOY004.

[150] C.-A. Reidel, et al. Fluence perturbation from fiducial markers due to edge-scattering measured with pixel sensors for ^{12}C ion beams. *Phys. Med. Biol.*, 2020. doi: 10.1088/1361-6560/ab762f.

[151] E. Y. León-Marroquín, et al. Investigation of EBT3 radiochromic film's response to humidity. *J. Appl. Clin. Med. Phys.*, 19(3):283–290, 2018. doi: 10.1002/acm2.12337.

[152] A. A. Schoenfeld, S. Wieker, D. Harder, and B. Poppe. The origin of the flatbed scanner artifacts in radiochromic film dosimetry–key experiments and theoretical descriptions. *Phys. Med. Biol.*, 61(21):7704, 2016. doi: 10.1088/0031-9155/61/21/7704.

[153] V. C. Borca, et al. Dosimetric characterization and use of GAFCHROMIC EBT3 film for IMRT dose verification. *J. Appl. Clin. Med. Phys.*, 14(2):158–171, 2013. doi: 10.1120/jacmp.v14i2.4111.

[154] Physics at the Terascale, Millepede II. http://www.terascale.de/wiki/millepede_ii.

[155] K. Parodi, et al. The influence of lateral beam profile modifications in scanned proton and carbon ion therapy: a Monte Carlo study. *Phys. Med. Biol.*, 55(17):5169, 2010. doi: 10.1088/0031-9155/55/17/018.

[156] V. Bellinzona, et al. On the parametrization of lateral dose profiles in proton radiation therapy. *Phys. Medica*, 31(5):484–492, 2015. doi: 10.1016/j.ejmp.2015.05.004.

[157] S. Russo, et al. Dosimetric characterization of a commercial 2-D scintillation detector for quality assurance tests in scanned proton and carbon ion beams. *Phys. Medica*, 32:199, 2016. ISSN 1120-1797. doi: 10.1016/j.ejmp.2016.07.675. Abstracts from the 1^{st} European Congress of Medical Physics.

List of publications

Parts of the research in this thesis have been published in the following peer-reviewed publications:

- C.-A. Reidel, C. Finck, C. Schuy, M. Rovituso, and U. Weber. Alignment procedure of silicon pixel detectors for ion-beam therapy applications. *Nucl. Instrum. Meth. A*, 931:142–150, 2019. doi: 10.1016/j.nima.2019.03.042
- C.-A. Reidel, C. Schuy, F. Horst, S. Ecker, C. Finck, M. Durante and U. Weber. Fluence perturbation from fiducial markers due to edge-scattering measured with pixel sensors for ^{12}C ion beams. *Phys. Med. Biol.*, 2020. doi: 10.1088/1361-6560/ab762f

Other peer-reviewed publications:

- F. Horst, W. Adi, G. Aricò, K.-T. Brinckmann, M. Durante, C.-A. Reidel, M. Rovituso, U. Weber, H.-G. Zaunick, K. Zink and C. Schuy. Measurement of PET isotope production cross sections for protons and carbon ions on carbon and oxygen targets for applications in particle therapy range verification. *Phys. Med. Biol.*, 64(20):205012, 2019. doi: 10.1088/1361-6560/ab4511
- F. Horst, G. Aricò, K.-T. Brinckmann, S. Brons, A. Ferrari, T. Haberer, A. Mairani, K. Parodi, C.-A. Reidel, U. Weber, K. Zink and C. Schuy. Measurement of ^{4}He charge-and mass-changing cross sections on H, C, O, and Si targets in the energy range 70–220 MeV/u for radiation transport calculations in ion-beam therapy. *Phys. Rev. C*, 99(1):014603, 2019. doi: 10.1103/PhysRevC.99.014603

Press publications related to this work:

- How do fiducial markers affect particle therapy dose distributions? *Phys. World*, March 2020, https://physicsworld.com/a/how-do-fiducial-markers-affect--particle-therapy-dose-distributions/

Claire-Anne REIDEL

Applications for CMOS pixel sensors in ion-beam therapy

Résumé : En hadronthérapie, des mesures de haute précision sont essentielles pour avoir une base de données robuste et délivrer le traitement prescrit au patient. Dans ce travail, un système de trajectométrie, composé de capteurs à pixels MIMOSA-28, a été utilisé pour différentes applications cliniques. Plusieurs améliorations ont été implémentées au niveau matériel et logiciel résultant à une résolution spatiale de trace $\leqslant 10$ μm. Les expériences ont été menées avec succès dans différents centres médicaux et de recherche. Les profils de faisceaux ont été mesurés et la largeur du faisceau le long de l'axe a pu être calculée grâce à un code de transport basé sur la diffusion. Un outil en ligne de suivi de faisceau a été développé pour avoir une information rapide de son profil. D'autre part, les perturbations de la fluence dues à des marqueurs de repères pour un faisceau ^{12}C ont été évaluées. Après reconstruction et extrapolation de chaque trace, une distribution 3D de la fluence a pu être établie et la perturbation maximale de la fluence et sa position ont pu être quantifiées. Les points froids mesurés varient entre moins de 3% à 9.2% pour un marqueur et une énergie de faisceau définis.

Mots clés : Hadronthérapie, MIMOSA-28, Capteur à pixels CMOS, Profil de faisceau, Marqueurs de repère

Abstract: In ion-beam therapy, high precision measurements are essential for having robust basic data to deliver the prescribed treatment to the patient. In this study, MIMOSA-28 pixel sensors were used as a tracker system for different medical applications. Several hardware and software improvements were implemented leading to a spatial track resolution $\leqslant 10$ μm. The experiments were conducted with success in different medical and research facilities. In this work, beam profiles were measured along the beam axis and the width of the beam along the axis could be calculated with a transportation code based on multiple Coulomb scattering. Moreover, an online beam monitoring was developed in order to have fast information about the beam profile. In another study, the fluence perturbation of ^{12}C ion beams due to small fiducial markers was investigated. After reconstruction and extrapolation of single track, a 3D fluence distribution could be performed and the maximum perturbation and its position along the beam axis could be quantified. In this work, the measured cold spot varied between less than 3% up to 9.2% for a defined marker and a defined primary energy beam.

Keywords: Ion-beam therapy, MIMOSA-28, CMOS pixel sensor, Beam profile, Fiducial marker